

SYNTHETIC ANTIOXIDANT POLYMERS: SYNTHESIS, ADSORPTION,
AND LAYER-BY-LAYER ASSEMBLY

A Dissertation

by

RAMAN HLUSHKO

Submitted to the Graduate and Professional School of
Texas A&M University
in partial fulfillment of the requirements for the degree of

DOCTOR OF PHILOSOPHY

Chair of Committee,	Svetlana A. Sukhishvili
Committee Members,	Jodie L. Lutkenhaus
	Melissa A. Grunlan
	Yossef A. Elabd
Head of Department,	Ibrahim Karaman

August 2021

Major Subject: Materials Science and Engineering

Copyright 2021 Raman Hlushko

ABSTRACT

This dissertation is focused on synthesis of a new class of polyphenol polymers with antioxidant properties which are potentially useful in adhesives, anticorrosion coatings, food packaging, and biomedical applications. It also explores the effect of chemical structure of the polyphenol pendant groups and polymer backbone on the layer-by-layer (LbL) assembly of these polymers, and the performance of the resultant films in radical scavenging and self-healing applications.

Linear polymeric polyphenol antioxidants with designed molecular weights and narrow molecular weight distributions were synthesized using reversible addition-fragmentation chain transfer (RAFT) polymerization. The polymers were based on the polymethacrylamide or the polyacrylamide backbone and contained functional catechol-, gallol-, or bromocatechol-polyphenol moieties. The developed synthetic routes enabled controlling antioxidant activity and hydrophobicity of these polymers simultaneously. That was achieved *via* variation of the chemical structure of the polyphenol groups and the introduction of non-oxidant hydrophobic units *via* copolymerization.

Linear homopolymers of gallol-based and catechol-based polyphenols were assembled with a neutral polymer within hydrogen-bonded LbL films, revealing drastic differences in film growth modes and the internal film structure for the films built with different polyphenols. Spectroscopic ellipsometry was used to determine growth regimes and swelling characteristics of these films, while neutron reflectometry involving deuterated marker layers enabled studies of internal film structure. Differences in the film structure strongly affected antioxidant performance and dynamics of hydrogen-bonded films in aqueous environment. In particular, gallol-based polymethacrylamide demonstrated the highest antioxidant activity because of self-association of

gallol units and weaker intermolecular binding within LbL films, which allowed deeper penetration of radicals and their more efficient interactions with polyphenol moieties. In contrast, catechol-containing LbL films demonstrated lowest activity due to densely assembled layered structure, which limit interactions between assembled polyphenols and free radicals in solution. Additionally, differences in strength of intermolecular binding resulted in diverse self-healing behavior. As demonstrated by *in situ* atomic force microscopy (AFM), while robust self-healing of gallol-containing films occurred at the time scale of minutes, no healing was observed in the case of catechol-containing films. These results are rationalized through differences in the polymer chain mobility in these two cases, which are further quantified by *in situ* ellipsometry and neutron reflectometry studies.

ACKNOWLEDGEMENTS

I would like to express the deepest gratitude and great appreciation to my research advisor and committee chair, Professor Svetlana A. Sukhishvili for her guidance, support and patience.

I would like to thank my committee members, Dr. Lutkenhaus, Dr. Grunlan, and Dr. Elabd for their advising and support throughout the course of this research. I would like to thank Dr. John F. Ankner for his contribution to this work.

I thank my group members Aliaksei Aliakseyeu, Jordan Brito, Diana Al Hussein, Al-Farabi Kopzhassar, Kartik Kumar Rajagopalan, Zhen Sang, Qing Zhou, and Xiuzhu Zhu. I also would like to thank staff members, Murat Kaynak, Amy Caldwell, Sheri Stebenne, Hanna Prichard, Amanda Sanders, Andrea Raines, Isabel Cantu, and Holley Toschlog, as well as my academic advisors Jules Henry and Erin Bandza.

I also would like to thank my former colleagues Dr. Hanna Hlushko, Dr. Viktor Selin, Dr. Victoria Albright, Dr. Parvin Karimi, Anja Krieger, Yashaswini Karath, and Adwait Gaikwad.

I would like to thank the staff of Materials Characterization facility for help with instruments and my analysis, including Dr. Wilson Serem, Dr. Yordanos Bisrat, and Dr. Jing Wu.

Thanks also to my friends and colleagues and the department faculty and staff for making my time at Texas A&M University a great experience.

I would like to thank my family for their encouragement and to my wife for her patience and endless support.

CONTRIBUTORS AND FUNDING SOURCES

Contributions

This work was supported by dissertation committee consisting of Professor Svetlana A. Sukhishvili of the Department of Materials Science and Engineering, Prof. Jodie L. Lutkenhaus of the Department of Chemical Engineering. Prof. Melissa A. Grunlan of the Department of Biomedical Engineering, and Prof. Yossef A. Elabd of the Department of Chemical Engineering.

The antioxidant properties of *PPH* polymers in solution were completed by Hanna Hlushko, a graduate student of Materials Science and Engineering department and were published in 2018 an article listed in the Biographical Sketch. The neutron reflectivity data analysis for Chapters 3 and 4 was provided by Dr. John F. Ankner from Oak Ridge National Laboratory and were published in 2020 in an article listed in the Biographical Sketch.

All other work conducted for the dissertation was completed by the student independently.

Funding Sources

This graduate study was partially supported by a research assistantship from Texas A&M Engineering Experiment Station and the graduate teaching assistantship from Texas A&M University.

This work was funded in part by National Science Foundation under Grant Numbers DMR-1610725 and DMR-1905535.

NOMENCLATURE

ABTS	2,2'-Azino-bis(3-Ethylbenzothiazoline-6-Sulfonic Acid)
AFM	Atomic Force Microscopy
AIBN	Azobisisobutyronitrile
ATR	Attenuated Total Reflection
BPEI	Branched Poly(Ethylene Imine)
CA	Contact Angle
CPD-TTC	2-Cyano-2-Propyl Dodecyl Trithiocarbonate
CTA	Chain Transferring Agent
DDMAT	2-(Dodecylthiocarbonothioylthio)-2-Methylpropionic Acid
DI	Deionized
DMF	Dimethylformamide
DMSO	Dimethylsulfoxide
DOPA	3,4-Dihydroxy-L-phenylalanine
DPPH	2,2-Diphenyl-1-Picrylhydrazyl
DSC	Differential Scanning Calorimetry
FTIR	Fourier Transform Infrared Spectroscopy
FRAP	Fluorescence Recovery After Photobleaching
GPC	Gel Permeation Chromatography
HB	Hydrogen Bond
IR	Infrared
LbL	Layer-by-layer
/PPh	Linear Synthetic Polyphenol Polymer
NMR	Nuclear Magnetic Resonance

NR Neutron Reflectometry

MCT Mercury Cadmium Telluride Detector

ORNL Oak Ridge National Laboratory

P2MAA Poly (N-(3,4-Dimethoxybenzyl) Acrylamide)

P2MMA Poly (N-(3,4-Dimethoxybenzyl) Methacrylamide)

P3MAA Poly (N-(3,4,5-Trimethoxybenzyl) Acrylamide)

P3MMA Poly (N-(3,4,5-Trimethoxybenzyl) Methacrylamide)

PBrMMA Poly (N-(3,4-Dimethoxy-5-Bromobenzyl) Methacrylamide)

P2HAA Poly (N-(3,4-Dihydroxybenzyl) Acrylamide)

P2HMA Poly (N-(3,4-Dihydroxybenzyl) Methacrylamide)

P3HAA Poly (N-(3,4,5-Trihydroxybenzyl) Acrylamide)

P3HMA Poly (N-(3,4,5-Trihydroxybenzyl) Methacrylamide)

PBrHMA Poly (N-(3,4-Dihydroxy-5-Bromobenzyl) Methacrylamide)

PVP Poly (Vinyl Pyrrolidone)

PDI Polydispersity Index

PEO Polyethylene Oxide

dPEO Deuterated Polyethylene Oxide

PHex Poly (N-Hexyl Methacrylamide)

PVP Poly (N-Vinyl Pyrrolidone)

RAFT Reversible Addition Fragmentation Chain Transfer

RI Refractive Index

ROS Reactive Oxygen Species

RT Room Temperature

SLD Scattering Length Density

SNS-LR Spallation Neutron Source Liquids Reflectometer

TA Tannic Acid

TEA Triethylamine

TGA Thermal Gravimetric Analysis

THF Tetrahydrofuran

UV Ultraviolet

VASE Variable Angle Spectroscopic Ellipsometer

QCM Quartz Crystal Microbalance

TABLE OF CONTENTS

	Page
ABSTRACT.....	ii
ACKNOWLEDGEMENTS.....	iv
CONTRIBUTORS AND FUNDING SOURCES	v
NOMENCLATURE	vi
TABLE OF CONTENTS.....	ix
LIST OF FIGURES	xi
LIST OF TABLES.....	xv
1. INTRODUCTION	1
1.1. Polyphenols.....	1
1.2. Layer-by-layer assembly.....	2
1.3. Goal and Objectives.....	3
2. SYNTHESIS OF LINEAR POLYPHENOL POLYMERS.....	4
2.1. Abstract.....	4
2.2. Introduction.....	4
2.3. Experimental Section.....	6
2.3.1. Materials	6
2.3.2. Characterization Methods	7
2.4. Synthetic Protocols	9
2.4.1. Synthesis of Monomers.....	9
2.4.2. RAFT Polymerization of Monomers	11
2.4.3. Demethylation.....	12
2.4.4. Studies of polymerization kinetics.....	13
2.5. Results and Discussion	13
2.5.1. Synthesis and characterization of phenolic polymers.....	13
2.6. Surface Adsorption of Polyphenolic Polymers.....	20
2.7. Conclusions.....	23
2.8. Acknowledgements.....	23
3. LAYER-BY-LAYER HYDROGEN-BONDED ANTIOXIDANT FILMS OF LINEAR SYNTHETIC POLYPHENOLS.....	24
3.1. Abstract.....	24

3.2. Introduction.....	25
3.3. Experimental section.....	27
3.3.1. Materials	27
3.3.2. Film Deposition	27
3.3.3. Methods.....	28
3.4. Results and discussion	31
4. DYNAMICS AND SELF-HEALING OF LAYER-BY-LAYER HYDROGEN-BONDED FILMS OF LINEAR SYNTHETIC POLYPHENOLS	45
4.1. Abstract.....	45
4.2. Introduction.....	46
4.3. Experimental section.....	49
4.3.1. Materials	49
4.3.2. Film Deposition	49
4.3.3. Methods.....	50
4.4. Results and discussion	52
4.5. Acknowledgments	69
5. CONCLUSIONS.....	70
REFERENCES	73
APPENDIX A SUPPORTING INFORMATION FOR THE CHAPTER 2	85
APPENDIX B SUPORTING INFORMATION FOR THE CHAPTER 3.....	91
APPENDIX C SUPORTING INFORMATION FOR THE CHAPTER 4.....	98

LIST OF FIGURES

	Page
Figure 2-1 Generalized representation of synthesis of precursors of phenolic monomers.....	10
Figure 2-3 Time evolution of $\ln([M]_0/[M]_t)$ during synthesis of PHex homopolymer and copolymers containing 10% of phenolic precursor groups (A), as well as representative GPC traces shown for synthesis of P3M ₁₀ Hex interrupted at various polymerization times (B) when polymerization was carried out at 70°C.	15
Figure 2-4 ¹ H NMR spectra of P3MMA in CDCl ₃ (purple) and P3HMA in CD ₃ OD (blue) (A); FTIR spectra of P3MMA (purple) and P3HMA (blue) (B). The 3500-1800 cm ⁻¹ region is shown in the Appendix A, Fig. A-3.	16
Figure 2-5 ¹ H NMR spectra of P3M ₁₅ Hex (maroon) and P3H ₁₅ Hex (blue) in CD ₃ OD, as well as PHex (green) in CDCl ₃ (A); FTIR spectra of P3M ₁₅ Hex (maroon), P3H ₁₅ Hex (blue), and PHex (green) (B).	17
Figure 2-6 Adsorption of polymers at the surface of gold substrates: dry thicknesses of monolayers of homopolymers (A) and copolymers (B) adsorbed from 1.0 mg mL ⁻¹ methanol solutions.....	21
Figure 2-7 The effect of adsorbed polymer monolayers on water contact angles measured on gold surfaces coated with adsorbed monolayers of the antioxidant homopolymers and copolymers.	22
Figure 3-1 Chemical structures and molecular characteristics of <i>l</i> PPhs (A); the dry thickness of <i>l</i> PPh/PEO films monitored by ellipsometry during film deposition (B); and changes in FTIR spectra of 6.5-bilayer P3HMA/PEO (C) or 50.5-bilayer P2HMA/PEO (D) films (with <i>l</i> PPh as a top layer in both cases) of matched thickness of ~200 nm in the 1250-950 cm ⁻¹ region upon addition of consecutive layers (E). See Figures B-1, B-2 for the entire FTIR spectra.....	33
Figure 3-2 Schematic of the film design, where H-stacks are built of hydrogenated PEO and <i>l</i> PPh, and D-stacks are built of deuterated PEO and <i>l</i> PPh (A); neutron reflectivity plotted as RQ^4 to highlight structural details for (P3HMA/PEO) ₂ /P3HMA/ <i>d</i> PEO/P3HMA/PEO/P3HMA/ <i>d</i> PEO and (P2HMA/PEO) ₂ /(P2HMA/ <i>d</i> PEO) ₂ /(P2HMA/PEO) ₇ /(P2HMA/ <i>d</i> PEO) ₂ films (B), and the fitted neutron scattering density profiles of those films (C).	35
Figure 3-3 AFM topography image of a 6.5-bilayer P3HMA/PEO film (A) and a 50.5-bilayer P2HMA/PEO film (B) of a matched thickness of ~200 nm. The scan area size is 600 × 600 nm ² and the <i>z</i> -scale shown on the right applies to both images.	37

Figure 3-4 Comparison of kinetics of ABTS ^{•+} scavenging by matched quantities of <i>I</i> PPh antioxidant polymer dissolved in solution or assembled within a 98-nm (4.5-bilayer) P3HMA/PEO film (A) or a 92.2-nm (25.5-bilayer) P2HMA/PEO film (B). Both films had <i>I</i> PPh as a top layer.	38
Figure 3-5 Time evolution of ABTS ^{•+} quantity reacted with P3HMA/PEO (A) and P2HMA/PEO (B) films of different thicknesses, as well as antioxidant activity of <i>I</i> PPH/PEO films assessed from the limiting values of ABTS ^{•+} reduced after 15 days (C).....	39
Figure 3-6 Schematic representation of ABTS ^{•+} radical penetration into the bulk of the exponential P3HMA/PEO film (A), and the linear P2HMA/PEO film (B). The green area depicts the antioxidant active region.	40
Figure 3-7 The swelling ratios of a 4.5-bilayer, 98-nm P3HMA/PEO film and a 25.5-bilayer, 92.2-nm P2HMA/PEO film as measured <i>by in situ</i> ellipsometry (A) and Young's moduli of 0.6- μ m-thick <i>I</i> PPH/PEO films dry and wet state (B).	41
Figure 3-8 Stability of 6.5-bilayer P3HMA/PEO and 50.5-bilayer P2HMA/PEO films with a matched thickness of \sim 200 nm in the DMF/water mixed solution before (dotted line) and after (solid line) exposure to 0.075 mM solutions of ABTS ^{•+} for 15 days (A), as well ATR-FTIR spectra of the films before and after a 5-day assay (B).	43
Figure 4-1 Dry thickness measured by spectroscopic ellipsometry during sequential deposition of <i>I</i> PPH/PEO films from 0.2 mg/ml polymer solutions using a 5 min per layer deposition time (A), and a comparison of dry film thicknesses measured using deposition time of 5 min (solid symbols) and 300 min per layer (open symbols) for P3/PEO systems (B) and P2/PEO systems (C).	53
Figure 4-2 <i>In situ</i> spectroscopic ellipsometry measurements of the uptake of PEO or <i>I</i> PPHs from 0.2 mg/ml aqueous or ethanol solutions (A and B, respectively) by \sim 100-nm <i>I</i> PPH/PEO films constructed using 5-min per layer deposition time. Swelling ratios of <i>I</i> PPH/PEO films in water (C) and ethanol (D) during the polymer uptake.	56
Figure 4-3 Scattering length density profiles (A-D) of hydrogenated <i>I</i> PPH/PEO films before (dashed lines) and after (solid lines) a 2-min exposure to a 0.2 mg/mL <i>d</i> PEO aqueous solution for 22.5-bilayer P2HMA/PEO (A), 15.5-bilayer P2HAA/PEO (B), 10.5-bilayer P3HAA/PEO (C), and 6.5-bilayer P3HMA/PEO (D) films, as well as changes in the total film thickness (symbols) and thickness of the <i>d</i> PEO-rich surface layer (bars) upon exposure of <i>I</i> PPH/PEO films to 0.2 mg/mL <i>d</i> PEO aqueous solutions for different times (E).	60
Figure 4-4 Self-healing of \sim 400-nm-thick <i>I</i> PPH/PEO films measured by <i>in situ</i> AFM during immersion in water. AFM images and depth profiles of the indented areas as a function of time for P2HMA/PEO (A, B), P2HAA/PEO (C, D), P3HAA/PEO (E, F), and P3HMA/PEO (G, H) films, respectively.	63

Figure 4-5 Time evolution of the lateral dimensions of the indented areas measured at the depth of 40 nm within the films using <i>in situ</i> AFM for P2HMA/PEO (A), P2HAA/PEO (B), P3HAA/PEO (C), and P3HMA/PEO (D) films during their continuous immersion in water.	65
Figure 4-6 Time evolution of the deepest point of the indented areas measured using <i>in situ</i> AFM for P2HMA/PEO (A), P2HAA/PEO (B), P3HAA/PEO (C), and P3HMA/PEO (D) films during their continuous immersion in water.....	67
Figure A-1 The number-average molecular weight M_n (A) and molar mass dispersities (B) as a function of polymerization time during synthesis of P2M ₁₀ Hex, PBrM ₁₀ Hex, or P3M ₁₀ Hex at 80°C.....	86
Figure A-2 GPC traces of PHex (A), P2M ₁₀ Hex (B), PBrM ₁₀ Hex (C) for different polymerization times, as well as M_n (D) and molar mass dispersities (E) as a function of monomer conversion during polymerization of PHex homopolymer and copolymers containing 10% of phenolic precursor groups at 70°C.....	87
Figure A-3 FTIR spectra of protected and deprotected P3MMA and P3HMA homopolymers (A), P3M ₁₅ Hex and P3H ₁₅ Hex copolymers (B, top) and PHex control polymer (B, bottom).	88
Figure A-4 FTIR spectra of protected and deprotected homopolymers: P2MMA and P2HMA (A), and PBrMMA and PBrHMA (B).....	89
Figure A-5 FTIR spectra of the copolymers of P3M _Z Hex and P3H _Z Hex series (A), P2M _Z Hex and P2H _Z Hex series (B), as well as PBrM _Z Hex and PBrH _Z Hex series (C).	90
Figure B-1 ATR-FTIR spectra of P3HMA, 6.5-bilayer P3HMA/PEO film, P2HMA, 50.5-bilayer P2HMA/PEO film and PEO.....	94
Figure B-2 ATR-FTIR spectra of P3HMA, 6.5-bilayer P3HMA/PEO film, P2HMA and 50.5-bilayer P2HMA/PEO film, and PEO between 3800 and 2700 cm ⁻¹	95
Figure B-3 pH stability of four-bilayer /PPh/PEO films assessed as dry film thickness retained after 60 min of sequential exposure to phosphate buffer solutions at increasing pH....	95
Figure B-4 Self-degradation of ABTS ^{•+} radical cation solutions with time as the percentage of initial absorbance value at 732 nm for 0.075 mM ABTS ^{•+} solution (A), and 0.075 mM ABTS ^{•+} in the presence of 0.5 mg/mL PEO (B).....	96
Figure B-5 Proposed resonance structures of semi-quinone radical of P2HMA and a radical coupling crosslinking structure.	96
Figure B-6 Proposed resonance structures of semi-quinone radical of P3HMA and a radical coupling crosslinking structure.	97

Figure C-1 A stepwise procedure used for P2HAA and P3HAA synthesis. Step i: acryloyl chloride, TEA, CH ₂ Cl ₂ , 30 min; step ii: AIBN as initiator, CPDTTC as CTA, dioxane, 70°C, 12-24 h; step iii: 1) BBr ₃ , CH ₂ Cl ₂ , -45°C to RT, 12 h; 2) water, overnight.....	98
Figure C-2 Time evolution of the lateral dimensions of the indented areas measured at the depth of 25 nm within the films using <i>in situ</i> AFM for P2HMA/PEO (A), P2HAA/PEO (B), P3HAA/PEO (C), and P3HMA/PEO (D) films during their continuous immersion in water.	115
Figure C-3 Time evolution of the lateral dimensions of the indented areas measured at the depth of 60 nm within the films using <i>in situ</i> AFM for P2HMA/PEO (A), P2HAA/PEO (B), P3HAA/PEO (C), and P3HMA/PEO (D) films during their continuous immersion in water.	116

LIST OF TABLES

	Page
Table 2-1 Compositions, Molecular Weight and Polydispersity of Antioxidant Polymers.	19
Table A-1 P2HzHex series and PHex.	85
Table A-2 PBrHzHex series.	85
Table A-3 P3HzHex series.	86
Table B-1 Dry thicknesses measured by ellipsometry during deposition of a (P3HMA/PEO) ₂ /P3HMA/ <i>d</i> PEO/P3HMA/PEO/P3HMA/ <i>d</i> PEO film.	91
Table B-2 Dry thicknesses measured by ellipsometry during deposition of a (P2HMA/PEO) ₂ /(P2HMA/ <i>d</i> PEO) ₂ /(P2HMA/PEO) ₇ /(P2HMA/ <i>d</i> PEO) ₂ film.	91
Table B-3 Model parameters for a (P3HMA/PEO) ₂ /P3HMA/ <i>d</i> PEO/P3HMA/PEO/P3HMA/ <i>d</i> PEO film. The interfacial widths, σ_{int} , are given as full-width-at-half-maximum (FWHM), which is 2.35 times larger than the more commonly used root-mean-squared (RMS) width.	92
Table B-4 Model parameters for a (P2HMA/PEO) ₂ /(P2HMA/ <i>d</i> PEO) ₂ /(P2HMA/PEO) ₇ / (P2HMA/ <i>d</i> PEO) ₂ film.	93
Table B-5 Assignment of FTIR bands of linear polyphenols.	93
Table C-1 Scattering lengths and stoichiometries for the components of the polyphenols and PEO: Compound, Formula Unit, the sum of the scattering lengths $\sum_j b_j$ of the nuclei in the Formula Unit, its molecular mass M , and its stoichiometry S	102
Table C-2 Model parameters for the (P2HMA/PEO) ₁₅ /P2HAA film. The interfacial widths, σ , are given as full-width-at-half-maximum (FWHM), which is 2.35 times larger than the more commonly used root-mean-squared (RMS).	105
Table C-3 Model parameters for the (P2HAA/PEO) ₁₅ /P2HAA film exposed to 0.2 mg/mL aqueous solution of <i>d</i> PEO for 1 min. The interfacial widths, σ , are given as full- width-at-half-maximum (FWHM), which is 2.35 times larger than the more commonly used root-mean-squared (RMS).	105
Table C-4 Model parameters for the (P2HAA/PEO) ₁₅ /P2HAA film exposed to 0.2 mg/mL aqueous solution of <i>d</i> PEO for 2 min. The interfacial widths, σ , are given as full- width-at-half-maximum (FWHM), which is 2.35 times larger than the more commonly used root-mean-squared (RMS).	106

Table C-5 Model parameters for the (P2HAA/PEO) ₁₅ /P2HAA film exposed to 0.2 mg/mL aqueous solution of <i>d</i> PEO for 5 min. The interfacial widths, σ , are given as full-width-at-half-maximum (FWHM), which is 2.35 times larger than the more commonly used root-mean-squared (RMS).	106
Table C-6 Model parameters for the (P2HAA/PEO) ₁₅ /P2HAA film exposed to 0.2 mg/mL aqueous solution of <i>d</i> PEO for 10 min. The interfacial widths, σ , are given as full-width-at-half-maximum (FWHM), which is 2.35 times larger than the more commonly used root-mean-squared (RMS).	107
Table C-7 Model parameters for the (P2HMA/PEO) ₂₂ /P2HMA film. The interfacial widths, σ , are given as full-width-at-half-maximum (FWHM), which is 2.35 times larger than the more commonly used root-mean-squared (RMS).	107
Table C-8 Model parameters for the (P2HMA/PEO) ₂₂ /P2HMA film exposed to 0.2 mg/mL aqueous solution of <i>d</i> PEO for 1 min. The interfacial widths, σ , are given as full-width-at-half-maximum (FWHM), which is 2.35 times larger than the more commonly used root-mean-squared (RMS).	108
Table C-9 Model parameters for the (P2HMA/PEO) ₂₂ /P2HMA film exposed to 0.2 mg/mL aqueous solution of <i>d</i> PEO for 2 min. The interfacial widths, σ , are given as full-width-at-half-maximum (FWHM), which is 2.35 times larger than the more commonly used root-mean-squared (RMS).	108
Table C-10 Model parameters for the (P2HMA/PEO) ₂₂ /P2HMA film exposed to 0.2 mg/mL aqueous solution of <i>d</i> PEO for 5 min. The interfacial widths, σ , are given as full-width-at-half-maximum (FWHM), which is 2.35 times larger than the more commonly used root-mean-squared (RMS).	109
Table C-11 Model parameters for the (P2HMA/PEO) ₂₂ /P2HMA film exposed to 0.2 mg/mL aqueous solution of <i>d</i> PEO for 10 min. The interfacial widths, σ , are given as full-width-at-half-maximum (FWHM), which is 2.35 times larger than the more commonly used root-mean-squared (RMS).	109
Table C-12 Model parameters for the (P3HAA/PEO) ₁₀ /P3HAA film. The interfacial widths, σ , are given as full-width-at-half-maximum (FWHM), which is 2.35 times larger than the more commonly used root-mean-squared (RMS).	110
Table C-13 Model parameters for the (P3HAA/PEO) ₁₀ /P3HAA film exposed to 0.2 mg/mL aqueous solution of <i>d</i> PEO for 1 min. The interfacial widths, σ , are given as full-width-at-half-maximum (FWHM), which is 2.35 times larger than the more commonly used root-mean-squared (RMS).	110
Table C-14 Model parameters for the (P3HAA/PEO) ₁₀ /P3HAA film exposed to 0.2 mg/mL aqueous solution of <i>d</i> PEO for 2 min. The interfacial widths, σ , are given as full-	

width-at-half-maximum (FWHM), which is 2.35 times larger than the more commonly used root-mean-squared (RMS).	111
Table C-15 Model parameters for the (P3HAA/PEO) ₁₀ /P3HAA film exposed to 0.2 mg/mL aqueous solution of <i>d</i> PEO for 5 min. The interfacial widths, σ , are given as full-width-at-half-maximum (FWHM), which is 2.35 times larger than the more commonly used root-mean-squared (RMS).	111
Table C-16 Model parameters for the (P3HAA/PEO) ₁₀ /P3HAA film exposed to 0.2 mg/mL aqueous solution of <i>d</i> PEO for 10 min. The interfacial widths, σ , are given as full-width-at-half-maximum (FWHM), which is 2.35 times larger than the more commonly used root-mean-squared (RMS).	112
Table C-17 Model parameters for the (P3HMA/PEO) ₄ /P3HMA film exposed to 0.2 mg/mL aqueous solution of <i>d</i> PEO for 1 min. The interfacial widths, σ , are given as full-width-at-half-maximum (FWHM), which is 2.35 times larger than the more commonly used root-mean-squared (RMS).	112
Table C-18 Model parameters for the (P3HMA/PEO) ₄ /P3HMA film exposed to 0.2 mg/mL aqueous solution of <i>d</i> PEO for 2 min. The interfacial widths, σ , are given as full-width-at-half-maximum (FWHM), which is 2.35 times larger than the more commonly used root-mean-squared (RMS).	113
Table C-19 Model parameters for the (P3HMA/PEO) ₄ /P3HMA film exposed to 0.2 mg/mL aqueous solution of <i>d</i> PEO for 5 min. The interfacial widths, σ , are given as full-width-at-half-maximum (FWHM), which is 2.35 times larger than the more commonly used root-mean-squared (RMS).	113

1. INTRODUCTION

1.1. Polyphenols

Antioxidants are an important class of organic compounds which can react with radicals, protecting other molecules from oxidative damage.¹ One abundant class of antioxidants is represented by polyphenols, which contain moieties with two or more phenol groups in the benzene ring. Natural polyphenols can be found in many products such as fruits,² vegetables,³ spices,⁴ teas,⁵ and wines.⁶ In plants, polyphenol compounds are known for exhibiting the antioxidant activity by quenching reactive oxygen species (ROSs)⁷ and thus preventing the oxidative damage in living cells that can be caused by pathogens or ultraviolet radiation.⁸ Besides plants, polyphenols can be found in some marine organisms. For example, the red algae is rich with numerous natural bromophenols,^{9,10} while marine mollusks use 3,4-dihydroxy-L-phenylalanine (DOPA) as a component of an adhesive protein involved in their attachment to surfaces.¹¹

In the world of synthetic products, the use of antioxidants enhances performance of polymers in food packaging¹²⁻¹⁵ and biomedical applications.¹⁶ Since natural polyphenols represent non-polymeric, low molecular weight compounds, blending is the most common way to introducing them into a polymer matrix.¹⁷⁻¹⁹ However, leaching of antioxidants is a well-known issue for blends.²⁰ To prevent leaching, antioxidant groups have been introduced into polymeric materials *via* covalent modification of pre-synthesized polymers,^{16,21-24} such as synthetic reaction with DOPA or dopamine moieties.²⁵⁻³³ Similarly, gallol functional groups were incorporated through chemical modification of some natural polymers, such as gelatin, chitin, chitosan or hyaluronic acid.^{22-24,34,35} A more controllable way to introduce antioxidant units within polymer chains is direct polymerization of antioxidant-bearing monomers.^{36,37} The latter approach allows

for greater control of distribution of the polyphenol species along the polymer chain and yields synthetic polymers which are highly suitable for preparation of antioxidant materials and coatings through sequential assembly of polymers at surfaces.

1.2. Layer-by-layer assembly

A powerful technique to introduce antioxidant species into a surface coating is layer-by-layer assembly.^{38,39} LbL assembly is generally driven by electrostatic interactions,^{38,39} hydrogen bonding,⁴⁰⁻⁴⁵ and/or hydrophobic interactions.⁴⁶ Deposition of LbL films is often achieved by alternating dipping of a substrate in solutions of interacting polymers with an application of rinsing steps in between. A polymer monolayer is adsorbed at each deposition step, leading to a gradual thickness increase. The technique can be used with substrates of various shapes⁴⁷ and provides precise control over film thickness, composition,⁴⁸ and structure⁴⁹ *via* selection of polymer chemistry and assembly conditions. The level of such a control depends on strength of binding between the film components. Strong interpolymer interactions usually lead to kinetically trapped conformations of adsorbed chains, which preserve film layered structure. Such films usually demonstrate linear growth mode with a constant amount of material deposited per each step.^{50,51} In contrast, weak binding enables chain mobility and results in significant polymer intermixing. Such films often exhibit non-linear or exponential growth behavior, with the amount of deposited material increasing per each immersion step.^{49,52-54} Exponentially growing films are not only highly diffusive, but also contain sufficient free volume, swell by entrapping large amounts of a solvent, and exhibit self-healing behavior.^{55,56}

1.3. Goal and Objectives

In this work we focused on how chemistry of the polyphenol ring affects layer-by-layer assemblies of polyphenolic polymers, including their internal structure, swelling behavior, chain dynamics, as well as their functionality, *i.e.* antioxidant activity. To achieve these goals, the following objectives were pursued:

1. To develop a synthetic procedure for preparation of linear polyphenol polymers (*l*PPhs) with controllable composition, hydrophobicity, adsorption, and antioxidant properties. To that end, reversible addition-fragmentation chain transfer polymerization procedures were developed to include catechol, bromocatechol or gallol moieties within polymer chains.
2. To understand the effect of the chemical structure of polyphenol ring and the content of hydrophobic non-phenolic hydrocarbon units on surface adsorption properties of *l*PPhs and their ability to alter and control surface wettability.
3. To study hydrogen-bonded assembly of *l*PPhs with a neutral hydrogen-bonded acceptor polymer within LbL films, explore the effect of chemical structure of polyphenol ring (gallol vs catechol) on polymer-polymer binding, polymer chain mobility, film internal structure, antioxidant activity and self-healing behavior.

2. SYNTHESIS OF LINEAR POLYPHENOL POLYMERS*

2.1. Abstract

A series of linear polymeric antioxidants with controllable antioxidant, hydrophobicity and surface adsorption properties was synthesized using reversible addition–fragmentation chain transfer (RAFT) polymerization. The polymers had a poly(methacrylamide) backbone and contained functional catechol-like 3,4-dihydroxybenzyl-, gallol-like 3,4,5-trihydroxybenzyl- and bromo-substituted 3,4-dihydroxy-5-bromobenzyl-(2H, 3H and BrH, respectively) groups, as well as N-hexyl (Hex) moieties. The polymers were abbreviated as P2H_ZHex, P3H_ZHex or PBrH_ZHex, where Z is the molar percentage of the polyphenol units in the polymer chains. Both the chemical functionality and the relative content of the polyphenol and hexyl units governed the hydrophobicity, adsorption and antiradical activity of these polymers. An increase in the content of the hexyl units in the polymer chains resulted in higher thicknesses of the adsorbed polymer monolayers and an increase in the water contact angles of the gold surface. Importantly, polymers with gallol-like side groups exhibited antioxidant activity (as determined using the DPPH assay in methanol solutions) and affinity to metal substrates that were superior to those of their catechol-like and bromo-substituted counterparts. The tunability of interfacial binding, hydrophobicity and antioxidant properties of these polymers are properties essential for the use of these polymers in coating applications.

2.2. Introduction

Inspiration for synthesis of phenolic polymers stems from natural polyphenols – low molecular weight compounds containing di- or trihydroxy benzene moieties that demonstrate

*A family of linear phenolic polymers with controlled hydrophobicity, adsorption and antioxidant properties. R. Hlushko, H. Hlushko and S. A. Sukhishvili, *Polym. Chem.*, 2018, **9**, 506 – Reproduced in part by permission of The Royal Society of Chemistry

radical scavenging, antioxidant activity, and metal-binding properties.^{1,57-61} In the most part, natural polyphenols are known as low molecular weight antioxidants abundant in plants,⁶² fruits,⁶³ or marine algae.^{9,10} One well-known antioxidant natural polyphenol – tannic acid (TA) – contains multiple 3,4,5-trihydroxybenzoyl (galloyl) groups arranged in a star-shaped molecular architecture. TA has been extensively studied in its free form in solution,⁶⁴ as well as in its complexes and layer-by-layer films with polymers⁶⁵⁻⁶⁷ and/or metal ions.^{68,69}

Incorporation of polyphenol moieties within synthetic polymers provides polymer materials with controllable properties, such as adhesive and gelation. So far, this strategy has been primarily explored with polymers that contain dihydroxybenzyl (catechol) moiety that mimics mussel adhesive proteins^{70,71} – the strongest natural adhesive materials containing up to 30% percent of 3,4-dihydroxy-L-phenylalanine.⁷²⁻⁷⁴ Synthetic polymers that contain DOPA or dopamine moieties constitute the basis for novel “wet” adhesives^{25,27,28,75} and self-healing materials.²⁹⁻³³ Several polymerization routes including free-radical,⁷⁶ anionic,⁷⁷ and reversible addition-fragmentation chain transfer polymerization^{78,79} were developed to introduce catechol groups to synthetic polymers. In particular, catechol functionality was included in carbon-chain^{76,79,80} and biodegradable polymers⁸¹ and was made part of copolymers,^{76,77} block copolymers,⁷⁹ or homopolymers.⁷⁸

While low-molecular-weight natural polyphenols containing gallol moieties or highly abundant bromocatechol antioxidants extracted from *Red Algae*^{9,10} have been known to exhibit high antioxidant activity,^{82,83} in contrast to catechol moieties they are rarely used in a buildup of polymer chains. In existing reports on synthetic polymers containing gallol groups, these functional groups were introduced in polymers or hydrogels by chemical modification of natural polymers^{22-24,35} rather than by direct polymerization of synthetic monomers. To the best of our

knowledge, synthetic polymers with bromo-polyphenol side groups have not been previously reported, whereas only two studies describe incorporation of gallol functionality in synthetic polymers with well-defined molecular architecture and composition. In one of these studies, gallol moiety was linked to imidazolium units to enable simultaneous electronic and ionic conductivities in a poly(ionic liquid).⁸⁴ In another related work, polyphenol moieties were included within polymers, whose preparation involves the use of organophosphorus compounds for monomer synthesis.^{37,85} Moreover, this earlier work was restricted to polymers with the polystyrene backbone.

Here we report a synthetically simple yet versatile procedure to synthesize a broad range of linear antioxidant homo- and copolymers with controlled hydrophobicity, adsorption and antioxidant properties that include catechol, gallol, or bromocatechol moieties. This study explores the effects of the chemical structure and content of polyphenol groups in polymer chains on their antioxidant activity in solution and the capability to adsorb on and modify wettability of solid surfaces.

2.3. Experimental Section

2.3.1. Materials

1,4-Dioxane, azobisisobutyronitrile (AIBN), 2-cyano-2-propyl dodecyl trithiocarbonate (CPD-TTC), deuterated chloroform (CDCl_3), deuterated dimethyl sulfoxide (DMSO-D_6), deuterated methanol (CD_3OD), bromine, sodium hydroxide (NaOH), hydrochloric acid (HCl), boron tribromide, and polystyrene standards were purchased from Sigma Aldrich. Acetone and hexylamine were purchased from EMD Millipore. Sodium carbonate, glacial acetic acid, and methanol were purchased from Avantor Performance Materials, Inc. Diphenyl-1-picrylhydrazyl (DPPH), sodium tetraborate decahydrate (borax), aluminum oxide, methacrylic anhydride, 3,4-

dimethoxybenzylamine, 3,4,5-trimethoxybenzylamine, magnesium sulfate, tetrahydrofuran (THF), and dichloromethane were purchased from Alfa Aesar. Dimethylformamide (DMF) was purchased from BDH VWR Analytical. AIBN was recrystallized from methanol prior to use. All solvents and monomers were purified from stabilizers by passing through a column packed with basic aluminum oxide with pore size of 58 Å. All other chemicals were used as received.

QCM O100RX1 chromium-gold crystals were purchased from Stanford Research Systems and used as substrate to study adsorption of polymers using ellipsometry.

2.3.2. Characterization Methods

Gel Permeation Chromatography (GPC) was performed using an Agilent Technologies GPC system equipped with Agilent 1260 infinity multi suite (refractive index and viscosity) detectors at 30°C. A Phenogel™ column (Phenomenex) with the particle size of 5 µm and the pore size of 10³ Å was used for characterization of 1 to 5 g L⁻¹ polymer solutions. THF was used as an eluent for kinetics studies. 0.01 M LiBr in DMF was used for characterization polyphenol precursors as well as deprotected polymers. All solutions were eluted at a rate of 0.15 mL min⁻¹ and 0.10 mL min⁻¹, at a temperature of 30°C. The presence of 0.01 LiBr has enabled disruption of hydrogen bonds between polyphenol groups of unprotected polymers.

¹H Nuclear Magnetic Resonance (¹H NMR) characterization of monomers and polymers was performed with a VARIAN Mercury 300 NMR SPECTROMETER with an Oxford Instruments Ltd. superconducting magnet, using CDCl₃, DMSO-D₆, or methanol-D₄ as solvents. The data were processed with a VarianJ software.

Fourier transform infrared (FTIR) analysis was performed using a Bruker Tensor II spectrometer equipped with a mercury cadmium telluride (MCT) detector. The spectra were

recorded by accumulating 96 scans within a spectral range of 900-4000 cm^{-1} at a resolution of 4 cm^{-1} .

Polymer adsorption. QCM O100RX1 chromium-gold crystals were used as a substrate in the studies of polymer adsorption. Prior to experiments, the substrates were cleaned by an overnight exposure to UV radiation at a wavelength of 185 nm supplied by a Mercury Grid Lamp, BHK Inc. The crystals were then rinsed with deionized water, dried in a flow of dry nitrogen gas, and additionally exposed to UV for 5 min prior to the adsorption experiments. All polymers were allowed to adsorb on gold substrates from 1.0 mg mL^{-1} solutions in methanol for 60 minutes. The substrates were then rinsed three times with methanol and dried in a flow of dry nitrogen gas prior to measurements.

Spectroscopic ellipsometry. Dry thicknesses of polymer monolayers adsorbed on gold substrates were determined using a variable angle spectroscopic ellipsometer (VASE) M-2000V (J. A. Woollam Co., Inc.). Measurements were performed at four incidence angles of 45°, 55°, 65°, and 75°. The gold surface was fitted as B-spline material with the complex dielectric function $\varepsilon = \varepsilon_1 + i\varepsilon_2$. Prior to the film thickness measurements, the values ε_1 and the amplitude of a zero energy oscillator (Drude term) for the Kramers-Kronig transformation of ε_2 were determined for each gold substrate.

Thin polymer films were treated as a Cauchy material with a thickness d and the wavelength dependence of the refractive index n described by the following equation: $n(\lambda) = A + B/\lambda^2 + C/\lambda^4$, where λ is a wavelength; and A , B , and C are fitting coefficients. The refractive index for dry polymer films was fixed at 1.50.

Contact angle (CA) measurements of bare gold substrates as well as substrates covered with adsorbed polymer monolayers were performed using an optical contact angle meter CAM

101 (KSV Instruments). Milli-Q water with resistivity of 18.2 M Ω cm (EMD Millipore) was used for CA measurements.

2.4. Synthetic Protocols

2.4.1. Synthesis of Monomers

Synthesis of N-hexyl methacrylamide (1). First, 15.0 g of borax (decahydrate) [39.3 mmol] and 15.0 g of anhydrous sodium carbonate [142 mmol] were dissolved in 400 ml of deionized water, and the solution was purged with argon gas for 120 min. Then 13.2 mL [99.9 mmol] of hexyl amine was slowly added to the solution during 15 min under continuous stirring. In a separate flask, 17.0 mL of methacrylic anhydride [97.4 mmol] was dissolved in 30.0 mL of THF; this solution was added dropwise to the hexyl amine solution under vigorous stirring at ~1000 rpm. The mixture was stirred for 24 h at room temperature, and the product was extracted in 150 mL of dichloromethane three times. The extract was washed with 0.1 M NaOH and 0.1 M HCl, while applying repeated washing steps after both basic and acidic treatments, and finally dried over anhydrous MgSO₄. The residual solvent was removed under vacuum to yield viscous colorless liquid (yield 74.6%).

N-hexyl methacrylamide (**1**) ¹H-NMR (300 MHz, CDCl₃): δ : 7.26 (solvent), 5.72-5.94 m (1H, -NH-), 5.65 s (1H, CHH=); 5.29 s (1H, CHH=); 3.27 t (2H, -NHCH₂CH₂-); 1.94 s (3H, CH₃-C(CH₂)CO-); 1.52 m (2H, -NHCH₂CH₂-); 1.29 m (6H, -NHCH₂CH₂(CH₂)₃CH₃); 0.87 t (3H, -NHCH₂CH₂(CH₂)₃CH₃)

It should be noted that while 3,4-dimethoxybenzyl amine (**2**) and 3,4,5-trimethoxybenzyl amine (**4**) used for polymer synthesis are commercially available, 3,4-dimethoxy-5-bromobenzyl amine (**3**) is not commercially available and was synthesized as described below.

Synthesis of 3,4-dimethoxy-5-bromobenzyl amine (3). 1.00 g of 3,4-diethoxybenzylamine (2) [6.63 mmol] was dissolved in 10.0 mL of glacial acetic acid. Then 0.342 mL of liquid bromine was added dropwise to thaw solution under rigorous steering, and the mixture was heated at 50°C for 3 hours. The product was dried under vacuum to yield a white solid (yield 98.8%). ¹H-NMR, (300 MHz, DMSO-d₆): δ 6.72 d (1H, C₆H₄HBr(OCH₃)₂); 6.63 d (1H, C₆H₄HBr(OCH₃)₂); 3.76 s (2H, -CH₂-); 3.68 s (6H, C₆H₂Br(OCH₃)₂); 2.49 s (solvent).

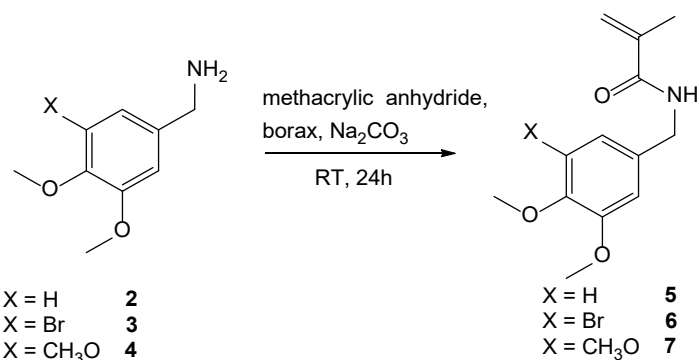


Figure 2-1 Generalized representation of synthesis of precursors of phenolic monomers.

Synthesis of monomers. In a typical procedure, Figure 2-1, 5.00 g of borax (decahydrate) [13.1 mmol] and 5.00 g of anhydrous sodium carbonate [47.2 mmol] were dissolved in 150 mL of water in a 250-mL two-neck round-bottom flask. The solution was purged with argon for two hours prior to the addition of one of the following amines: 3,4-dimethoxybenzyl amine (2) (2.00 mL [13.3 mmol]), 3,4-dimethoxy-5-bromobenzyl amine (3) (2.00 g [6.37 mmol]), or 3,4,5-trimethoxybenzyl amine (4) (2.80 g [10.6 mmol]). After complete dissolution of amines, a stoichiometric amount of methacrylic anhydride in 10.0 mL of THF was slowly added to the mixture under intense stirring. The solution was continuously stirred for 24 hours at room temperature, and the reaction products extracted with dichloromethane (50 mL) three times. The extract was sequentially washed with 0.1 M NaOH, 0.1 M HCl, and deionized water, and dried

over anhydrous MgSO₄. The residual solvent was removed under vacuum to yield a white solid [yield: 74.7% for N-(3,4-dimethoxybenzyl) methacrylamide (**5**), 73.8% for N-(3,4-dimethoxy-5-bromobenzyl) methacrylamide (**6**), and 73.5% for N-(3,4-trimethoxybenzyl) methacrylamide (**7**)].

N-(3,4-dimethoxybenzyl) methacrylamide (**5**) ¹H-NMR (300 MHz, DMSO-d₆): δ 8.2 t (1H, -NH-); 6.5 - 6.6 d (3H, C₆H₃(OCH₃)₂); 5.69 s (1H, CHH=); 5.35 s (1H, CHH=); 4.23 -4.25 d (2H, -CH₂-); 3.71 - 3.73 d (6H, -C₆H₃(OCH₃)₂); 2.49 s (solvent), 1.87 s (3H,CH₃-).

N-(3,4-dimethoxy-5-bromobenzyl) methacrylamide (**6**) ¹H-NMR (300 MHz, DMSO-d₆): δ 8.2 t (1H, -NH-); 6.5 - 6.6 d (2H, C₆H₂Br(OCH₃)₂); 5.69 s (1H, CHH=); 5.35 s (1H, CHH=); 4.23-4.25 d (2H, -CH₂-); 3.71 - 3.73 d (6H, -C₆H₂Br(OCH₃)₂); 2.49 s (solvent), 1.87 s (3H,CH₃-).

N-(3,4,5-trimethoxybenzyl) methacrylamide (**7**) ¹H-NMR (300 MHz, DMSO-d₆): δ 8.2 t (1H, -NH-); 6.5 - 6.6 d (2H, C₆H₂(OCH₃)₃); 5.69 s (1H, CHH=); 5.35 s (1H, CHH=); 4.23 -4.25 d (2H, -CH₂-); 3.71 - 3.73 d (9H, -C₆H₂(OCH₃)₃); 2.49 s (solvent), 1.87 s (3H, CH₃-).

2.4.2. RAFT Polymerization of Monomers

Individual monomers (**5**, **6**, and **7**) or their mixtures with N-hexyl methacrylamide (**1**) (to obtain homopolymers or copolymers, respectively) in the total amount of 11.5 mmol were placed in a Schlenk flask, sealed, deaerated under vacuum, and filled with argon gas. Tables A-1–A-3 in the Appendix A section specify the amounts of monomers used for synthesis of various polymers. After addition of 2.00 mL of anhydrous 1,4-dioxane, the solutions were stirred at room temperature. In a separate container, 20.0 mg of AIBN [0.122 mmol] and 250 μL of CPD-TTC [0.717 mmol] were dissolved in 5.00 mL of anhydrous 1,4-dioxane, and a 0.400 mL aliquot of this solution was added to the Schlenk flask. After three vacuum-thaw cycles, the tube was sealed and polymerization was allowed to proceed at 70°C for 48 hours. After completion of polymerization,

the reaction mixtures were cooled to room temperature and diluted with 13.0 mL of THF. Polymer solutions in THF were added drop-by-drop to 200 mL of n-hexane at vigorous stirring, precipitated polymers were filtered, washed with 100 mL of n-hexane, and dried under vacuum.

2.4.3. Demethylation

Approximately 0.5 g amounts of each polymer (Tables A-1–A-3) were dissolved in 15 mL of anhydrous CH_2Cl_2 in the Schlenk flask. After three freeze-thaw cycles, the mixtures were placed in the chlorobenzene slush cooling bath which maintained a temperature of -45°C . Then ~ 1.5 molar excess of 2 M BBr_3 solution in CH_2Cl_2 (calculated as a molar ratio of BBr_3 to $-\text{OCH}_3$ groups) was added drop-by-drop to the reaction mixtures under intense stirring. After 30 min, Schlenk flasks were allowed to slowly warm overnight to room temperature. Then 20 mL of 1% HCl in degassed water was carefully added to the flask. Finally, the mixture was stirred for 2 hours, filtered in inert atmosphere, and dried under vacuum. The homopolymers were abbreviated as PXYMA, where X is used to identify various substituents in the polyphenol ring ($X = 2$ for catechol, $X = \text{Br}$ for bromocatechol, and $X = 3$ for gallol units), Y denotes either methoxy protecting group ($Y = \text{M}$) or deprotected hydroxyl group ($Y = \text{H}$) in the benzene ring of precursor and deprotected polymers, respectively. Poly(N-hexyl methacrylamide) is abbreviated as PHex. In the case of copolymers, an abbreviation PXY_ZHex is used, where Z denotes the molar percentage of polyphenol units in the polymer chains. For example, poly(N-(3,4-dimethoxy-5-bromobenzyl) methacrylamide) and poly(N-(3,4,5-trihydroxybenzyl) methacrylamide) homopolymers are abbreviated as PBrMMA and P3HMA, respectively. At the same time, poly[(N-(3,4-dimethoxybenzyl) methacrylamide)-*co*-(N-hexyl methacrylamide)] copolymer with 10% of phenolic units and poly[(N-(3,4,5-trihydroxybenzyl) methacrylamide)-*co*-(N-hexyl methacrylamide)] with 15% of phenolic groups are abbreviated as $\text{P2M}_{10}\text{Hex}$ and $\text{P3H}_{15}\text{Hex}$, respectively.

2.4.4. Studies of polymerization kinetics

Kinetics of polymerization was studied for copolymers with varied chemistry of polyphenol units but the same targeted composition. To that end, mixtures with a 1:9 molar ratio of N-(3,4-dimethoxybenzyl) methacrylamide (**5**), N-(3,4-dimethoxy-5-bromobenzyl) (**6**), or N-(3,4,5-trimethoxybenzyl) methacrylamide (**7**) with N-hexyl methacrylamide (**1**) were prepared to obtain P2M₁₀Hex, PBrM₁₀Hex, and P3M₁₀Hex copolymers, respectively. In addition to polyphenolic copolymers, homopolymerization of N-hexyl methacrylamide was explored. To study the effect of temperature, the polymerization was conducted at 60, 70 or 80°C. In all cases, 100- μ l aliquots were taken hourly from the polymerization solutions, diluted with 1 mL of THF and cooled down to -18°C to stop polymerization. The molecular weights of the polymers at each time point were determined by GPC equipped with the Phenogel™ column calibrated using polystyrene standards.

2.5. Results and Discussion

2.5.1. Synthesis and characterization of phenolic polymers

The synthesis of a series of phenolic polymers *via* RAFT polymerization is summarized in Figure 2-2. A commercially available chain transfer agent (CTA) – 2-cyano-2-propyl dodecyl trithiocarbonate – was chosen as being the most suitable for synthesis of methacrylate monomers.⁸⁶ The [monomer]/[CTA]/[AIBN] ratio was fixed at a constant value of 200/1/0.17 in order to obtain a polymer series with similar polymerization degrees.

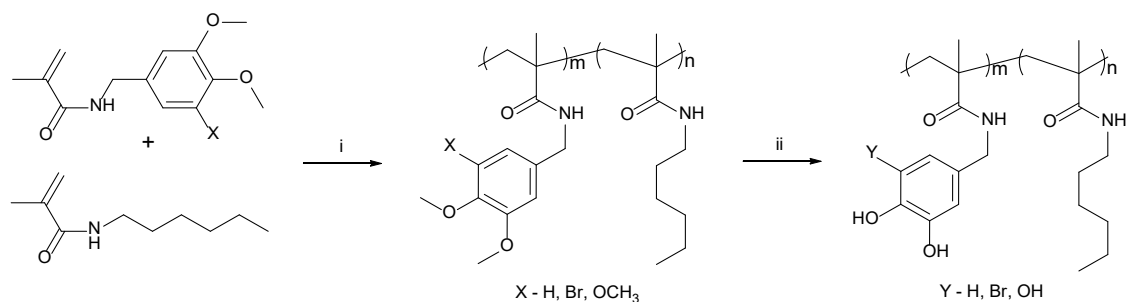


Figure 2-2 General synthesis of phenolic polymers. (i) AIBN and CPD-TTC as CTA in dioxane at 70°C for 12-24 hours. (ii) (a) BBr₃ in CH₂Cl₂ at -45°C to RT for 2 hours, (b) 1% HCl for 2 hours.

The polymerization process was strongly affected by temperature. Specifically, the use of 60 or 80 °C did not result in controlled growth of polymer chains. No polymeric products were formed for as long as 8 hours when polymerization was performed at 60°C (data not shown). At the same time, an increase in polymerization temperature to 80°C caused fast (completed within two hours) formation of polymer products with high polydispersity (Figure. A-1). The poor control of the polymer chain growth at 80°C is likely a result of a high dissociation rate of the initiator and the fast chain propagation rate.⁸⁷ In contrast, the use of 70°C for polymerization supported moderate polymerization rates and enabled good control of the growing chains. Therefore, 70°C was selected for polymerization of all monomers in this work.

To demonstrate living nature of polymerization, 1:9 molar mixtures of N-(3,4-dimethoxybenzyl) methacrylamide, N-(3,4-dimethoxy-5-bromobenzyl), or N-(3,4,5-trimethoxybenzyl) methacrylamide with N-hexyl methacrylamide, or pure N-hexyl methacrylamide were polymerized to obtain P2M₁₀Hex, PBrM₁₀Hex, P3M₁₀Hex copolymers or PHex homopolymer, respectively. At specific points of time during polymerization at 70°C, 0.1-mL aliquots of the reaction mixture were taken, diluted with 1 mL of THF, cooled down to -18°C to stop polymerization reaction, and polymer products were analyzed using GPC and ¹H NMR

(Figure A-1 and A-2). Figure 2-3 illustrates that the kinetics plots for all polymers were linear up to 10 hours, indicating good control of chain propagation during polymerization.

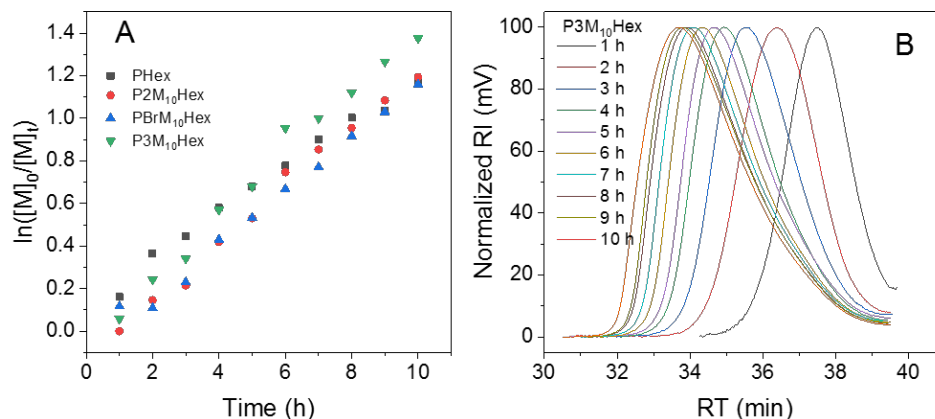


Figure 2-3 Time evolution of $\ln([M]_0/[M]_t)$ during synthesis of PHex homopolymer and copolymers containing 10% of phenolic precursor groups (A), as well as representative GPC traces shown for synthesis of P3M₁₀Hex interrupted at various polymerization times (B) when polymerization was carried out at 70°C.

After establishing living nature of polymerization, a range of phenolic copolymers with varied density of phenolic groups in the polymer chains, as well as polyphenolic homopolymers were synthesized using the established protocol while allowing polymerization to proceed to high conversion degrees. All polymers were deprotected as described in the Experimental Section to yield polymers with active phenolic groups.

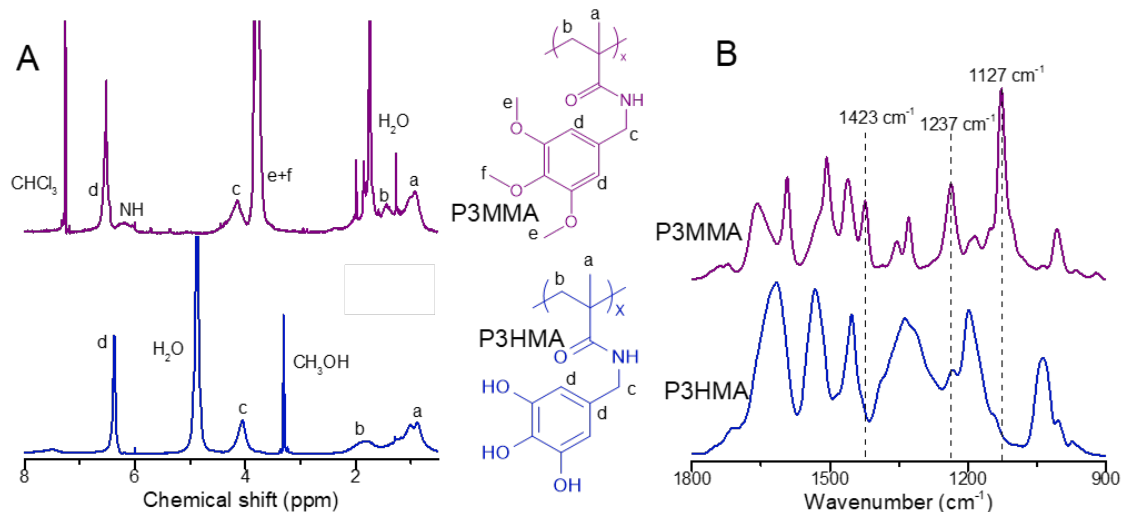


Figure 2-4 ¹H NMR spectra of P3MMA in CDCl₃ (purple) and P3HMA in CD₃OD (blue) (A); FTIR spectra of P3MMA (purple) and P3HMA (blue) (B). The 3500-1800 cm⁻¹ region is shown in the Appendix A, Figure A-3.

Figure 2-4 compares the data of ¹H NMR and FTIR characterization of homopolymers before and after deprotection of phenolic groups, while Figure 2-4 presents typical results of characterization of protected and deprotected copolymers. In the case of protected P3MMA and deprotected P3HMA homopolymers, aromatic protons in polyphenol ring at 6.5-6.6 ppm (Figure 2-4A, d) aliphatic protons of the polymer backbone at 0.7-2 ppm (Figure 2-4A, a and b) are clearly seen in both cases. However, the spectra are clearly distinct in the 3.6-3.9 ppm range characteristic of methoxy protons (e and f), suggesting complete removal of methoxy protection and conversion of P3MMA to P3HMA. Additionally, complete deprotection of polyphenol units was confirmed by FTIR analysis. Figure 2-4B shows that vibrational bands at 1127 cm⁻¹, 1237 cm⁻¹, and 1423 cm⁻¹ associated with O-CH₃ (ether) stretching, aryl-O (ether) stretching, and -CH₃ rocking vibrations and characteristic of the protected polymers have disappeared in the deprotected polymer. Moreover, an additional wide band at ≈3200 cm⁻¹ associated with O-H stretching vibrations⁸⁸ emerged in the FTIR spectra of the deprotected polymer (Figure A-3).

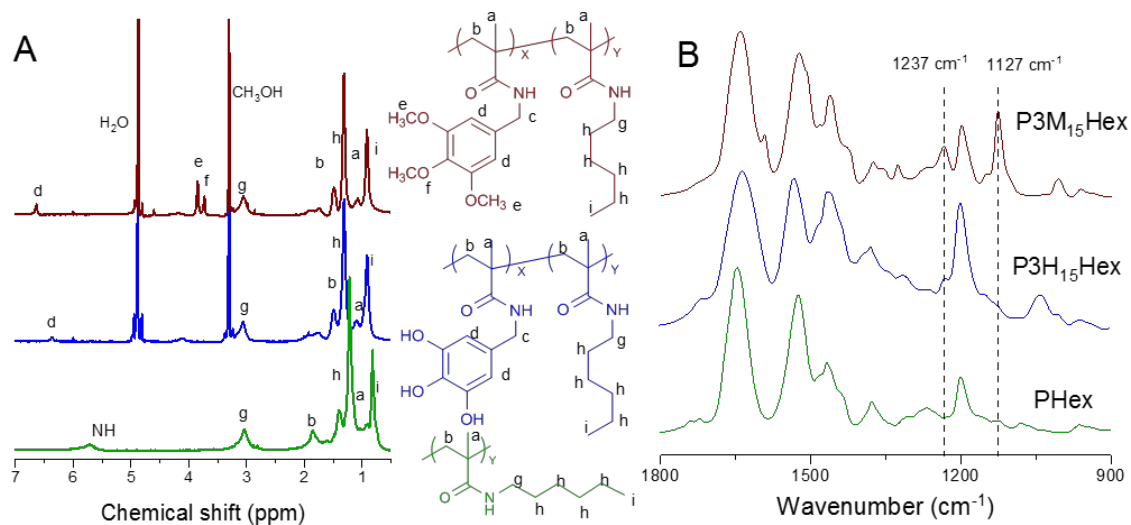


Figure 2-5 ^1H NMR spectra of P3M₁₅Hex (maroon) and P3H₁₅Hex (blue) in CD₃OD, as well as PHex (green) in CDCl₃ (A); FTIR spectra of P3M₁₅Hex (maroon), P3H₁₅Hex (blue), and PHex (green) (B).

Typical results of characterization of the copolymers are shown in Figure 2-5 for the case of a precursor P3M₁₅Hex and a deprotected P3H₁₅Hex copolymers. The ^1H NMR data confirm the presence of both phenolic and hexyl monomeric units in the polymer chain. The peaks at 6.5–6.8 ppm characteristic of aromatic protons (Figure 2-5A, d), as well as the peaks at 0.7–1.5 ppm (h) and 2.9–3.3 ppm (g) characteristic of n-hexyl groups are present in both the protected and deprotected copolymers. However, similarly to the case of homopolymers, the characteristic peaks of the methoxy protons at 3.6–3.9 ppm disappeared in the spectra of deprotected P3H₁₅Hex, confirming complete removal of the protecting methyl groups from the phenolic rings. The FTIR data for the copolymers in Figure 2-5B are fully consistent with ^1H NMR results, *i.e.* they show absence of 1127 cm^{-1} and 1237 cm^{-1} bands associated with O–CH₃ vibrations in the deprotected polymer. The strong intensities of vibrational bands at 2960–2860 cm^{-1} in both protected and deprotected P3M₁₅Hex and P3H₁₅Hex copolymers indicate the presence of hexyl-monomer units (Figure A-3). FTIR spectra of all other homopolymers and copolymers are shown in the Supporting

Information section (Figure A-4 and A-5, respectively). FTIR and ^1H NMR also confirmed that demethylation procedure did not result in cleavage of the amide groups.

In the copolymer synthesis, a varied molar content of phenolic units of 5, 10 and 15% was targeted *via* the use of the feed ratios of the phenolic monomer precursors to hexyl monomer of 1:19, 1:9, and 3:17, respectively. For all the copolymers, the compositions calculated from the integrated peak intensities of methoxy groups (3.6-3.9 ppm, e+f) and n-hexyl groups (2.9-3.3 ppm, g) in the ^1H NMR spectra were in good agreement with the designed polymer composition (Table 2.1). Note that while all polymers were soluble in a range of polar solvents, including ethanol, methanol, isopropyl alcohol and DMSO, their solubility in less polar tetrahydrofuran was limited to the polymers that contain hexyl moieties. Specifically, P3HMA and P2HMA homopolymers that lacked hexyl groups were not soluble in THF. All polymers were not soluble in water.

Table 2-1 Compositions, Molecular Weight and Polydispersity of Antioxidant Polymers

Designed molar percent of phenolic units, %	Actual molar percent of phenolic units (based on ^1H NMR of protected polymers), %	Protected polymers			Deprotected polymers		
		Abbreviation	M_n , $\text{kg}\cdot\text{mol}^{-1}$	\bar{D}	Abbreviation	M_n , $\text{kg}\cdot\text{mol}^{-1}$	\bar{D}
0	-	PHex	29.2	1.19	-	-	-
5	4.9±0.2	P2M ₅ Hex	24.4	1.21	P2H ₅ Hex	24.4	1.22
10	11.0±0.1	P2M ₁₀ Hex	26.1	1.18	P2H ₁₀ Hex	26.5	1.27
15	19.4±2.0	P2M ₁₅ Hex	21.9	1.26	P2H ₁₅ Hex	29.2	1.12
100	-	P2MMA	38.1	1.15	P2HMA	35.9	1.20
5	5.7±1.0	PBrM ₅ Hex	24.2	1.46	PBrH ₅ Hex	21.6	1.64
10	8.1±1.8	PBrM ₁₀ Hex	30.3	1.21	PBrH ₁₀ Hex	27.7	1.37
15	14.0±2.0	PBrM ₁₅ Hex	26.6	1.25	PBrH ₁₅ Hex	27.1	1.38
100	-	PBrMMA	54.5	1.10	PBrHMA	64.1	1.11
5	6.0±1.9	P3M ₅ Hex	24.4	1.26	P3H ₅ Hex	26.3	1.24
10	8.7±3.6	P3M ₁₀ Hex	26.6	1.28	P3H ₁₀ Hex	32.5	1.19
15	14.8±4.0	P3M ₁₅ Hex	25.9	1.27	P3H ₁₅ Hex	31.9	1.23
100	-	P3MMA	49.6	1.17	P3HMA	43.4	1.45

2.6. Surface Adsorption of Polyphenolic Polymers

The capability of polyphenol groups to adhere to surfaces has been explored in many mussel-mimicking catechol-containing polymers.^{25,27,28,75} Here, we explored the effect of the polyphenol unit chemical structure and their content in the polymer chains on the capability to adsorb to a gold substrate. To that end, the surface of gold-sputtered QCM crystals was pre-cleaned as described in the Experimental Section, brought in contact with 1.0 mg mL⁻¹ polymer solutions in methanol for 1 hour, and thoroughly rinsed with methanol. The amounts of polymers adsorbed within surface monolayers were then determined from ellipsometric measurements of thicknesses of adsorbed layers when fixing the refractive index of adsorbed polymers at 1.50, and assuming the density of dry polymer films of 1 g cm⁻³. Fig. 2-6A shows ellipsometric thicknesses of adsorbed polymer monolayers for a series homopolymers. Thicknesses of adsorbed polymer monolayers are defined by the conformation of polymer chains that can be represented by loops, trains, and tails of polymer units.⁸⁹ Among polyphenolic homopolymers, P3HMA homopolymer formed the thickest monolayer of $\sim 3.3 \pm 1.0$ nm, P2HMA showed an intermediate thickness of 2.0 ± 0.7 nm, and PBrHMA homopolymer formed the thinnest layer with 1.3 ± 0.4 nm thickness. This trend can be explained by a varied strength of intramolecular hydrogen bonding between polyphenolic units included within loops of the adsorbed polymers. P3HMA homopolymer can form stronger hydrogen bonds within the polymer loops because of larger number of hydroxy groups per polymer ring,⁹⁰ and therefore yields thicker adsorbed layers. Note that control PHex polymer that did not contain phenolic groups formed the thinnest layers with the average thickness of 0.6 ± 0.3 nm. This

is likely due to an incomplete monolayer coverage caused by low affinity of nonpolar hydrocarbon units to gold surface.

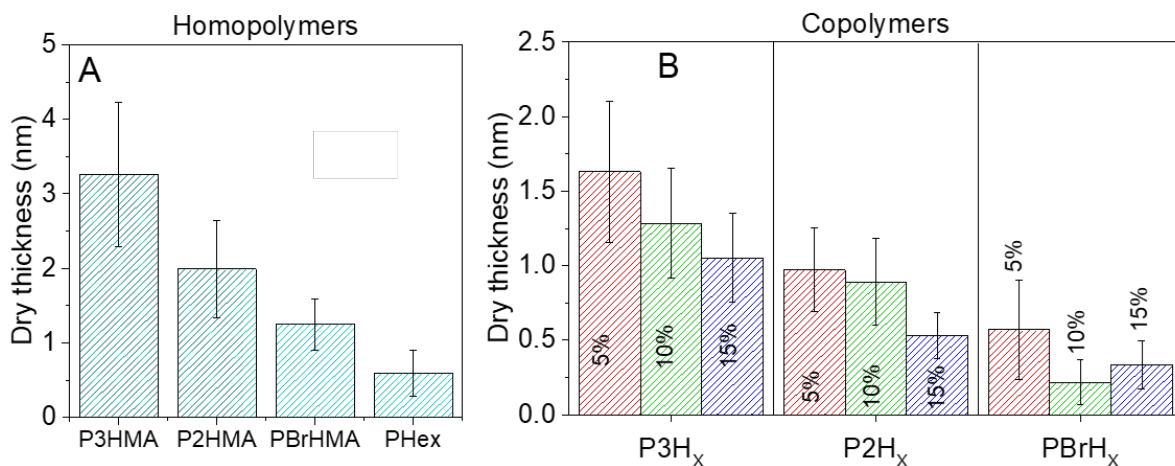


Figure 2-6 Adsorption of polymers at the surface of gold substrates: dry thicknesses of monolayers of homopolymers (A) and copolymers (B) adsorbed from 1.0 mg mL⁻¹ methanol solutions.

Fig. 2-6B shows that a similar trend was also observed for a series of copolymers. The highest amounts adsorbed were detected for gallol-containing polymers within copolymers with the same content of phenolic groups (5, 10 or 15%). Another trend is that the copolymers with the same chemistry of phenolic units formed thinner monolayers as content of phenolic groups in the polymer chains increased. For example, gallol-containing copolymers yielded monolayers with dry thicknesses 1.65 ± 0.50 , 1.3 ± 0.40 , and 1.0 ± 0.30 nm in the case of P3H₅Hex, P3H₁₀Hex, and P3H₁₅Hex, respectively. Such a dependence is reminiscent of a decrease in layer thickness with an increase of charge density of polyelectrolytes,⁹¹ and reflects flattening of polymer chains when the density of surface-adsorbing groups is increased. Taken together, these results indicate that the polyphenol rings play a central role in binding at surfaces and defining the amount of adsorbed polymers, while hexyl and bromide functionalities do not significantly contribute to the interfacial activity of the polymers.

The capability of polyphenol polymers to adsorb to substrates can be used to control the surface wettability. Bare pre-cleaned gold substrates before or after exposure to pure methanol and drying remained fully wettable by deionized water, *i.e.* water contact angles on these surfaces were close to 0°. However, wettability of surfaces was significantly affected by polymer adsorption (Figure 2-7). As the most hydrophobic of the polymers, PHex caused the largest increase in the surface contact angle despite its smallest amount adsorbed.

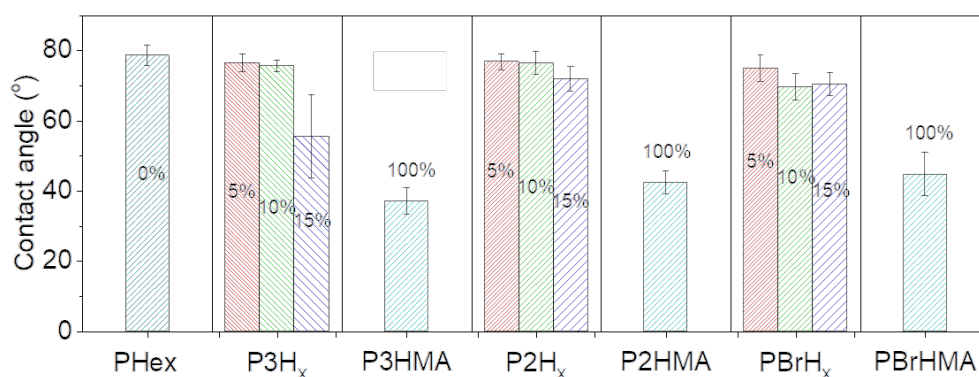


Figure 2-7 The effect of adsorbed polymer monolayers on water contact angles measured on gold surfaces coated with adsorbed monolayers of the antioxidant homopolymers and copolymers.

An increase in the content of polyphenol units up to 10% did not significantly alter surface wettability which remained similar to that resulted from PHex adsorption. A larger than 10% increase in the percentage of phenolic units in the copolymers caused a pronounced increase in surface wettability, with the strongest effect observed with polyphenolic homopolymers. The contact angles of water measured with monolayers of gallol- and catechol-containing polymers increased from 0° for bare gold surface to 37±4° and 42±3° for P3HMA and P2HMA, respectively, reflecting higher hydrophobicity of catechol groups as compared to gallol moieties. A homopolymer with bromocatechol groups (PBrHMA) resulted in contact angles which were similar to those observed with P2HMA. Importantly, among various copolymers, the copolymers

containing gallol groups were unique in their capability to alter surface wettability in the widest range of polymer compositions. This is illustrated by the capability of P3H_xHex copolymers to fine tune the surface wettability between $78\pm 3^\circ$ and $37\pm 4^\circ$ when the content of gallol groups was varied between 0 and 100%.

2.7. Conclusions

This work demonstrates a facile synthesis of a family of polyphenolic polymers with various chemistries of the polyphenol groups, whose antioxidant properties and the capability to adsorb at surfaces and alter the surface wettability can be pre-programmed at the step of polymer synthesis. Several types of antioxidant groups including catechol, bromocatechol, and gallol were introduced in homopolymers and copolymers via RAFT polymerization. A comparative study of the antioxidant activity and surface adsorption properties of the polymers revealed the superior performance of the gallol-type polymers as compared to those of the catechol- and bromocatechol-type polymers. The capability of tuning the functionality of the antioxidant copolymers via “diluting” the polyphenol groups within the polymer chains through copolymerization with inert hydrophobic polymer units enables the control of the adsorption of these polymers at solid surfaces and allows the creation of antioxidant surfaces with controlled wettability. These features might be useful in many future applications of these polymers, especially those related to food packaging, pharmaceuticals, and anticorrosion coatings.

2.8. Acknowledgements

This work was supported by the NSF under Award DMR-1610725, and by Texas A&M University and Texas A&M Experimental Engineering Station (TEES).

3. LAYER-BY-LAYER HYDROGEN-BONDED ANTIOXIDANT FILMS OF LINEAR SYNTHETIC POLYPHENOLS*

3.1. Abstract

We report on the role of the chemical structure of polyphenol pendant groups in linear antioxidant polymers on their assembly and chain intermixing within layer-by-layer films, as well as on the antioxidant performance of the interfacial assemblies. When assembled with poly(ethylene oxide) (PEO) within hydrogen-bonded films, the antioxidant polymers – poly(3,4-dihydroxybenzyl methacrylamide) and poly(3,4,5-trihydroxybenzyl methacrylamide) – which contained catechol-like and gallol-like moieties, respectively, generated films with drastically different structure and functionality. Specifically, while catechol-based P2HMA deposited within LbL films linearly with a low increment of mass increase per step, growth of P3HMA/PEO films was strongly exponential, probably because of self-association of gallol-like polyphenol units in P3HMA. Dramatic differences in chain intermixing and layering in these films are revealed by the application of neutron reflectometry using deuterated PEO, *d*PEO, to create marker layers. The differences in the film structure strongly affected film antioxidant performance, as demonstrated by radical scavenging assay. While assembled P3HMA was fully available for scavenging 2,2'-azino-bis(3-ethylbenzothiazoline-6-sulfonic acid) (ABTS^{•+}) radical cations, in assembled P2HMA radical scavenging was restricted to the top ~35 nm of the LbL film, highlighting the effect of the LbL film structure on its antioxidant performance.

*Reproduced with permission from: Hlushko, R.; Ankner, J. A.; Sukhishvili, S. A. Layer-by-Layer Hydrogen-Bonded Antioxidant Films of Linear Synthetic Polyphenols, *Macromolecules* **2020**, 53, 3, 1033–1042 Copyright 2020 American Chemical Society.

3.2. Introduction

Antioxidants can enhance the performance of polymers used in food packaging¹²⁻¹⁵ or biomedical applications^{16,18} by reducing oxidative damage caused by reactive oxygen species. The most common approach of blending low molecular weight antioxidants into a polymer matrix^{1-4,17,18} is often associated, however, with leaching of antioxidants.²⁰ To prevent leaching, antioxidant groups have been introduced into polymeric materials either via covalent modification of already synthesized polymers^{16,21-24} or via direct polymerization of antioxidant-bearing monomers.^{36,37} The latter approach allows for greater control of the distribution of antioxidant species along the polymer chain. Using this approach, antioxidant-bearing materials were used in the preparation of free-standing or substrate-deposited films using solution-casting.⁹²

Here we present an alternative way to generate antioxidant films, based on layer-by-layer assembly of synthetic polymeric antioxidant with of polyphenol rings of varying structure (catechol vs. gallol) and correlate the mechanism of film growth and layering with the antioxidant activity of these assemblies. The LbL deposition technique is a powerful means of creating nanoscopic coatings from a diverse set of components.^{38,39} The most appealing features of the technique are the control it affords of film composition, structure, and thickness and its enabling the application of ultrathin coatings to arbitrarily shaped substrates. The degree to which the LbL technique can provide such control is strongly dependent on the strength of interpolymer binding within the films. While strong polymer-polymer pairing usually results in kinetically trapped conformations of sequentially adsorbed chains and preserves film layering, weak binding enables chain mobility, resulting in polymer intermixing.^{49,52-54} The assembly of LbL films is often supported by electrostatic pairing^{38,39} and/or hydrogen bonding,⁴⁰⁻⁴⁵ with both electrostatically associated and hydrogen bonded films able to be assembled linearly (a constant amount of material

deposited per immersion step) or exponentially (an increasing amount of material deposited per immersion step). Because of the large number of unbound polymer units within exponential films, these assemblies can exhibit high swelling ratios and in extreme cases even approach those characteristic of densely physically crosslinked, surface-attached gels.⁹³ The polymer units which do not directly participate in electrostatic or hydrogen bonding polymer-polymer pairing remain available for supporting film functionality. In the case of electrostatic assemblies, these polymer units have been utilized, for example, for the capture of metal or organic ions.⁹⁴⁻⁹⁶ For hydrogen-bonded LbL assemblies, however, such structure-functionality correlations remain unexplored.

Our group has pioneered the deposition of hydrogen-bonded films composed of a small polyphenol molecule, tannic acid, with neutral polymeric hydrogen-bond acceptors.^{65,97} The low value of the TA ionization constant (pK_a 8.5)⁶⁵ enabled the creation of hydrogen-bonded assemblies stable at neutral to slightly basic pH⁶⁵ and thus the exploitation of the antioxidant, antibacterial, anti-inflammatory, and immuno-modulating properties of TA in biological environments.^{98,99} However, as a small rigid molecule, TA is unable to supply an excess of unbound functional groups within LbL assemblies.

Here, we focus on hydrogen-bonded coatings created by LbL assembly of synthetic linear polyphenols, recently synthesized in our group,^{36,100} containing catechol or gallol functionalities. These polymers, specifically those with gallol functional groups, can be viewed as synthetic analogs of tannic acid. Unlike TA, however, these polymers are flexible and is capable of multisite binding with hydrogen-bonding partners, leaving some segments unbound to polymer partners. We aim to explore how the chemistry of polyphenol moieties affected polymer-polymer binding, chain intermixing and film structure, as well as the availability of polyphenol segments for radical

scavenging. We believe that this work significantly expands the arsenal of adhesive and antioxidant films and coatings which are based on phenolic functionality.^{101,102}

3.3. Experimental section

3.3.1. Materials

Polyethylene oxide with M_n 100 kg/mol, branched polyethylene amine (BPEI) with M_n 60 kg/mol, 2,2'-azino-bis(3-ethylbenzothiazoline-6-sulfonic acid) (ABTS) diammonium salt, ethanol, sodium hydroxide, hydrochloric acid, sodium hydrogen phosphate, and potassium persulfate were purchased from Sigma-Aldrich and used as received. Deuterated poly(ethylene oxide-d4) (*d*PEO) with M_n 93.0 kg/mol and a polydispersity index of 1.07 was purchased from Polymer Source Inc. Linear synthetic polyphenols, poly(3,4-dihydroxybenzyl methacrylamide) (P2HMA, M_n 35.9 kg/mol, PDI 1.20) and poly(3,4,5-trihydroxybenzyl methacrylamide) (P3HMA, M_n 43.4 kg/mol, PDI 1.45), were synthesized and characterized as described in our previous work.³⁶

3.3.2. Film Deposition

Silicon substrates (<111>) used in neutron reflectivity experiments, as well as 0.5-mm thick undoped silicon wafers, both obtained from Institute of Electronic Materials Technology, Poland, were cleaned as described elsewhere.¹⁰³ Prior to film deposition, silicon substrates and/or wafers were primed with a monolayer of BPEI adsorbed from 0.2 mg/mL solution at pH 9 for 20 min. The LbL films were constructed from 0.2 mg/mL polymer solutions in ethanol or water for PPh or PEO, respectively, immersed for 5 minutes per deposition step, rinsed twice in solvent, and dried in a gentle flow of nitrogen gas. The substrates were immersed in the deposition solutions for 5 minutes per deposition step, rinsed twice in solvent, and dried in a gentle flow of nitrogen gas. Films thicker than 20 bilayers were deposited using a Riegler & Kirstein GmbH DR-3 table top dipping robot.

3.3.3. Methods

Spectroscopic Ellipsometry. Refractive indices and thicknesses of LbL films deposited on a silicon wafer were determined using a variable angle spectroscopic ellipsometer (M-2000, J.A. Woollam Co., Inc.) equipped with a temperature-controlled liquid cell. Dry measurements were performed at four incidence angles: 45, 55, 65, and 75°. A single incident angle of 75° was used in liquid-cell measurements due to cell geometry. The thicknesses of the native oxide layers on the silicon wafers were measured prior to depositing the LbL films.

The data for dry LbL films were fitted using a three-layer model. The first two layers were the silicon substrate and the oxide layer. The third layer was characterized as a Cauchy material of thickness d . The wavelength dependence of the refractive index was modeled by $n(\lambda) = A + B/\lambda^2 + C/\lambda^4$, where λ is wavelength and A , B , and C are fitted coefficients.¹⁰⁴ For the swollen films, a four-layer model was used, wherein the solvent was considered as the fourth layer, characterized as a semi-infinite transparent Cauchy medium. The dependence of refractive index on wavelength was determined prior to each measurement using a bare silicon wafer installed in the liquid cell. The four variables A , B , C , and thickness d were fitted simultaneously.

Attenuated Total Reflection Fourier Transform Infrared spectra were collected using a Bruker Tensor II spectrometer equipped with a mercury cadmium telluride detector and an ATR diamond crystal. The spectra were recorded by accumulating 96 scans within a spectral range of 900–4000 cm^{-1} at a resolution of 2 cm^{-1} .

To assess the composition of the polyphenol films, *l*PPh/PEO films of ~200 nm dry thickness deposited on undoped Si wafers were exposed to either *l*PPh or PEO 0.2 mg/mL solutions in ethanol for 5 minutes, followed by two cycles of solvent rinsing, and finally dried in a flow of nitrogen gas. FTIR spectra were collected after each deposited polymer layer.

Atomic Force Microscopy (AFM) studies were performed using a Bruker Dimension Icon AFM instrument in tapping mode using a MikroMasch HQ:NSC35/Cr-Au BS 150 kHz cantilever with a 5.4 N/m force constant. The average film roughness was measured over three imaged areas.

Nanoindentation. Mechanical properties of the films were studied using Hysitron TI 950 Triboindenter equipped with a diamond Berkovich tip with a radius of 150 nm. Indentation was performed in the load-controlled mode, where the load was increased at a constant rate for a 10 s up to a finite value, kept constant for 5 s and brought back to zero in 2 s. The applied load was set as 50 μN for the 0.6 μm films and 150 μN for thicker films. The tip displacement was less than 10% of the total film thickness for all film. The Young's modulus of the films was calculated using the equation

Equation 3-1

$$\frac{1}{E_{eff}} = \frac{1-\nu^2}{E} + \frac{1-\nu_i^2}{E_i}$$

where E_{eff} is the measured effective elastic modulus, E and ν are the Young's modulus and Poisson ratio of the film, E_i and ν_i are Young's modulus and Poisson ratio of the diamond indenter, equal to 1141 GPa and 0.07, respectively.¹⁰⁵ The Poisson ratio of the dry hydrogen-bonded films was set at 0.33, and a value of 0.5 was used for wet measurements, a value which was previously used for LbL films.¹⁰⁶

Neutron reflectometry measurements were performed at the Spallation Neutron Source Liquids Reflectometer (SNS-LR) at the Oak Ridge National Laboratory (ORNL). The reflectivity data were collected using a sequence of 3.4- \AA -wide continuous wavelength bands (selected from $2.55 \text{ \AA} < \lambda < 16.70 \text{ \AA}$) and incident angles (ranging over $0.6^\circ < \theta < 2.34^\circ$). The momentum transfer, $Q = (4\pi \sin \theta/\lambda)$, was varied over a range of $0.008 \text{ \AA}^{-1} < Q < 0.20 \text{ \AA}^{-1}$. Reflectivity curves were

assembled by combining seven different wavelength and angle data sets together, maintaining a constant relative instrumental resolution of $\delta Q/Q = 0.023$ by varying the incident-beam apertures.

Neutron scattering densities within hydrogenated and deuterated blocks were averaged, each block exhibiting its characteristic thickness, scattering density, and interlayer roughness. Those characteristic parameters were adjusted until the reflectivity curve was best fitted (minimized χ^2).

The antioxidant activity of PPh/PEO coatings was studied using a radical scavenging assay employing aqueous solutions of ABTS^{•+} radical cations. The stock solution of ABTS^{•+} was prepared by mixing 10 mL of 7 mM ABTS and 10 mL of 2.45 mM potassium persulfate aqueous solutions. The stock solution was incubated in the dark at ambient temperature for 24 hours to complete the formation of ABTS^{•+} radical cations, and then diluted with water until the absorbance decreased to 1.0-2.0 absorbance units as measured at 732 nm using a 2600 UV-Vis Shimadzu spectrophotometer. The diluted solutions were purged with nitrogen gas for one hour and then immediately used for the antiradical assay. The antiradical efficiency of PPh/PEO films was monitored as a decrease in absorbances of diluted ABTS^{•+} solutions at 732 nm. Experiments were performed with films deposited on 0.5-0.8 cm² Si chips. To perform the radical scavenging assay, the substrates with deposited PPh/PEO films as well as control bare Si wafers were placed in plastic cuvettes filled with 0.04 mM (in case of P3HMA/PEO films) or 0.06 mM (in case of P2HMA/PEO films) ABTS^{•+} solutions and sealed. At a sequence of times after exposure, the solutions were carefully shaken and the absorbance at 732 nm was recorded. The decrease in absorbance was converted to concentration of reacted ABTS^{•+} as $(A_0 - A)/\epsilon$, where A_0 and A are the absorbances of the control ABTS^{•+} solutions and ABTS^{•+} solutions exposed to antioxidant films, respectively, and ϵ is the extinction coefficient of ABTS^{•+} solutions at 732 nm ($\epsilon = 25400$

$M^{-1}cm^{-1}$).¹⁰⁷ Data for the reacted $ABTS^{++}$ were normalized to a 1 cm^2 film area. The antioxidant activity of *l*PPhs in solution was determined similarly from the decrease in the absorbance of 3.0 mL 0.075 mM $ABTS^{++}$ aqueous solution after addition of 100 μ L of 0.5 mg/mL polymer in ethanol.

3.4. Results and discussion

Figure 3-1A shows the chemical structures of the two synthetic linear polyphenols used in this work. These polymers, poly(3,4-dihydroxybenzyl methacrylamide) and poly(3,4,5-trihydroxybenzyl methacrylamide), containing catechol and gallol pendant groups, respectively, were previously synthesized by our group using RAFT polymerization.³⁶ P2HMA and P3HMA had number-average molecular weights of 35.9 kg/mol and 43.4 kg/mol, and degrees of polymerization of 170 and 200, respectively (Figure 3-1A). In previous work we showed that the structure of the polyphenol rings had a weak effect on intrinsic *l*PPh antioxidant activity but strongly affected the capability of these polymers to adsorb within a monolayer on a solid substrate. Specifically, P3HMA, containing gallol-like pendant groups, had a higher propensity than P2HMA to adsorb to surfaces.³⁶ This work aims to explore the capability of *l*PPhs of different chemical structure to assemble at surfaces within multilayers rather than monolayers. To that end, *l*PPh polymers have been assembled within functional LbL coatings with polyethylene oxide, which is used as a hydrogen-bonding partner.

Figure 3-1B shows the increase in dry film thickness during LbL film deposition measured by ellipsometry. Assembly occurs as a result of hydrogen bonding between hydroxyl groups in polyphenol units and PEO units. Films formed by PEO and *l*PPh with catechol functionality (P2HMA) grew linearly, with a 3.3-nm dry thickness increase per bilayer. In contrast, the P3HMA/PEO layers exhibited a dramatically different growth mode, forming much thicker films of exponentially

increasing thickness per deposition step. The exponential growth of P3HMA/PEO films was somewhat counterintuitive since such growth is usually a characteristic of weakly associated polymers.^{108,109} As a polyphenol with three hydroxyl groups, P3HMA is a stronger hydrogen donor than P2HMA³⁶ and thus was expected to bind more strongly with PEO and to exhibit linear film growth. Figure 3-1B displays the opposite trend, however, with linear growth for the P2HMA/PEO rather than the P3HMA/PEO system. This trend can be explained if one suggests that gallol units are more prone to self-association compared to the catechol functionalities in P2HMA, resulting in a large polymer mass deposited at surfaces within P3HMA loops. Stronger hydrogen bonding between gallol moieties as compared to catechols has previously manifested itself in higher stability of gallol-containing supramolecular structures.¹¹⁰ The stronger hydrogen donating capability of gallols is also supported by their higher acidity (pK_a of 9.01 and 9.45 for gallol and catechol groups, respectively).¹¹¹ Stronger hydrogen bonding between P3HMA units can reduce the total number of units in P3HMA chains available for binding with PEO and weaken the overall P3HMA/PEO polymer-polymer association. The difference in mass balance between PPh and PEO within hydrogen-bonded films was clearly observed in ellipsometric measurements of dry thickness during film growth. Estimates made for films thicker than four bilayers (to reduce the effect of the substrate) and using 1 g/cm³ for film density, gave molar ratios of phenolic –OH groups to ether –C–O–C– groups of PEO deposited within LbL films as 1.7±0.2 and 0.8±0.2 for P3HMA/PEO and P2HMA/PEO, respectively, indicating a significant excess of P3HMA.

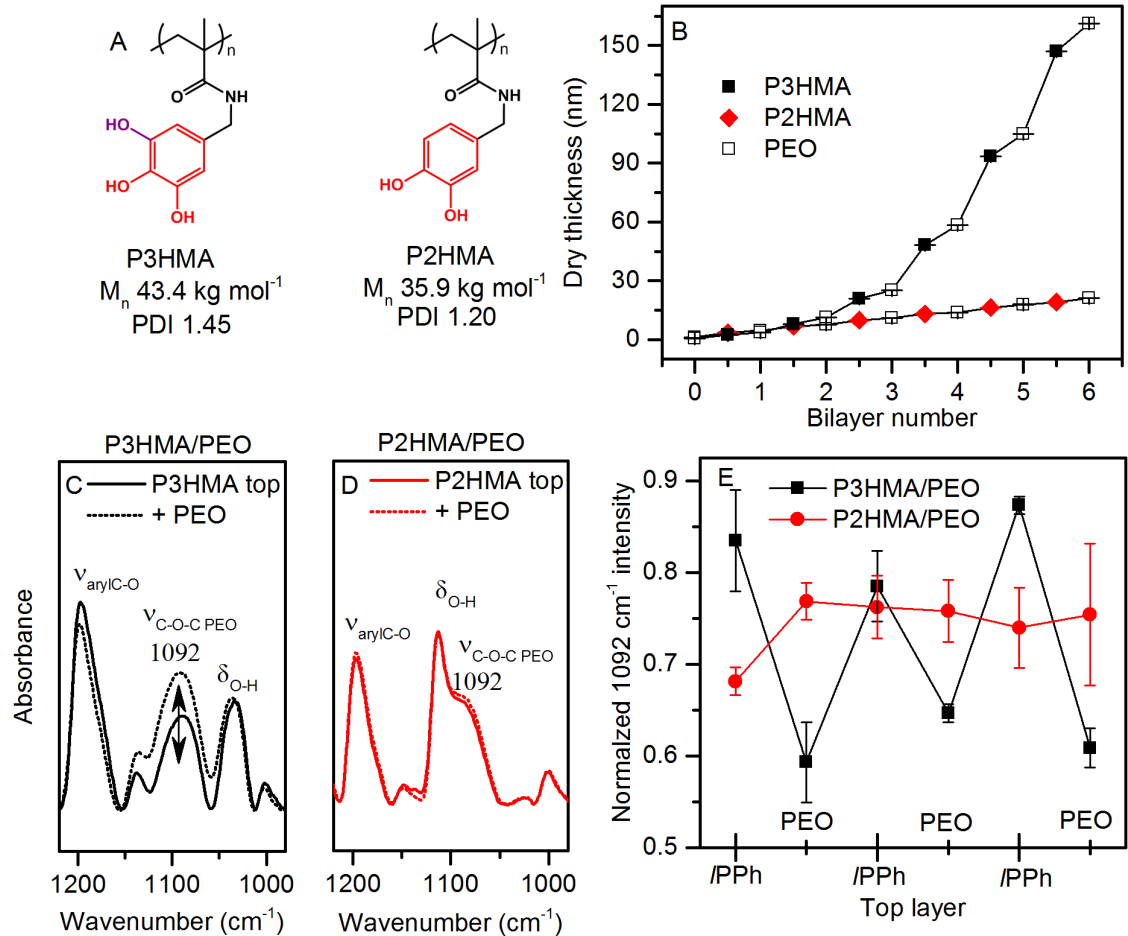


Figure 3-1 Chemical structures and molecular characteristics of /PPhs (A); the dry thickness of /PPh/PEO films monitored by ellipsometry during film deposition (B); and changes in FTIR spectra of 6.5-bilayer P3HMA/PEO (C) or 50.5-bilayer P2HMA/PEO (D) films (with /PPh as a top layer in both cases) of matched thickness of ~200 nm in the 1250-950 cm⁻¹ region upon addition of consecutive layers (E). See Figures B-1, B-2 for the entire FTIR spectra.

The composition of /PPh/PEO films was further explored using ATR-FTIR spectroscopy.

Figure B-1 shows the FTIR spectra of individual film components and /PPh/PEO films. The formation of hydrogen bonds between /PPh and PEO was observed spectroscopically by changes in a broad O-H band stretching region of /PPh, with a red shift in the band maximum from 3358 cm⁻¹ to 3355 cm⁻¹ and a significant ~50-120 cm⁻¹ narrowing from the high-wavenumber side of the band (Figure B-2).

Significant changes were also observed for the *l*PPh/PEO films in the 1200-1000 cm⁻¹ region, especially in the relative intensity of an ~1190 cm⁻¹ band associated with aryl -C–O stretching vibrations coupling with the skeletal vibrations of the benzene ring.¹¹² Changes in the vibrational intensities of covalent bonds involved in hydrogen bonding have been predicted theoretically and observed experimentally for several small organic molecules.^{113,114} Figure 3-1E shows the variation of the integrated intensity of the 1092 cm⁻¹ C–O–C stretching vibrational band of PEO during deposition of additional layers to ~200-nm-thick P3HMA/PEO and P2HMA/PEO films. To allow for a quantitative comparison of changes in the relative amounts of PEO and *l*PPhs during film growth, the raw ATR-FTIR data were normalized to the intensities at 1605 cm⁻¹ and 1609 cm⁻¹, which are associated with skeletal ring vibrations of catechol and gallol pendant groups in assembled P2HMA- and P3HMA-containing films, respectively. The changes in the intensity of the 1092 cm⁻¹ band upon deposition of additional layers were drastically different for P3HMA/PEO and P2HMA/PEO films. For exponentially growing P3HMA/PEO films, significant oscillations in intensity at 1092 cm⁻¹ occurred for successive layers, indicating the deposition of a large amount of polymer and a significant shift in the ratio of film components with each layer deposition step. In contrast, in the P2HMA/PEO system the 1092 cm⁻¹ intensity was almost unaffected by the addition of successive layers. Such behavior is expected for this linearly growing film, in which polymer adsorption was limited to the film surface and relatively little material was added (~3 nm per bilayer) to the existing thick (~200 nm) film.

Differences in the internal structure of P3HMA/PEO and P2HMA/PEO films were then explored by neutron reflectometry, a technique we have previously applied to study the structure of electrostatically assembled and hydrogen-bonded LbL films.^{49,115-117} To introduce contrast in neutron reflectometry measurements, fully deuterated PEO, *d*PEO, with M_n of 101.7 kg/mol

matching the molecular weight of hydrogenated PEO of ~ 100 kg/mol, was used to create marker layers. Figure 3-2A depicts the design of the films used in the neutron reflectometry experiments. The films had a sandwich-like architecture featuring deuterated stacks deposited at the film substrate and surface with a hydrogenated stack in the middle. The dry thicknesses of the stacks were measured with ellipsometry during film construction (see Tables B-1, B-2) and used for initial construction of the models used to fit the neutron reflectivity data. Note that while only one *d*PEO layer was needed to provide scattering contrast in the P3HMA/PEO film, two bilayers were needed to accumulate enough material for P2HMA/PEO, due to the small incremental mass increase for each layer deposited.

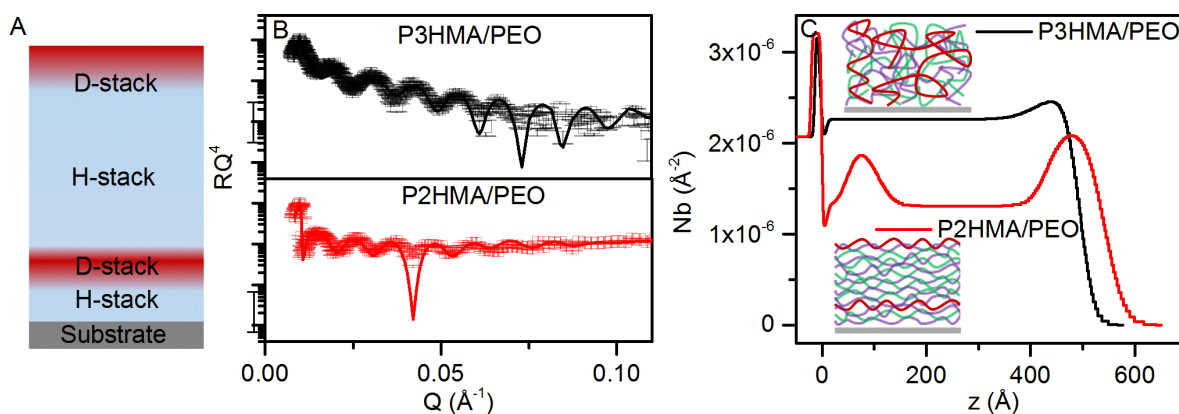


Figure 3-2 Schematic of the film design, where H-stacks are built of hydrogenated PEO and *I*PPh, and D-stacks are built of deuterated PEO and *I*PPh (A); neutron reflectivity plotted as RQ^4 to highlight structural details for $(\text{P3HMA/PEO})_2/\text{P3HMA}/d\text{PEO}/\text{P3HMA/PEO}/\text{P3HMA}/d\text{PEO}$ and $(\text{P2HMA/PEO})_2/(\text{P2HMA}/d\text{PEO})_2/(\text{P2HMA/PEO})_7/(\text{P2HMA}/d\text{PEO})_2$ films (B), and the fitted neutron scattering density profiles of those films (C).

Figures 3-2B&C show the neutron reflectivity data and fitted neutron scattering length density (SLD) profiles for linear and exponential films. The scattering length density (SLD, Nb), the thickness of hydrogenated and deuterated stacks d , and internal roughness σ_{int} were found by fitting the reflectivity data and are shown in Tables B-3 and B-4 for P3HMA/PEO and P2HMA/PEO films, respectively. For the linear P2HMA/PEO film, distinct regions of higher and

lower SLD were observed, associated with the deuterated and hydrogenated stacks of the deposited polymers. The boundaries between the H- and D-stacks were diffuse, with interfacial widths of 5.8 nm and 6.2 nm for the substrate- and surface-deposited deuterated blocks. In contrast, the P3HMA/PEO exponential film was highly intermixed with nearly all differences in SLD between hydrogenated and deuterated layers smeared out by molecular diffusion. Marker *d*PEO permeated the entire ~50-nm thickness of the P3HMA/PEO film within 5 min, while for the P2HMA/PEO film, *d*PEO only diffused to a depth of half the interfacial roughness of the deuterated stack within the hydrogenated matrix. The diffusion coefficients of *d*PEO were therefore estimated as $\sim 10^{-14}$ and $\sim 10^{-16}$ cm²/s for P3HMA/PEO and P2HMA/PEO, respectively. For the P3HMA/PEO film, the estimated diffusion coefficient of $\sim 10^{-14}$ cm²/s represents a lower bound and is of the same order of magnitude as the diffusion coefficients of polyelectrolytes reported for highly intermixed non-linearly growing electrostatically assembled LbL films.⁴⁹

Figure 3-3 shows clear differences in the surface morphology and roughness of P3HMA/PEO and P2HMA/PEO films. The AFM root-mean-square roughnesses of these films were 5.8 ± 2.5 nm and 2.9 ± 0.7 nm, respectively, indicating a smoother surface on the P2HMA/PEO film. High surface roughness was previously reported for electrostatically assembled exponential films and explained by microphase separation at the film surface, enhanced by salt-induced disruption of polymer-polymer pairing.¹¹⁸

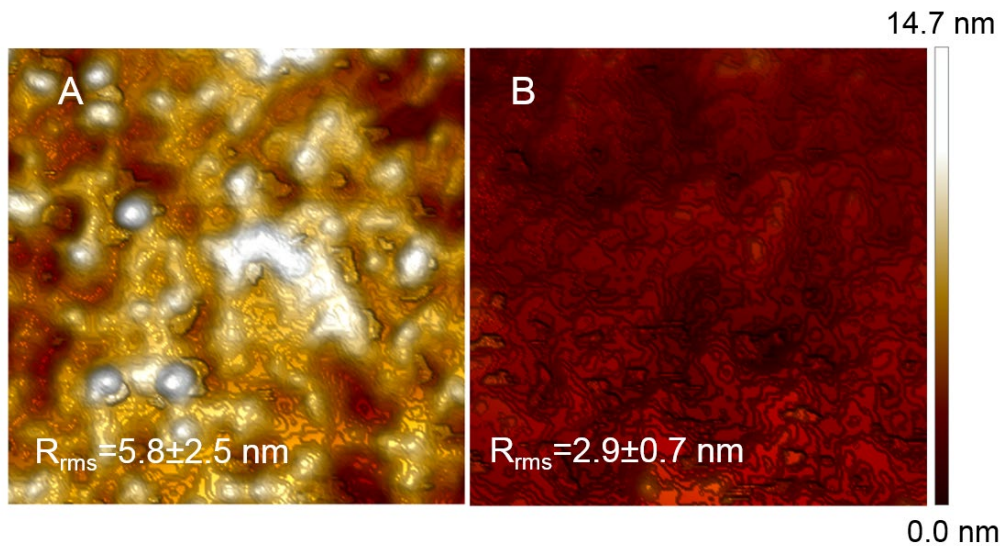


Figure 3-3 AFM topography image of a 6.5-bilayer P3HMA/PEO film (A) and a 50.5-bilayer P2HMA/PEO film (B) of a matched thickness of ~ 200 nm. The scan area size is 600×600 nm² and the z -scale shown on the right applies to both images.

We next address how the different morphology and internal structure of *l*PPh/PEO films affect film functionality, *i.e.* its antioxidant activity. Confining *l*PPh moieties within assembled films can influence their antioxidant performance. Film swelling and the strength of polymer-polymer pairing are both expected to influence the availability of assembled *l*PPh units for interaction with radical species. Prior to the antioxidant studies, the stability of the films was examined. Figure B-3 shows that *l*PPh/PEO films dissolved only when pH was raised significantly higher than the pK_a of the polyphenol moieties (9.01 and 9.45 for catechol and gallol groups)¹¹¹, causing ionization of hydroxyl groups in the polyphenol rings. The films were therefore stable over a wide range of pH, including the pH 6.0 at which the ABTS assay was performed.

In the ABTS assay, the number of radicals consumed over time was quantified spectroscopically by measuring the UV-Vis absorbance of ABTS^{•+} solutions at 732 nm. Quenching of colored ABTS^{•+} radicals can easily be detected visually by the bleaching of the blue-green solution. To compare the scavenging rates of ABTS^{•+} radicals by antioxidant polymers in solution

to those in the film, the number of /PPh antioxidant monomers in solution was matched to those assembled within /PPh/PEO films, assuming dry polymer densities of 1 g/cm³.

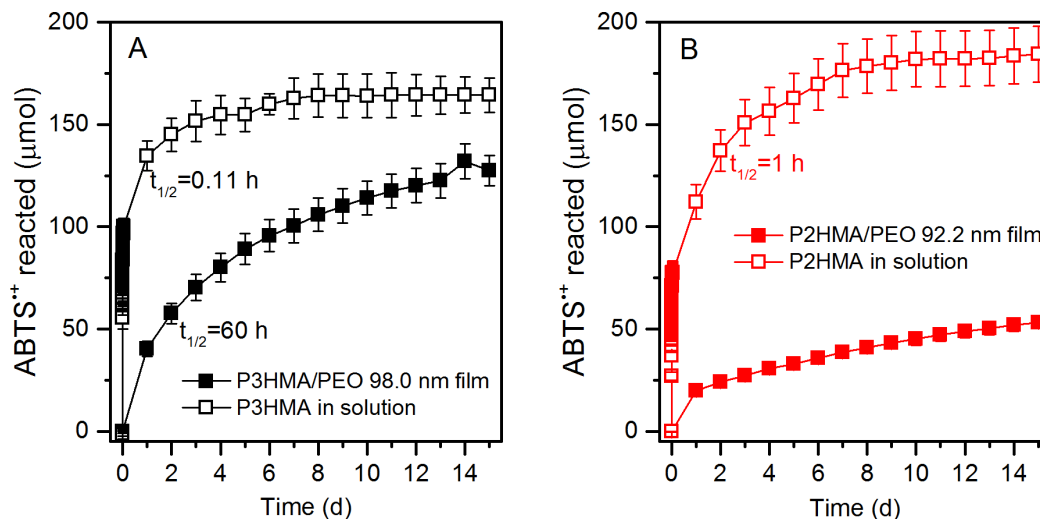


Figure 3-4 Comparison of kinetics of ABTS^{•+} scavenging by matched quantities of /PPh antioxidant polymer dissolved in solution or assembled within a 98-nm (4.5-bilayer) P3HMA/PEO film (A) or a 92.2-nm (25.5-bilayer) P2HMA/PEO film (B). Both films had /PPh as a top layer.

Figure 3-4 shows ABTS^{•+} scavenging is dramatically reduced relative to polymers in solution when the antioxidant polymers are assembled within films. Note that, commonly, ABTS^{•+} assays with antioxidant species in solution are performed over minutes-to-hour time scales.¹¹⁹⁻¹²² Here, we were interested in the long-term performance of antioxidant polymers assembled within LbL films, and therefore special care was taken to reduce the long-term degradation of stable radicals by initially purging nitrogen through the stable radical solution, followed by sealing and keeping all solutions in the dark (see Experimental sections for more details). Figure B-4 shows that despite these precautions, ~20% of the initial ABTS^{•+} degraded in control solutions after 15 days, and that the percentage of degraded ABTS^{•+} was not affected by the presence of PEO in solution. All data presented in this manuscript were corrected by subtracting the degraded quantity of ABTS^{•+} found in the control experiment.

Figure 3-4 also reveals significant differences in solution vs. film behavior for *l*PPh with catechol and gallol functionalities. In solution, the half-life of ABTS^{•+} consumption was shorter for P3HMA than P2HMA (0.11 hour vs 1 hour), in agreement with the previously reported higher reactivity of low-molecular-weight polyphenols featuring more phenolic groups.¹²³ For *l*PPhs assembled within films, the radical scavenging rate was strongly reduced. In the case of P3HMA/PEO films, the half-life of ABTS^{•+} consumption (~60 h) was more than two orders of magnitude longer than that for P3HMA in solution (0.11 h, Figure 3-4A). For P2HMA/PEO films, the reaction rate decreased so much that half-conversion of ABTS^{•+} was not achieved for a 92.2-nm film even after 15 days, reaching only 30% of the polymer activity in solution (Figure 3-4B). These results suggest that the impact of diffusional constraints to penetration of ABTS^{•+} into P2HMA/PEO films was more significant than that into P3HMA/PEO films.

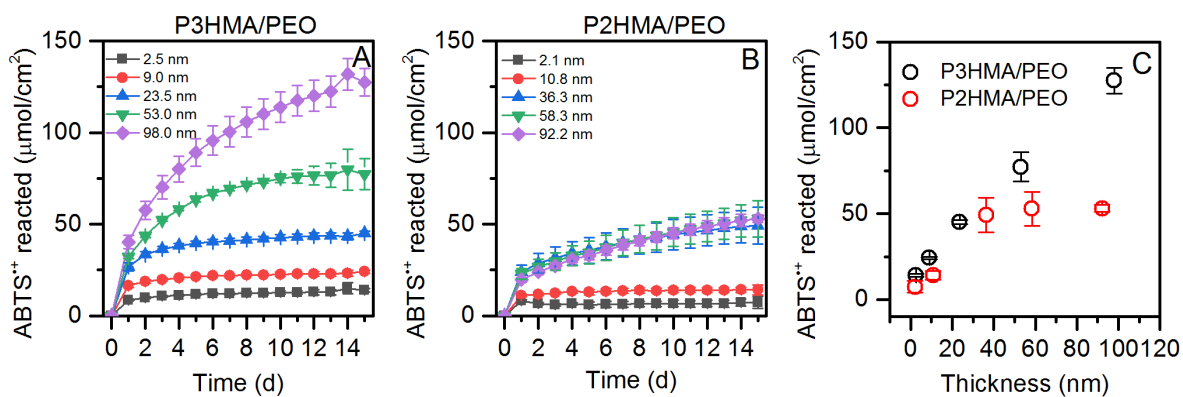


Figure 3-5 Time evolution of ABTS^{•+} quantity reacted with P3HMA/PEO (A) and P2HMA/PEO (B) films of different thicknesses, as well as antioxidant activity of *l*PPH/PEO films assessed from the limiting values of ABTS^{•+} reduced after 15 days (C).

To further assess differences in the radical scavenging capability of *l*PPH/PEO films, we designed experiments involving films of different thicknesses. Figure 3-5A–C shows that the kinetic profiles of ABTS^{•+} reduction vary differently with thickness for P3HMA/PEO and

P2HMA/PEO films. While the amount of consumed ABTS^{*+} increased linearly with film thickness for P3HMA/PEO films, it saturated for films thicker than ~ 35 nm for P2HMA/PEO. Figure 3-5C compares the limiting amounts of ABTS^{*+} reacted after 15 days. Together, these data suggest a differing availability of assembled I^{PPh} s for radical scavenging. In the case of P3HMA/PEO, the entire thickness of the films reacts with ABTS^{*+} , while only the top layers of the P2HMA/PEO films were available for reaction. The thickness of P2HMA/PEO contributing to radical scavenging can be estimated from Figure 3-5B as 30-35 nm. Differences in the penetration of ABTS^{*+} into I^{PPh} /PEO films are illustrated in Figure 3-6.

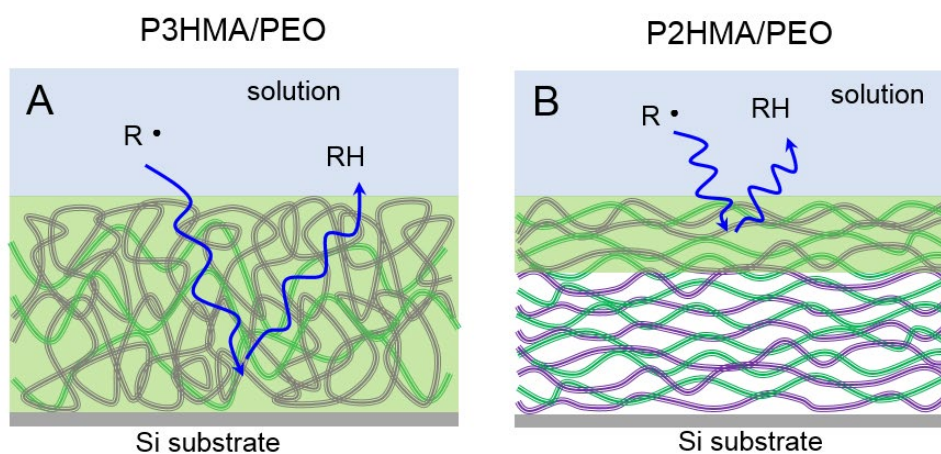


Figure 3-6 Schematic representation of ABTS^{*+} radical penetration into the bulk of the exponential P3HMA/PEO film (A), and the linear P2HMA/PEO film (B). The green area depicts the antioxidant active region.

Spectroscopic ellipsometry data on I^{PPh} /PEO film swelling at pH 6, *i.e.* under the same conditions used in the ABTS assay, provide additional insight into the structural determinants of free radical penetration. The data in Figure 3-7A show that while P3HMA/PEO films took up $\sim 30\%$ water (assuming a polymer density of 1 g/cm^3), P2HMA/PEO films were practically unswollen.

The effect of uptake of water on film mechanical properties was explored using nanoindentation. These studies were performed on *l*PPh/PEO films whose thickness exceeded 0.5 μm , with tip penetration limited to 60 nm to eliminate the effect of silicon substrate. Figure 3-7B shows that the Young's moduli for dry *l*PPh/PEO films were in the 9 to 12 GPa range. However, P3HMA/PEO and P2HMA/PEO films responded very differently upon exposure to water.

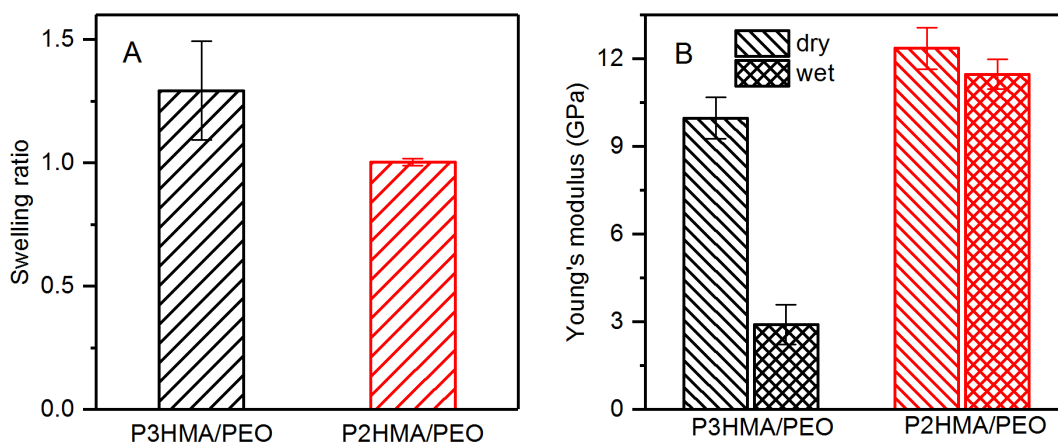


Figure 3-7 The swelling ratios of a 4.5-bilayer, 98-nm P3HMA/PEO film and a 25.5-bilayer, 92.2-nm P2HMA/PEO film as measured by *in situ* ellipsometry (A) and Young's moduli of 0.6- μm -thick *l*PPh/PEO films dry and wet state (B).

While the P3HMA/PEO system underwent substantial plasticization, the Young's modulus did not significantly change for the P2HMA/PEO films. The threefold solvent-induced decrease in the Young's modulus of P3HMA/PEO films is smaller than values reported for ionically associated polyelectrolyte multilayers,^{106,124} probably due to the low propensity of assembled *l*PPh chains to hydrate upon exposure to water. In spite of the insolubility of P3HMA in water, loose association between P3HMA and PEO allowed for significant water uptake within the film. This higher degree of swelling contributes to the higher antiradical activity of P3HMA/PEO films by providing a larger free volume, easing the penetration of radicals into the bulk of the film. In

contrast, tighter interlayer binding within P2HMA/PEO films suppressed water uptake, leading to limited penetration of ABTS^{•+}.

Reaction of ABTS^{•+} with phenolic compounds, whose redox potentials are typically lower than that of ABTS^{•+} (~0.7 V), has been suggested to occur predominantly via a single electron transfer (SET) mechanism.^{119,125} In the case of catechol and gallol functionalities, several reaction products have been proposed, with quinones most often formed from catechols, and oxidative crosslinking proposed as a typical reaction path.¹²⁶ A question then arises of how reaction with ABTS^{•+} alters the properties of the assembled films. To determine if crosslinking takes place in these LbL films, the stability of films in a competitive hydrogen-bonding solvent was assessed for pristine as-deposited films and for films exposed to ABTS^{•+}. Figure 3-8A illustrates the effect of ABTS^{•+} on film stability. It has been observed that *l*PPh/PEO films dissociate to individual polymer components when the concentration of DMF – a stronger hydrogen bond acceptor than PEO^{127,128} – is above 20-30 vol %. A hydrogen-bond-accepting solvent, such as DMF or DMSO, was previously reported to competitively bind with polymers containing hydrogen-bond-donating units, such as carboxylic groups in polyacids, resulting in a weakening in binding or a dissociation of hydrogen-polymer complexes^{129,130} or hydrogen-bonded LbL films.^{26,131} In this work, DMF formed hydrogen bonds with polyphenol groups of assembled *l*PPh, and dissolved P3HMA/PEO and P2HMA/PEO films when DMF content exceeded 20 and 30 vol %, respectively. The higher stability of P2HMA/PEO assemblies in DMF solutions is consistent with a larger number of hydrogen bonds with PEO per P2HMA moiety in this linearly growing system. Remarkably, exposure to ABTS^{•+} resulted in a drastic increase in the stability of the films, which did not dissolve in DMF up to 70 vol % (Figure 3-8A), but delaminated from the surface at higher DMF concentrations.

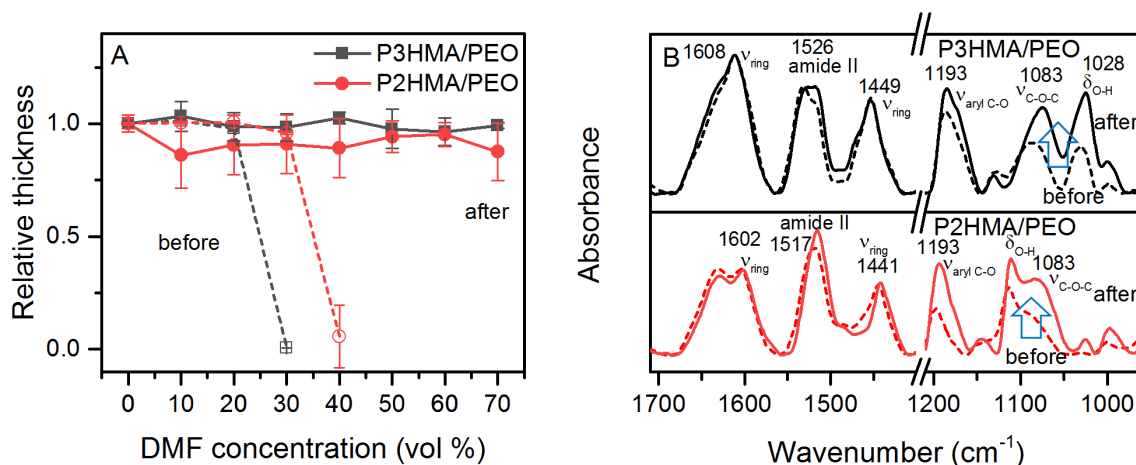


Figure 3-8 Stability of 6.5-bilayer P3HMA/PEO and 50.5-bilayer P2HMA/PEO films with a matched thickness of ~200 nm in the DMF/water mixed solution before (dotted line) and after (solid line) exposure to 0.075 mM solutions of ABTS⁺ for 15 days (A), as well ATR-FTIR spectra of the films before and after a 5-day assay (B).

To identify chemical changes in the /PPh/PEO film triggered by the reaction of /PPh with ABTS⁺, FTIR measurements were performed before and after long-term exposure to solutions of the radical species. FTIR spectra shown in Figure 3-8B indicate a significant increase in absorbance of /PPh/PEO films in the 1000-1200 cm⁻¹ region after exposure to ABTS⁺ solutions. Increased intensities of a band at 1193 cm⁻¹, which is associated with aryl -C-O stretching vibrations coupled with skeletal vibrations of the benzene ring, as well as of a band at 1083 cm⁻¹, which is assigned to -C-O-C- stretching vibrations,^{112,132} are both consistent with the formation of ether bonds as a result of radical-induced coupling of polyphenol rings (Figures B-10 and B-11).

In conclusion, we have found fundamental differences in LbL assembly of synthetic linear polyphenols with gallol- and catechol pendant groups and demonstrated the dramatic effect of these differences on film functionality. Specifically, the film growth mode, structure, and antioxidant activity were all strongly influenced by the chemical structure of the polyphenol rings.

A gallol-based polymer resulted in exponential film growth, in which polymer chains were strongly intermixed. Weak intermolecular binding within those films led to film swelling and engagement of polyphenol units throughout the entire film thickness in radical scavenging reactions. In contrast, a catechol-based polyphenol formed linearly grown films that restricted the penetration of radical species, thus confining radical scavenging to the surface layers of the films. This work demonstrates how the chemical structure of polyphenol units can control their hydrogen bonding within LbL films and can program film structure, swelling, and availability of polyphenol units for interaction with radical species.

4. DYNAMICS AND SELF-HEALING OF LAYER-BY-LAYER HYDROGEN-BONDED FILMS OF LINEAR SYNTHETIC POLYPHENOLS*

4.1. Abstract

This work explores dynamics of hydrogen-bonded layer-by-layer films of linear synthetic polyphenols with varied backbone and pendant group structure. The polymers had the repeat units with catechol-like or gallol-like polyphenol rings, *i.e.* poly(3,4-dihydroxybenzyl methacrylamide), poly(3,4-dihydroxybenzyl acrylamide) (P2HAA), poly(3,4,5-trihydroxybenzyl acrylamide) (P3HAA) and poly(3,4,5-trihydroxybenzyl methacrylamide), and were assembled with linear poly(ethylene oxide). Structure of *l*PPhs had a major effect on diffusivity of LbL films, and chain dynamics was asymmetric for *l*PPh- and PEO-terminated films during film construction. Specifically, diffusivity of polyphenols in the direction perpendicular to the substrate varied from values below $\sim 10^{-18}$ cm² s⁻¹ to $\sim 10^{-14}$ cm² s⁻¹ for *l*PPhs of P2 and P3 families as assessed by *in situ* ellipsometry during film assembly. Similarly, large differences in film dynamics were revealed by neutral reflectometry, which detected fast penetration of deuterated PEO through the entire film with the diffusion coefficient $> 10^{-12}$ cm² s⁻¹ through P3HMA/PEO films, but accumulation of *d*PEO at the film surface for all other *l*PPh/PEO systems during the first 10 minutes of the experiment. The found trends in film dynamics were consistent with strongly exponential growth of P3HMA/PEO films, and largely linear deposition of non-diffusive P2/PEO systems. Finally, self-healing behavior of *l*PPh/PEO films in aqueous environment was quantified by *in situ* AFM experiments, which revealed robust self-healing of P3/PEO films occurring at the time scale of minutes, and absence of film healing in the case of P2/PEO films.

*Reproduced in part with permission from *Macromolecules*, submitted for publication. Unpublished work copyright 2021 American Chemical Society.

4.2. Introduction

Layer-by-layer deposition of polymers at surfaces has become a powerful tool for assembly of functional coatings for a variety of applications.¹³³ For example, LbL coatings can be created to enhance tissue regeneration,^{134,135} provide hemocompatibility, antibacterial and antioxidant activity to biomedical devices,¹³⁵ or control localized delivery of bioactive molecules.^{51,136,137} Among various intermolecular forces that control LbL assembly, such as electrostatic,^{38,39} metal-ligand coordination¹³⁸ or hydrophobic interactions,⁴⁶ hydrogen bonding is unique in its ability to assemble neutral molecules and include antioxidant polyphenol molecules within surface coatings.^{40-42,139-141} While earlier hydrogen-bonded films were mostly based on assembly of poly(carboxylic acids) which assembled with neutral polybases at acidic pH and dissociated in neutral and basic environments,^{40,41,45,142,143} more recent studies focused on assembly of a neutral polyphenol molecule – tannic acid, which yielded robust films stable in a wide range conditions, including physiological ones.⁶⁵ Inclusion of polyphenols within LbL films opens a way for combining a generally known for hydrogen-bonded systems nontoxicity with polyphenol-provided antioxidant and radical scavenging activity of the coatings. These advantages of TA-based assemblies were advantageously used for encapsulation of living cells^{144,145} and construction of nontoxic capsules that can modulate immune response.¹⁴⁶⁻¹⁴⁸

Fundamental principles of hydrogen-bonded LbL assemblies and their structure-property relations are less understood, however, compared to those of their electrostatically assembled counterparts. For electrostatically assembled LbL films, it is well established that film structure and polymer chain diffusivity are dependent on the strength of interpolymer ionic pairing,^{51,149-151} polymer molecular weight,^{115,152} chains rigidity,¹⁵³ and how they can be controlled by the film processing conditions, such as solution pH,¹⁵⁴ salt concentration,¹¹⁶ temperature,¹⁵⁵ or assembly

time.¹⁵⁶ For hydrogen-bonded films, few correlations between strength of hydrogen-bonding and film growth regime (linear *vs.* exponential) have also been established. For example, strongly bound polyvinylpyrrolidone/poly(methacrylic acid) films deposited linearly,⁴⁸ while weakly associated poly(ethylene oxide)/PMAA films exhibited exponential growth.¹⁵⁷ The growth regimes were correlated with the degree of polymer chain intermixing within hydrogen-bonded films as determined in neutron reflectometry (NR) experiments.¹⁵⁸ Unlike electrostatic systems, hydrogen-bonded assemblies typically do not involve charge pairing, and film deposition does not need to follow the rule of balance of charges within the films, osmotic effects associated with counterions or long-range repulsions that terminate deposition of polyelectrolyte chains. Instead, polymer chains are deposited through saturation of hydrogen-bonded sites within the film. Distinct from ionic pairing, hydrogen-bonding sites are only weakly sensitive to salt concentration.¹⁴³ Instead, the strength of hydrogen bonding can be modulated by an addition of small molecules which play a role of hydrogen bonding competitors.⁴⁸ Similar to salt ions in electrostatic LbL films, such competitors weaken polymer-polymer interactions and can strongly affect film growth mode or even destruct LbL assemblies.⁴⁸

It is usually assumed that hydrogen-bonding interactions are weaker than electrostatic coupling and lead to reversible, dynamic assemblies.^{159,160} However, hydrogen bonding is strengthened by hydrophobic interactions in aqueous media,¹⁶¹ and a wide range of layer interdiffusion is found in hydrogen bonded LbL films.^{158,162} In electrostatic polyelectrolyte assemblies, chain dynamics was explored by a variety of techniques. One of them, a wide-line ²H NMR spectroscopy, revealed dependence of chain mobility on the nature of the capping layer¹⁶³. Numerous studies of lateral diffusivity of polymer chains were also performed for different electrostatically assembled LbL films using fluorescence recovery after photobleaching

(FRAP)^{45,116,153,162}. At the same time, salt-triggered layer intermixing and chain diffusion in the direction perpendicular to substrate was explored using neutron reflectometry,^{116,164-166} revealing anisotropy of chain dynamics in salt solutions of linearly growing polyelectrolyte multilayers.¹⁶⁷ Another technique to assess dynamics of polymer assemblies is based on monitoring evolution of surface morphology by atomic force microscopy.^{168,169} Smoothing of the surface morphology of electrostatically assembled films was observed due to diffusivity of polyelectrolytes from the “peaks” to “valleys” during films annealing in salt solution, and surface (inter)diffusion coefficients of 10^{-15} – 10^{-14} cm² s⁻¹ were estimated for these systems.¹⁶⁸ However, these studies were not previously applied to hydrogen bonded films. Studies of dynamics in hydrogen-bonded systems so far have been limited to the application of wide-line ²H NMR spectroscopy to films of weak poly(carboxylic acids) with neutral polymer acceptors, such as PVP and PEO.¹⁷⁰

In this work, we use a combination of *in situ* ellipsometry, NR and AFM techniques to explore dynamics of polymer chains and self-healing in hydrogen-bonded assemblies. These studies are performed with linear synthetic polyphenol polymers rather than with previously studied films of poly(carboxylic acids). A family of synthetic polyphenols with two or three polyphenol groups in the benzene ring has been previously synthesized in our groups and were shown to exhibit antioxidant properties.^{36,100} We previously demonstrated that the structure of the polyphenol rings has a strong effect on the film growth regime, film internal structure and the ability of these assemblies to radical scavenging.¹⁷¹ In this work, we aim to understand the underlying dynamics that controls such films behavior. Using a NR to track invasion of deuterated PEO chains within linear and exponential hydrogen-bonded LbL, *in situ* ellipsometry to monitor kinetics of mass deposition during film construction, and AFM to track healing of tip-indented films upon exposure to water, we uncover the differences in chain diffusivity between film

components during film construction, and correlate them with film growth mode and structure of the polyphenol ring of hydrogen-bonded linear polymers.

4.3. Experimental section

4.3.1. Materials

Branched polyethylene amine with number-average molecular weight (M_n) of 60,000 g/mol, ethanol, sodium hydroxide, hydrochloric acid, sodium hydrogen phosphate, and potassium persulfate were purchased from Sigma-Aldrich and used as received. Polyethylene oxide with M_n 95,000 g/mol, polydispersity index (PDI) of 1.08, and deuterated poly(ethylene oxide-*d*4) with M_n 93,000 g/mol and PDI 1.07 were purchased from Polymer Source, Inc. Linear synthetic polyphenols with two and three hydroxyl groups in the benzene ring and methacrylamide or acrylamide backbones were synthesized using reversible addition–fragmentation chain transfer polymerization. Polymers with methacrylamide backbone, *i.e.* poly(3,4-dihydroxybenzyl methacrylamide) (P2HMA, M_n 35,900 g/mol, PDI 1.20) and poly(3,4,5-trihydroxybenzyl methacrylamide) (P3HMA, M_n 43,400 g/mol, PDI 1.45), were prepared as described in our previous publication.³⁶ At the same time, synthesis and characterization of acrylamide-backbone polymers, *i.e.* poly(3,4-dihydroxybenzyl acrylamide) (P2HAA, M_n 36,400 g/mol, PDI 1.17) and poly(3,4,5-trihydroxybenzyl acrylamide) (P3HAA, M_n 42,300 g/mol, PDI 1.20), was performed in this work for the first time and is schematically shown in Figure C-1 and described in the Appendix C.

4.3.2. Film Deposition

Silicon wafers used for ellipsometric studies of film deposition (0.5-mm-thick, undoped) used for characterization of LbL films by ellipsometry and silicon substrates (<111>, 50 mm-diameter, 4.0 mm-thick) used for neutron reflectometry studies of polymer chain diffusion were

both obtained from the Institute of Electronic Materials Technology, Poland. Prior to LbL film deposition, the substrates were cleaned by UV radiation and concentrated sulfuric acid and primed with a monolayer of BPEI, which was adsorbed from a 0.2 mg/mL solution at pH 9 for 20 min as described in our previous publication.¹⁰³ Construction of *l*PPh/PEO films was then performed (starting from deposition of *l*PPh) using a sequential exposure of the substrates in 0.2 mg/mL solutions of *l*PPh and PEO in ethanol or water, respectively, and application of two rinsing cycles in between the polymer deposition steps. The rinsing steps after deposition of *l*PPh were performed in ethanol first and then in ethanol/water (1:1 by volume) mixture, while PEO-capped films were first rinsed with water first and then with a 1:1 v/v ethanol/water mixture. For studies of film growth modes by ellipsometry and neutron reflectometry, deposition was performed manually using 5-min immersion time in each polymer solution, followed by carefully drying of films in a gentle flow of nitrogen gas after each deposition cycle prior to analysis.

For studies of healing in aqueous environment using *in situ* AFM, *l*PPh/PEO films with ~400-nm dry thickness were deposited using a Riegler & Kirstein GmbH DR-3 table-top robotic system at a 0.5 cm/s deeping and withdrawal rate.

4.3.3. Methods

Spectroscopic Ellipsometry. Thicknesses of LbL films deposited on a silicon wafer were determined using a variable angle spectroscopic ellipsometer (M-2000, J.A. Woollam Co., Inc.) equipped with a temperature-controlled liquid cell. Dry measurements were performed at four incidence angles: 45, 55, 65, and 75°. A single incident angle of 75° was used in liquid-cell measurements due to cell geometry. The thicknesses of the native oxide layers on the silicon wafers was measured prior to depositing the LbL films. The data for dry LbL films were fitted using a three-layer model. The first two layers were the silicon substrate and the oxide layer. The third

layer was characterized as a Cauchy material of thickness d . The wavelength dependence of the refractive index was modeled by $n(\lambda) = A + B/\lambda^2 + C/\lambda^4$, where λ is wavelength and A , B , and C are fitted coefficients.¹⁰⁴

For studies of polymer chain uptake using *in-situ* ellipsometry, *l*PPh/PEO films were first placed in a liquid ellipsometry cell supplied by J.A. Woollam Co. The cell was then filled with a solvent (water for PEO top layer film, ethanol for *l*PPh top film). The film was immersed for 30 min in the solvent. Then cell was filled with 0.2 mg/mL polymer solution in corresponding solvent (water for PEO or ethanol for *l*PPh) and the wet thickness data were collected. After film exposure, the cell was rinsed three times by 25 mL the corresponded solvent.

For the swollen films, a four-layer model was used, wherein the solvent was considered as the fourth layer, characterized as a semi-infinite transparent Cauchy medium. The dependence of refractive index on wavelength was determined prior to each measurement using a bare silicon wafer installed in the liquid cell. The four variables A , B , C , and thickness d were fitted simultaneously.

Atomic Force Microscopy studies were performed using a Bruker Dimension Icon AFM instrument in ScanAsyst mode using a ScanAsyst Fluid+ probe ($k = 0.7$ N/m, $f = 150$ kHz, $R = 2.0$ nm). All samples were immersed in DI water for 60 min prior to measurements to allow for equilibrated water uptake. Indentation was then induced with the tip in a contact mode by applying a force of 2-20 nN for 5 min. After that, the substrate containing the indented region was scanned continuously (scanned area $2 \times 2 \mu\text{m}$, resolution 256 points) in the ScanAsyst mode (an advanced version of the PeakForce tapping mode) using the same tip. The images were analyzed using the ProfilmOnline tool.

Neutron reflectometry measurements were performed at the Spallation Neutron Source Liquids Reflectometer at the Oak Ridge National Laboratory. The reflectivity data were collected using a sequence of 3.4-Å-wide continuous wavelength bands (selected from $2.55 \text{ \AA} < \lambda < 16.70 \text{ \AA}$) and incident angles (ranging over $0.6^\circ < \theta < 2.34^\circ$). The momentum transfer, $Q = (4\pi \sin \theta/\lambda)$, was varied over a range of $0.008 \text{ \AA}^{-1} < Q < 0.20 \text{ \AA}^{-1}$. Reflectivity curves were assembled by combining seven different wavelength and angle data sets together, maintaining a constant relative instrumental resolution of $\delta Q/Q = 0.023$ by varying the incident-beam apertures.

Neutron scattering densities within hydrogenated and deuterated stacks were averaged, each stack exhibiting its characteristic thickness, scattering density, and interlayer roughness. Those characteristic parameters were adjusted until the reflectivity curve was best fitted (minimized χ^2).

4.4. Results and discussion

Figure 4-1A illustrates deposition of hydrogen-bonded LbL films of linear polyphenol polymers with PEO on the surface of BPEI-primed silicon wafers. The four linear polyphenols used for film construction had either catechol-like structure with two hydroxyl groups (such as in P2HMA and P2HAA) or gallol-like structure with three hydroxyl groups in the benzene ring (such as in P3HMA and P3HAA), and either an acrylate or methacrylate polymer backbone. All *l*PPhs polymers, synthesized by RAFT polymerization had similar degrees of polymerization (DPs) of 190 ± 12 and polydispersity indices (PDIs) of 1.17 – 1.45. Synthesis of P2HMA and P3HMA is described in our previous work,³⁶ while procedures for synthesis and characterization of a new pair of linear polyphenols with an acrylic backbone (*i.e.* P2HAA and P3HAA) can be found in the Appendix C.

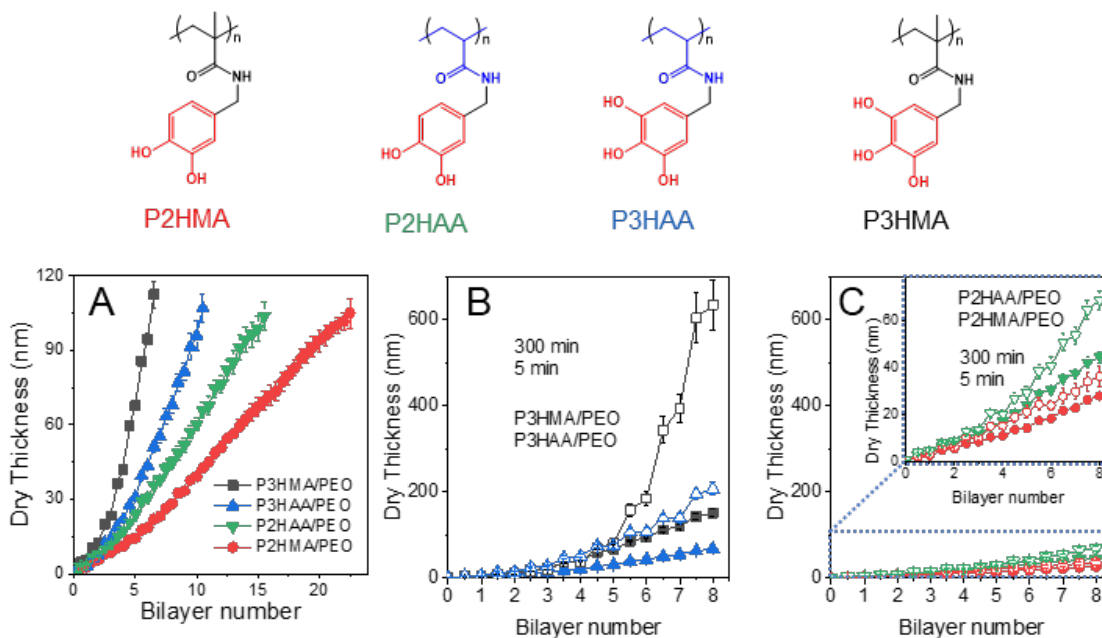


Figure 4-1 Dry thickness measured by spectroscopic ellipsometry during sequential deposition of *PPh*/PEO films from 0.2 mg/ml polymer solutions using a 5 min per layer deposition time (A), and a comparison of dry film thicknesses measured using deposition time of 5 min (solid symbols) and 300 min per layer (open symbols) for P3/PEO systems (B) and P2/PEO systems (C).

Figure 4-1A shows that the fastest increase in thickness occurs for the P3HMA/PEO system, with film thickness reaching 112 nm after as few as 6.5 bilayer deposition cycles, and the slowest thickness increase for the P2HMA/PEO system, with a total thickness of only 105 nm reached after deposition of as many as 22.5 bilayers. These differences in film growth are rationalized by a greater tendency of the P3HMA polymer to self-association through hydrogen binding between gallol polymer units as discussed in our prior publication.¹⁷¹ Note that the difference in film growth mode for polymers with catechol-like and gallol-like units was smaller for acrylate polymer backbones than it was for methacrylate backbones (acrylates P3HAA and P2HAA vs. methacrylates P3HMA and P2HMA), suggesting a possible effect of backbone hydrophobicity on self-association of polyphenol units. To further study the differences in the mechanism of *PPh*/PEO film growth brought about by the chemistry of polyphenol units, we

probed the diffusivity of polymers and its role in the accumulation of film mass. To that end, the deposition time was increased from 5 min to 300 min per layer. Figures 4-1B, C show that the effect of an increase in deposition time on dry film thickness was drastically different for P3HMA/PEO and P2HMA/PEO films, in agreement with the diffusive character of exponential vs. the non-diffusive character of linearly deposited films. Time-induced mass increase was the largest for the most exponential P3HMA/PEO film, and smallest for the P2HMA/PEO system, with the P3HAA/PEO and P2HAA/PEO systems exhibiting an intermediate rate of film thickness accumulation (Figures 4-1B,C). Interestingly, the long-term uptake of *l*PPh and PEO was highly asymmetric for exponential P3HMA/PEO films. P3HMA contributes most of the film mass increase (half-integer bilayer numbers in Figure 4-1B), reaching ~200 nm per layer for deposition of a 7-bilayer film, while the contribution of PEO to the film growth did not exceed 10-20 nm per layer. The larger amount of P3HMA is consistent with self-association of P3HMA polyphenol groups, which reduced the density of hydrogen-bonding sites of this polymer available to PEO.

To further understand this asymmetry in deposition of *l*PPh and PEO components during LbL assembly, kinetic experiments on each layer deposition were performed by *in situ* ellipsometry and complemented by dry thickness measurements of mass deposited within the films as they became saturated with each polymer. These experiments utilized films of matched dry thicknesses of 100 ± 5 nm followed by 5-min deposition cycles and capped with *l*PPh or PEO for further *in situ* PEO or *l*PPh deposition, respectively. The films were then pre-swollen in water or ethanol for 30 min (time $t = 0$ in Figures 4-2A and 4-2B), then PEO or *l*PPh solution was added to the *in situ* ellipsometry cell. Addition of 0.2 mg/ml PEO (Figure 4-2A) or *l*PPh solution (Figure 4-2B) resulted in changes in wet film thickness associated with incorporation of polymers within the films. For all films, adsorption of PEO was fast and levelled off after about 10 min. The amount

of PEO adsorbed on or absorbed by the films after 20 minutes (determined by the dry thickness increase measured by ellipsometry) systematically increased from 1.5 nm to 1.7 nm, 4.8 and 10.3 nm for P2HMA/PEO, P2HAA/PEO, P3HAA/PEO and P3HMA/PEO films, respectively. Regardless of the total mass adsorbed, PEO deposition for all the films was fast (Figure 4-2A). At the same time, large differences in the rate of increase of wet thickness were revealed for the different *l*PPhs: while film wet thicknesses equilibrated after ~5 minutes of exposure to P2HMA, other polyphenols showed ongoing long-term absorption within the films, which likely indicated slow penetration of the polyphenols into the LbL films (Figure 4-2B). The dry thickness increase due to uptake of *l*PPhs was 3.3 nm, 6.7 nm, 11.1 nm and 35.3 nm for P2HMA, P2HAA, P3HAA and P3HMA, respectively. Figure 4-2C shows that for uptake of PEO within *l*PPh-capped films, film swelling ratios (measured as the ratio of wet to dry ellipsometric thickness) varied between the different *l*PPh systems but did not change significantly after PEO uptake. Specifically, for the P2HMA/PEO film, the swelling ratios were 1.03 ± 0.08 and 1.10 ± 0.1 before and after 20-min PEO deposition, respectively. While the other *l*PPh/PEO films were more swollen, no significant changes were detected during PEO deposition.

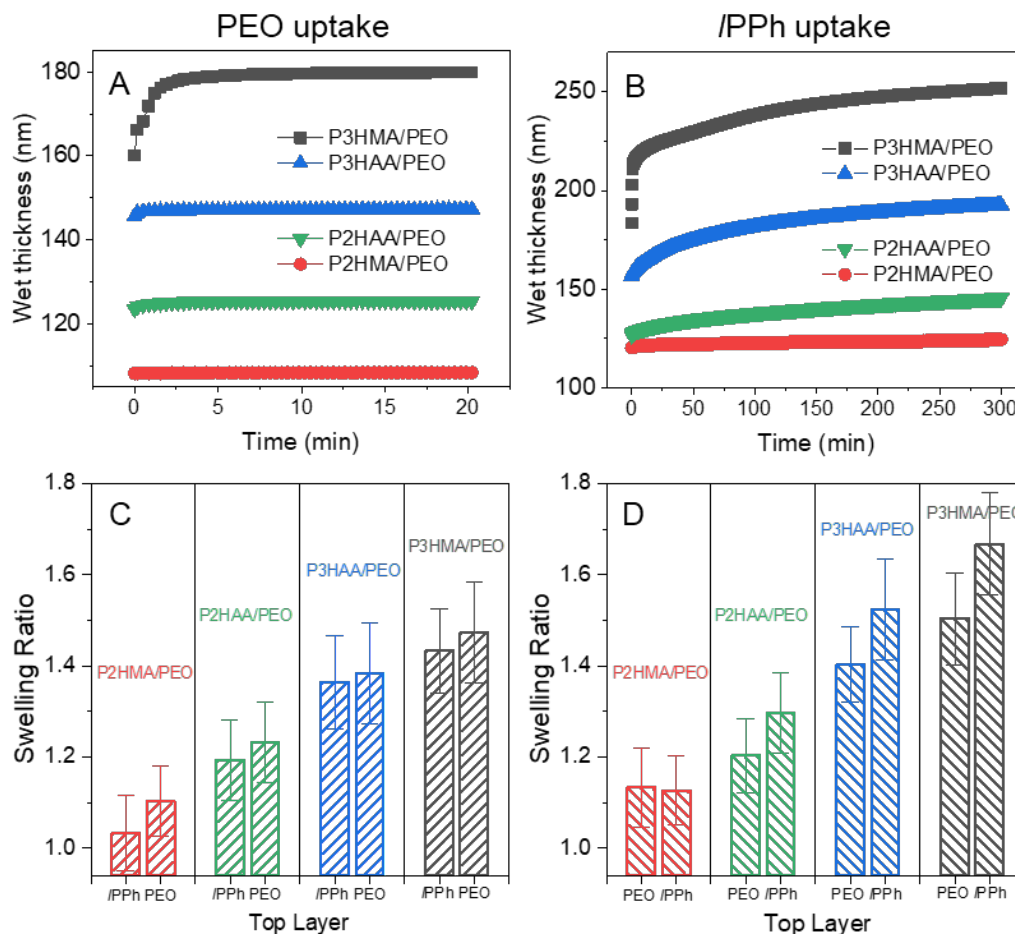


Figure 4-2 *In situ* spectroscopic ellipsometry measurements of the uptake of PEO or I/PPhs from 0.2 mg/ml aqueous or ethanol solutions (A and B, respectively) by ~100-nm I/PPh/PEO films constructed using 5-min per layer deposition time. Swelling ratios of I/PPh/PEO films in water (C) and ethanol (D) during the polymer uptake.

The highest swelling ratio was observed for P3HMA/PEO system, which featured the highest rate of exponential growth. For uptake of I/PPh within PEO-capped films, while changes in wet film thickness for most of I/PPh/PEO films occurred over long times (Figure 4-2B), and except for the P2HMA/PEO film whose swelling did not change before and after 300-min P2HMA deposition, swelling ratios of the other films slightly increased with I/PPh deposition time (Figure 4-2D). The refractive indices (RIs) obtained by fitting ellipsometry data for wet films using the Cauchy model with a constant value of A^{104} gave good fits with low mean square error values,

suggesting that the refractive indices of the swollen films can be assumed constant during polymer uptake. However, RIs were lower for P2/PEO films than those for P3/PEO films (1.487 and 1.485 for P2HMA/PEO, 1.493 and 1.491 for P2HAA/PEO, 1.510 and 1.513 for P3HAA/PEO, and 1.517 and 1.515 for P3HMA/PEO films during PEO and /PPh uptake, respectively (data not shown). The higher refractive indices of P3/PEO films, observed for the swollen films despite their higher solvent content (RI of water is 1.333 and RI of ethanol is 1.362) is explained by a larger fraction of P3 polymers in /PPh/PEO films, also seen in the data in Figure 4-1, and indicates that the RIs of /PPhs (which could not be directly determined in this study) are higher than that of PEO (RI 1.46).¹⁷² In the experiments shown in Figure 4-2, the greatest degree of film swelling caused by a long-term uptake of a polymer, observed for uptake of P3HMA within P3HMA/PEO films, was moderate (1.67 ± 0.11). This observation is drastically different from our earlier study of electrostatic exponential LbL films, which instead demonstrated dramatic increases in film swelling (from 2.4 to 3.8) upon invasion of polyelectrolyte chains from solution.⁴⁹ The two cases are clearly distinct because of the absence of electrostatic charge regulation and the osmotic pressure of counterions as factors controlling swelling of hydrogen-bonded films.

While at short times (up to 5 min) the binding of polymers in LbL is likely limited by solution flux, longer interaction times allow for rearrangement of assembled polymer chains and diffusion of polymer chains into the bulk of the films. The kinetics of /PPh uptake, shown in Figure 4-2B, enables estimation of rates and diffusion coefficients for the penetration of polyphenol chains into the film using a Fickian diffusion model: $Dt = q^2 H^2 / 4$, where D is the diffusion coefficient of deposited polymer chains through the wet polymer film, and q is the normalized mass uptake, calculated from measurements of wet film thickness as $(l_t - l_0) / (l_\infty - l_0)$, where l_0 , l_t , and l_∞ are the initial, effective (at time t), and equilibrium thicknesses of dry films, t is the exposure

time to a polyphenol solution, and H is the film wet thickness at time t as detected with spectroscopic ellipsometry. These estimates yield diffusion coefficients D for penetration of polyphenols through I Ph/PEO films which systematically decrease from $(6.2 \pm 0.6) \times 10^{-15} \text{ cm}^2/\text{s}$ for P3HMA/PEO to $(3.8 \pm 0.1) \times 10^{-16} \text{ cm}^2/\text{s}$ for P3HAA/PEO, and $(9.4 \pm 0.2) \times 10^{-17} \text{ cm}^2/\text{s}$ for P2HAA/PEO films, in agreement with the transition from a more exponential to a more linear growth mode for these films. In the case of P2HMA/PEO, the diffusion coefficient was lower than $10^{-18} \text{ cm}^2/\text{s}$ and was not quantified because of the uncertainty associated with the measurement of such slow diffusion over a short time. While these estimates are consistent with differences in film growth modes observed in I Ph/PEO films, the ellipsometry technique used for these measurements is unable to directly assess diffusivity of polymer chains. Moreover, asymmetry in the mass deposition of I Ph and PEO within the film poses a question of whether the PEO deposited within the film in much smaller amounts than I Ph can diffuse within the film during deposition, and thus support self-healing of these films in an aqueous environment.

To explore the diffusivity of PEO chains within I Ph/PEO films, we have used neutron reflectometry. In this technique, we took advantage of the contrast provided by deuterated polyethylene oxide (poly(ethylene glycol- d_4), d PEO) whose molecular weight and polydispersity (M_n 93,000 g/mol, PDI 1.07) were closely matched to those of hydrogenated PEO chains (h PEO, M_n 95,000 g/mol, PDI 1.08). Neutron reflectometry has been traditionally used to study the internal structure of LbL films after their assembly, and has been applied to both electrostatically assembled⁴⁹ and hydrogen-bonded films.¹⁷¹ In this paper, we instead designed an experiment in which pre-assembled hydrogenated films were exposed to a solution of d PEO for different time intervals and the diffusivity of film-invading chains was then accessed by measurements of the dry films. We used a similar approach previously to study chain diffusivity within electrostatically

assembled films.⁴⁹ In this work, hydrogenated *l*PPh/PEO films were deposited using a BPEI priming layer and a 5-min per layer deposition time to achieve a total thickness of ~100-110 nm. Maintaining constant thickness required assembly of a different number of layers for different *l*PPh/PEO pairs (Figure 4-1A). Specifically, the film thicknesses of 105.0 nm, 103.8 nm, 107.0 nm, and 112.0 nm were achieved with 22.5-bilayer 15.5-bilayer, 10.5-bilayer, and 5.5-bilayer films of P2HMA/PEO, P2HAA/PEO, P3HAA/PEO, and P3HMA/PEO films, respectively. For these experiments, all films containing a *l*PPh as a capping layer were exposed to a 0.2 mg/mL aqueous solution of *d*PEO for a sequence of time intervals to allow for observation of diffusion of the deuterated marker polymer through the hydrogenated film. The model used for the dry films included a silicon oxide layer, a BPEI priming layer, an underlying *d*PEO-poor layer (H-stack), and a surface layer (D-stack) whose scattering-length-density increases after exposure to the *d*PEO solution. The SLD values of hydrogenated and deuterated stacks (H-stack and D-stack, respectively) were determined by fitting the reflectivity data. This value is calculated as an integral of SLD over the film thickness and was fitted with all the parameters simultaneously.

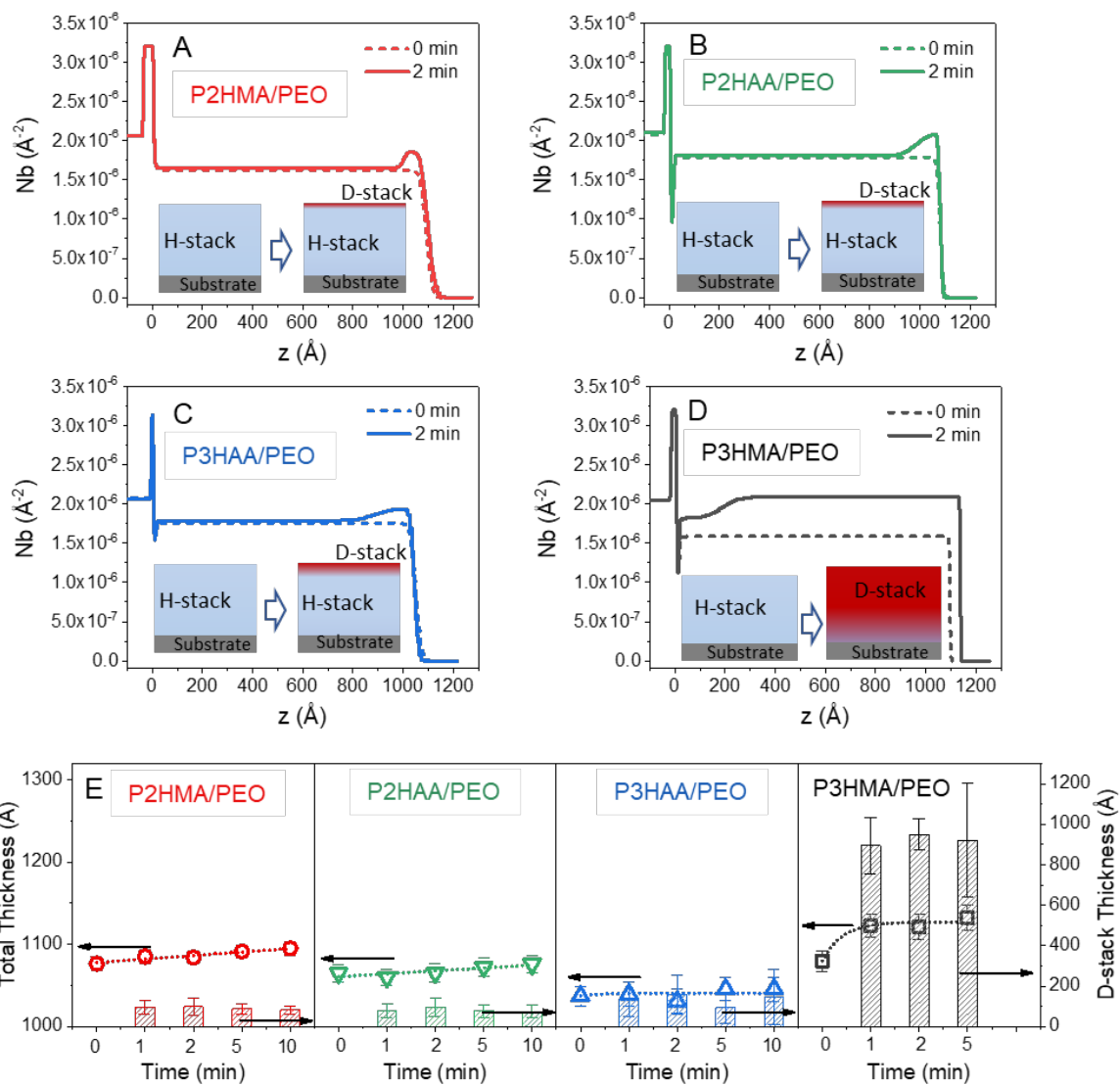


Figure 4-3 Scattering length density profiles (A-D) of hydrogenated *IPh*/PEO films before (dashed lines) and after (solid lines) a 2-min exposure to a 0.2 mg/mL *d*PEO aqueous solution for 22.5-bilayer P2HMA/PEO (A), 15.5-bilayer P2HAA/PEO (B), 10.5-bilayer P3HAA/PEO (C), and 6.5-bilayer P3HMA/PEO (D) films, as well as changes in the total film thickness (symbols) and thickness of the *d*PEO-rich surface layer (bars) upon exposure of *IPh*/PEO films to 0.2 mg/mL *d*PEO aqueous solutions for different times (E).

Figure 4-3 A–D shows neutron reflectivity data, SLD profiles of different *IPh*/PEO films upon exposure to *d*PEO solution, as well as schematic representations of uptake of *d*PEO by the films. Figure 4-3E summarizes the results of the neutron reflectometry studies. The linearly growing P2HMA/PEO film formed a *d*PEO-rich layer of dry thickness 9.1 ± 1.6 nm at the film

surface after 1-min exposure to a 0.2 mg/mL *d*PEO solution. Further exposure of this film to *d*PEO did not significantly change the SLD profile. These data demonstrate that *d*PEO does not penetrate deeply into the P2HMA/PEO hydrogenated matrix, but rather quickly accumulates at the film surface through diffusion from solution, in agreement with the ellipsometry data for uptake of hydrogenated PEO in Figure 4-2A. Similar results were observed for adsorption of *d*PEO onto the P2HAA/PEO hydrogenated film (Figure 4-3E), *i.e.* thickness of the deuterated layers remained constant at 8.1 ± 1.8 nm for all *d*PEO adsorption times of 1–10 min, suggesting that similarly to the P2HMA/PEO system, *d*PEO accumulated at the surface of the P2HAA/PEO hydrogenated matrix.

In contrast, gallol-based P3/PEO films demonstrated different trends for an uptake of deuterated PEO chains. As seen in Figure 4-3E, the interface between H-stacks and D-stacks was still located largely within the top region of the film for P3HAA/PEO system, but moved closer to the substrate for P3HMA/PEO films. Specifically, thickness of a D-stack for P3HAA/PEO film (13.3 ± 5.0 nm) were larger than that for P2/PEO systems, suggesting more diffusive nature of the film. Finally, for the most exponential P3HMA/PEO system, D-stack thicknesses were the largest, about 92.1 ± 10.8 nm, and comprised $\sim 85\%$ of film thickness. The larger thickness of D-stack reflects faster penetration and larger amount of *d*PEO absorbed by P3HMA/PEO in comparison to P3HAA/PEO film. Interestingly, SLD profiles measured during these experiments on invasion of *d*PEO chains in *l*PPH/PEO films did not show significant differences when the time of contact of films with *d*PEO solution was varied between 1 and 10 min, suggesting fast, sub-minute-scale, penetration of *d*PEO. This result is in stark contrast with our earlier findings for electrostatic systems, where evolution of the film SLD profile were observed for tens of minutes during uptake of a deuterated polycation, yielding diffusion coefficient of the order of 10^{-14} cm²/s.⁴⁹ The differences can be understood by more dynamic nature of hydrogen bonds as compared to

electrostatic pairing, and by an intrinsically high mobility of flexible PEO chains. Here, for the most diffusive P3HMA/PEO system, the lower bound of the diffusion coefficient for a 1-min uptake rate of *d*PEO within hydrogenated films of $\sim 5 \times 10^{-13} \text{ cm}^2/\text{s}$ was estimated assuming the simplest case of Fickian diffusion. The fast kinetics of PEO uptake is consistent with the timescale of PEO uptake by P3HMA/PEO films measured by *in situ* ellipsometry and shown in Figure 4-2A. At the same time, the diffusion coefficient for *d*PEO uptake derived from the neutron reflectometry is at least two orders of magnitude larger than that estimated for an uptake P3HMA chains using *in situ* ellipsometry in Figure 4-2B. These data again illustrate the asymmetric nature of dynamics of PEO and P3HMA chains in exponential hydrogen-bonded films.

While neutron reflectometry probed mobility of PEO chains within the film in the direction perpendicular to the substrate, the technique does not track mobility of hydrogenated *d*PPh chains and does not allow to follow mass transfer in the direction perpendicular to the substrate. To explore mass transfer of both *l*PPh and PEO chains and evaluate the ability of films to heal, we applied *in situ* atomic force microscopy and designed experiments to explore the self-healing properties for *l*PPh/PEO films. This technique has been previously used to study self-healing properties of non-LbL polymer films.¹⁷³⁻¹⁷⁵ Here, we used the procedure of mechanically indenting a film by an AFM tip followed by monitoring of film healing as a function of time. In a typical experiment, a *l*PPh/PEO film with dry thickness of about 400 nm was immersed in DI water, and its surface morphology was first analyzed by a Bruker Dimension Icon AFM instrument using a ScanAsyst Fluid+ tip. The film surface was then indented by the tip in a contact mode with a force of 2-20 nN for 5 min. After that, the damaged spot was scanned continuously in the ScanAsyst mode using the same tip while the film was continuously immersed in water.

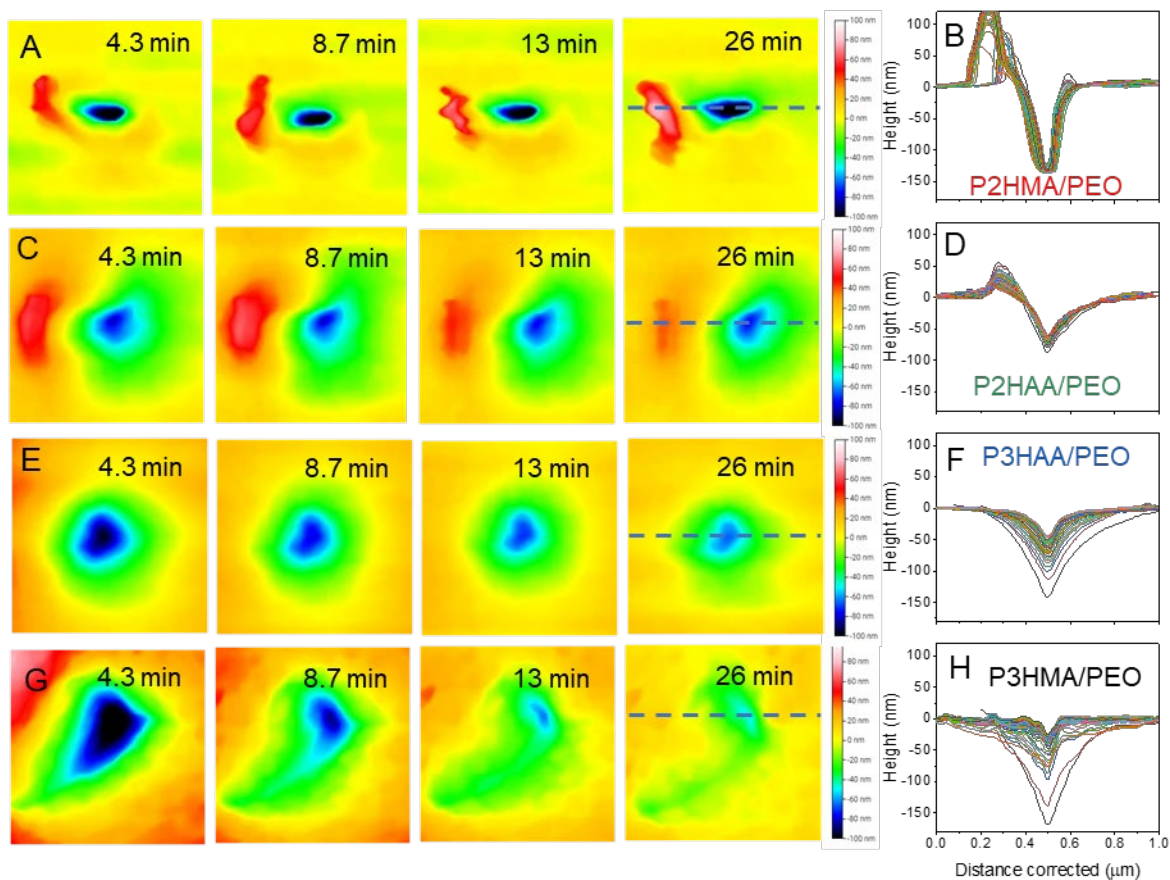


Figure 4-4 Self-healing of ~400-nm-thick *IPh*/PEO films measured by *in situ* AFM during immersion in water. AFM images and depth profiles of the indented areas as a function of time for P2HMA/PEO (A, B), P2HAA/PEO (C, D), P3HAA/PEO (E, F), and P3HMA/PEO (G, H) films, respectively.

Figure 4-4 shows *in situ* AFM images of the indented film and time evolution of the indented areas and depth profiles as a function of exposure time in water. Figure 4-4 A, B illustrate that in the case of P2HMA/PEO films, the area scans and depth profiles did not change with time, maintaining the depth of ~140 nm at the deepest point throughout the experimental timescale. This data show that the film built with catechol-like P2HMA did not exhibit self-healing properties. Another *IPh*/PEO film also composed of a catechol-like polymer but with acrylate rather than methacrylate backbone, *i.e.* P2HAA/PEO, exhibited negligible dynamic changes of the indented area (Figure 4-4 C, D). Self-healing behavior of films built with gallol-like polyphenols was much

more pronounced. Specifically, P3HAA/PEO system (Figure 4-4 E, F) showed continuous time evolution of both the indented area and the depth profile indicating significant film dynamics. P3HMA/PEO film exhibited superior self-healing and the fastest film dynamics among all the /PPh/PEO systems (Figure 4-4 G, H). The rate of self-healing is related to mass transport of the hydrogen-bonded polymer material from the bulk of the film into a void region. The time-resolved AFM data in Figure 4-4 allowed us to assess the rate of mass transport in the directions parallel and perpendicular to the substrate. However, because of the uncertainties associated with a specific shape of the indented area during indentation with an AFM tip, and the absence of analytical solution of the Fickian diffusion equation for materials of arbitrary shape, we have chosen not to derive specific values of diffusion coefficients for the mass transfer, but instead evaluate corresponding dynamics through half-recovery times.

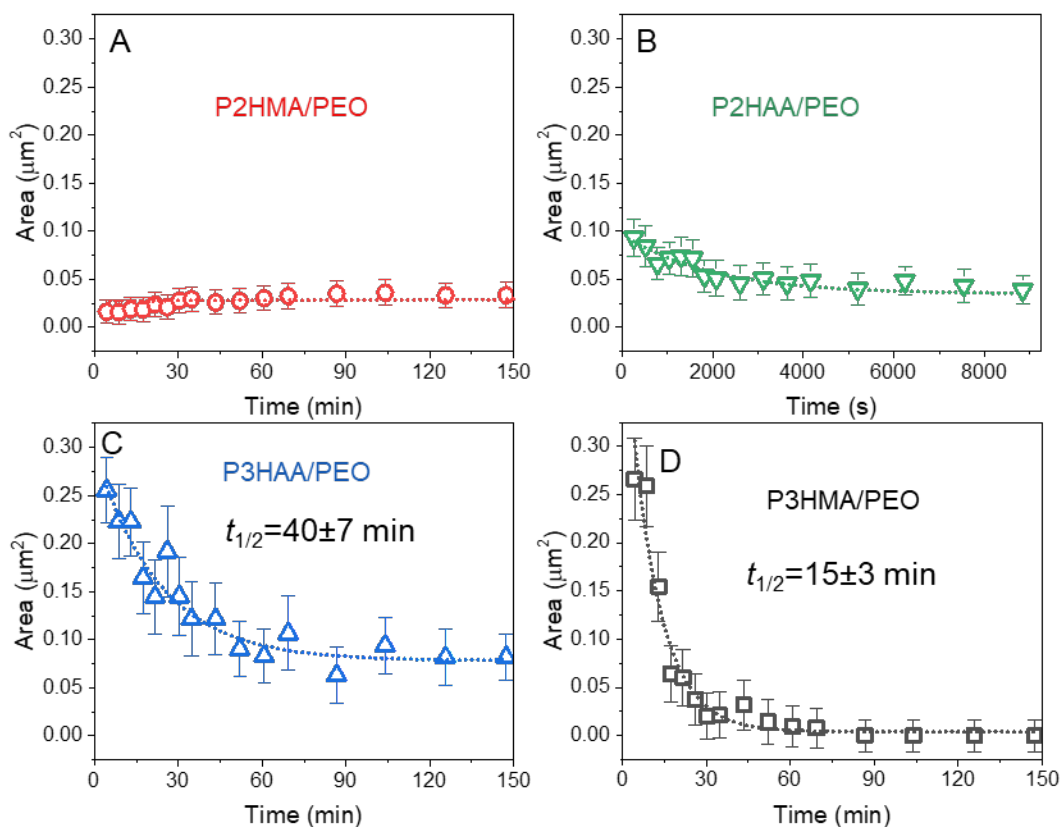


Figure 4-5 Time evolution of the lateral dimensions of the indented areas measured at the depth of 40 nm within the films using *in situ* AFM for P2HMA/PEO (A), P2HAA/PEO (B), P3HAA/PEO (C), and P3HMA/PEO (D) films during their continuous immersion in water.

Dynamics of *l*PPh/PEO films in the direction parallel to the substrate was evaluated from the time evolution of the cross-section of the indented areas at the depth of 40 nm from the film surface. This choice was made to avoid the top film region which has been demonstrated to have faster dynamics of polymer chains than the ‘bulk’ of the film,^{115,116,167} allow uniform comparison between different *l*PPh/PEO systems by eliminating possible effect of surface roughness on the estimated values. Figure 4-5A shows that with P2HMA/PEO films, the cross-sectional area did not reduce with time. Instead, even a slight increase in the size of the indent was observed, possibly due to the tip-induced effects caused by repeated scanning of the same area. This result is consistent with a complete absence of diffusivity in this system for >150 min of observation. Films

of another catechol-like polyphenol with the acrylate backbone (P2HAA) (Figure 4-5B) showed only slight dynamics, which was not, however, quantified here because of the negligible changes observed in depth profile that can be explained by the uncertainty, associated with the selection of surface reference line, which was significantly altered by the indentation tip (Figure 4-4D). P3HAA/PEO films exhibited faster healing, showing more pronounced change in the cross-section area from $0.26 \mu\text{m}^2$ to $0.08 \mu\text{m}^2$ after 150 min. Finally, the fastest dynamics and healing was observed for P3HMA/PEO films which demonstrated complete healing after 30-min immersion in water. The half-time of recovery in lateral direction lateral can be estimated as 40 ± 7 min and 15 ± 3 min for P3HAA/PEO and P3HMA/PEO systems, respectively. Evaluation of lateral mobility at the depth of 25 and 60 nm provided similar values of half-recovery time for all /PPh/PEO films (Figures C-2, C-3), indicating that depth of cross-sectional area, if it was not within the interfacial of the films, did not have a significant effect on the measurements of lateral mobility.

The results in Figure 4-4 can be also used for evaluating diffusivity of /PPh/PEO films in the direction perpendicular to substrate. Figure 4-6 shows time evolution of depth of the indented area for /PPh/PEO films. Similar results observed in the lateral direction, P2HMA/PEO and P2HAA/PEO films did not exhibit any significant mass transfer in the perpendicular direction, suggesting that, if present, dynamics was slower than the observation time (Figure 4-6 A, B). Again, gallol-containing systems (Figure 4-6 C, D) exhibited robust self-healing behavior, with the estimated half-recovery times of 60 ± 7 min and 20 ± 3 min, respectively P3HAA/PEO and P3HMA/PEO systems.

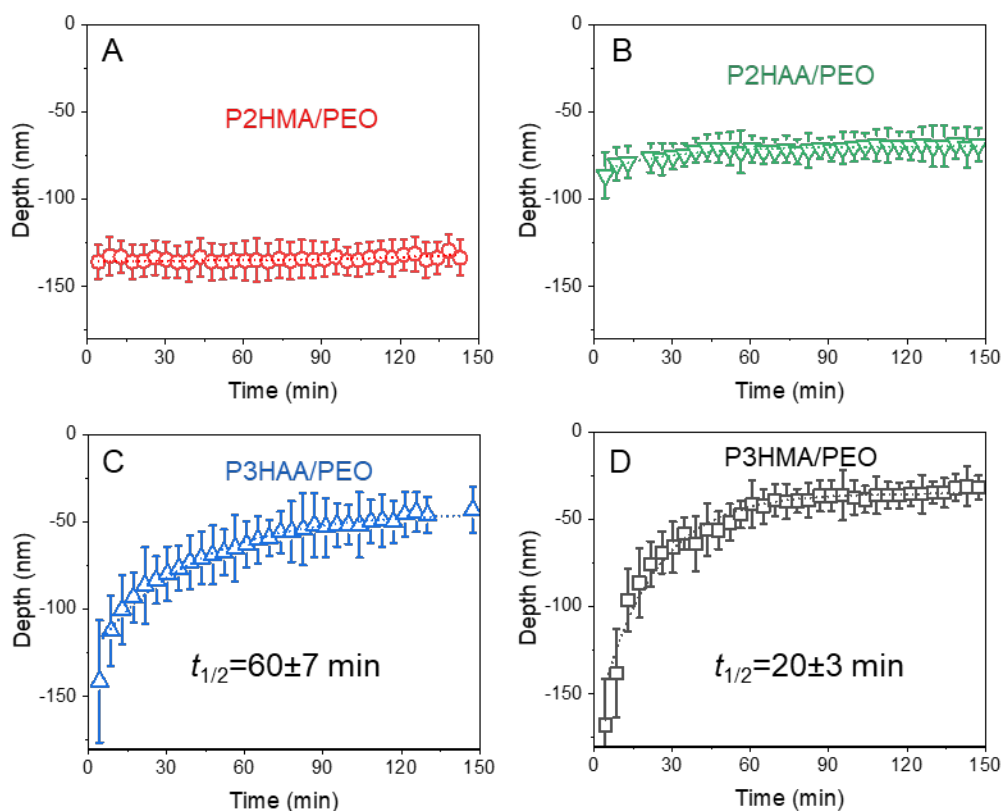


Figure 4-6 Time evolution of the deepest point of the indented areas measured using *in situ* AFM for P2HMA/PEO (A), P2HAA/PEO (B), P3HAA/PEO (C), and P3HMA/PEO (D) films during their continuous immersion in water.

The absence of mass transfer to the void area in both lateral and perpendicular direction for the most linear of *l*PPh/PEO systems, *i.e.* P2HMA/PEO and P2HAA/PEO (Figure 4-1) is consistent with the lack of penetration of PEO within bulk of the film detected in the neutron reflectometry experiments (Figure 4-3). For films built with gallol-like polyphenols (*i.e.* P3HAA/PEO and P3HMA/PEO films), much faster mass transfer occurred indicating a drastic enhancement of intermixing in these films. These data are also consistent with our earlier study of antioxidant activity of P2HMA/PEO and P3HMA/PEO films, which demonstrated drastic differences in the depth of penetration of films.¹⁷¹ Because polyphenol components comprised 70-80% of mass of the exponential P3HAA/PEO and P3HMA/PEO films, measurements of film

dynamics and self-healing using AFM were more sensitive to diffusion of the polyphenol components of the films, while neutron reflectometry experiments were selective to the mobility of a minority PEO component in the films. Assessment of the characteristic time scales for self-healing of P3/PEO films suggested that mass transfer in these films was likely isotropic in the direction parallel and perpendicular to the substrate, despite the surface-supported, layer-by-layer film deposition. Our finding of the low or even absent anisotropy of diffusion in PPh/PEO hydrogen-bonded systems are in contrast with high anisotropy easier reported to polyelectrolyte multilayer systems. For example, 10^4 – 10^5 faster polymer chain diffusion was found for poly(2-(dimethylamino)ethyl methacrylate) – poly(methacrylic acid) films expose to NaCl solutions.¹⁶⁷ Stratification of hydrogen-bonded LbL films in comparison to electrostatic multilayers is generally found to be weaker than that in electrostatic systems, and decay with the distance from the substrate.^{158,166} Note that direct measurements of the degree of film stratification at the highest above 200 nm from the substrate (such as those studied by AFM in this work) cannot be performed by neutron reflectometry, and that the decay of film stratification with distance from the substrate can contribute to the lack of anisotropy in mass transfer in hydrogen-bonded films. Overall weaker interpolymer interactions in hydrogen-bonded films can also be seen as one reason for this difference, although the lack of healing in P2/PEO films is not consistent with this explanation. The presence of electrostatic pairing, electrostatic barriers to layer intermixing and local charge control of ionic pair rearrangements in electrostatic systems could be responsible for the significant differences in structure and dynamics of electrostatic and hydrogen bonded LbL films.

In conclusion, we showed that structure of the polyphenol rings can strongly affect dynamics of hydrogen-bonded films, and evaluated such dynamics, using *in situ* ellipsometry, neutron reflectometry and *in situ* AFM techniques. A vast range of behavior, varying from non-

diffusive at the experimental time scale to fast self-healing upon exposure to aqueous solutions can be obtained for LbL films of polyphenols with different polyphenol repeat units. An interesting finding was a strongly asymmetric chain dynamics in P3/PEO assemblies with gallol structure of polyphenol rings, which demonstrated fast binding of flexible PEO chains with the top region of the film, or fast penetration of PEO within the entire LbL films. In contrast to fast diffusion of PEO chains, dynamics of film mass transfer during self-healing correlated with a much slower diffusion of P3 chains measured by *in situ* ellipsometry, suggesting that diffusion of P3 chains limits the transport associated P3/PEO chains within hydrogen-bonded films. However, more flexible PEO chains can achieve faster diffusion by exchange with other bound PEO chains in the film. Because of a significant antioxidant activity of PPh/PEO assemblies, experiments reported in this work can help to rationally construct functional coatings with both antioxidant and self-healing ability. Moreover, small molecules-competitors can be additionally used in future work to control hydrogen bonding⁴⁸ and self-healing behavior of these films.

4.5. Acknowledgments

The authors acknowledge the financial support of Texas A&M Experiment Station (TEES). Use of the TAMU Materials Characterization facility is acknowledged.

5. CONCLUSIONS

First, this work resulted in the development of a synthetic procedure for preparation of a new class of linear polyphenol homo- and copolymers containing gallol, catechol, and bromocatechol moieties. The synthetic route includes synthesis of protected polyphenol monomers, polymerization using RAFT technique, and deprotection steps. The living nature of polymerization was demonstrated, allowing to control length of polymeric chains with low dispersity.

Second, we demonstrated that the chemical structure of the polyphenol ring and the density of the polyphenol moieties in the polymer chains (in the case of copolymers) strongly controlled polymer ability to adsorb at solid surfaces within a monolayer, as well as form hydrogen-bonded LbL films with a hydrogen-bonded acceptor polymer. Polyphenolic polymers were capable of adhering to substrates of varied hydrophobicity, enabling control of surface wettability.

Third, we achieved LbL assembly of the synthesized polymers and showed fundamental differences in interactions of gallol- and catechol-based *PPhs* with hydrogen-bonded acceptor polymers. Specifically, gallol groups in *PPhs* were prone to intramolecular self-association, leading to exponential growth of LbL films, while catechol-based polyphenols showed linear growth as studied by spectroscopic ellipsometry. Using neutron reflectometry, we demonstrated that linear LbL films had stratified internal structure, whereas the exponential ones were highly intermixed. Moreover, we showed that *PPh* exponential films were more permeable to radical species and macromolecules, and established correlations between the degree of permeation and intermixing of polymer chains within the films. Importantly, the film functionality, *i.e.* its ability

to scavenge free radical from solution, was strongly controlled by the strength of interpolymer binding.

Finally, we demonstrated that the structure of polyphenol rings strongly affects dynamics of hydrogen-bonded films which varied from non-diffusive behavior to fast, minute-scale self-healing of damaged areas of LbL films upon their exposure to aqueous solutions. Hydrogen-bonded LbL films showed asymmetric chain dynamics in */PPh/PEO* assemblies with faster diffusion of PEO chains in comparison to */PPhs*. Interestingly, in contrast to polyelectrolyte multilayers, hydrogen-bonded assemblies showed lower ability to swell upon penetration of invading polymer chains, and demonstrates low anisotropy of mass transport in directions parallel and perpendicular to the substrate, likely due to absence of electrostatic barriers to chain diffusion.

Overall, exploration of hydrogen-bonded */PPh*-based LbL assemblies strengthens the knowledge base on correlations between intermolecular and intramolecular interactions within LbL films, and film structure and dynamics. Important similarities and differences between hydrogen-bonded LbL films and electrostatically assembled multilayers in their swelling, dynamics and structure can be rationalized through consideration of a wide range of strength of intermolecular binding in both cases, and the absence of electrostatic charge in hydrogen-bonded films.

Future work on antioxidant LbL coatings can be focused on attaining a better understanding of a specific mechanism of radical scavenging within antioxidant films. One possible mechanism involves oxidative crosslinking through polyphenol rings within the films, which can lead to enhanced mechanical properties and decreased permeability of the films to radical species. We envision that the diffusivity can be programmed by the strength of binding between components,

film swelling ratio, and flexibility of the polymer backbone. Finally, exploration of the competitive binding of low-molecular-weight hydrogen-bonding molecules within antioxidant films and the effect of such binding film characteristics and functional properties can be explored. The competitive interaction of active sites of polyphenol polymers with small molecules can be a key to controlling interpolymer interactions by programmed disruption of hydrogen-bonding within LbL films for guiding permeability, swelling, and self-healing properties of these materials.

REFERENCES

- (1) Larson, R. A. The antioxidants of higher plants. *Phytochemistry* **1988**, *27*, 969-978.
- (2) Cieřlik, E.; Gręda, A.; Adamus, W. Contents of polyphenols in fruit and vegetables. *Food Chemistry* **2006**, *94*, 135-142.
- (3) Podsedek, A. Natural antioxidants and antioxidant capacity of Brassica vegetables: A review. *LWT - Food Science and Technology* **2007**, *40*, 1-11.
- (4) Yashin, A.; Yashin, Y.; Xia, X.; Nemzer, B. Antioxidant Activity of Spices and Their Impact on Human Health: A Review. *Antioxidants (Basel)* **2017**, *6*, 70.
- (5) Graham, H. N. Green tea composition, consumption, and polyphenol chemistry. *Preventive medicine* **1992**, *21*, 334-350.
- (6) Garrido, J.; Borges, F. Wine and grape polyphenols — A chemical perspective. *Food Research International* **2013**, *54*, 1844-1858.
- (7) Yahfoufi, N.; Alsadi, N.; Jambi, M.; Matar, C. The Immunomodulatory and Anti-Inflammatory Role of Polyphenols. *Nutrients* **2018**, *10*.
- (8) Pandey, K. B.; Rizvi, S. I. Plant polyphenols as dietary antioxidants in human health and disease. *Oxid Med Cell Longev* **2009**, *2*, 270-278.
- (9) Zhao, J.; Fan, X.; Wang, S.; Li, S.; Shang, S.; Yang, Y.; Xu, N.; Lü, Y.; Shi, J. Bromophenol Derivatives from the Red Alga *Rhodomela confervoides*. *Journal of Natural Products* **2004**, *67*, 1032-1035.
- (10) Lingwood, M.; Hammond, J. R.; Hrovat, D. A.; Mayer, J. M.; Borden, W. T. MPW1K Performs Much Better than B3LYP in DFT Calculations on Reactions that Proceed by Proton-Coupled Electron Transfer (PCET). *Journal of Chemical Theory and Computation* **2006**, *2*, 740-745.
- (11) Waite, J. H.; Tanzer, M. L. The bioadhesive of *Mytilus byssus*: A protein containing L-DOPA. *Biochemical and Biophysical Research Communications* **1980**, *96*, 1554-1561.
- (12) Jamshidian, M.; Tehrani, E. A.; Imran, M.; Akhtar, M. J.; Cleymand, F.; Desobry, S. Structural, mechanical and barrier properties of active PLA-antioxidant films. *Journal of Food Engineering* **2012**, *110*, 380-389.
- (13) Hager, A.-S.; Vallons, K. J. R.; Arendt, E. K. Influence of Gallic Acid and Tannic Acid on the Mechanical and Barrier Properties of Wheat Gluten Films. *Journal of Agricultural and Food Chemistry* **2012**, *60*, 6157-6163.
- (14) Pant, A. F.; Sangerlaub, S.; Muller, K. Gallic Acid as an Oxygen Scavenger in Bio-Based Multilayer Packaging Films. *Materials (Basel, Switzerland)* **2017**, *10*, 489.
- (15) Iniguez-Franco, F.; Soto-Valdez, H.; Peralta, E.; Ayala-Zavala, J. F.; Auras, R.; Gamez-Meza, N. Antioxidant Activity and Diffusion of Catechin and Epicatechin from Antioxidant Active Films Made of Poly(l-lactic acid). *Journal of Agricultural and Food Chemistry* **2012**, *60*, 6515-6523.
- (16) Sun, X.; Wang, Z.; Kadouh, H.; Zhou, K. The antimicrobial, mechanical, physical and structural properties of chitosan-gallic acid films. *LWT - Food Science and Technology* **2014**, *57*, 83-89.
- (17) Luzi, F.; Fortunati, E.; Giovanale, G.; Mazzaglia, A.; Torre, L.; Balestra, G. M. Cellulose nanocrystals from *Actinidia deliciosa* pruning residues combined with carvacrol in

PVA_CH films with antioxidant/antimicrobial properties for packaging applications.

International Journal of Biological Macromolecules **2017**, *104*, 43-55.

(18) Nerín, C.; Tovar, L.; Salafranca, J. Behaviour of a new antioxidant active film versus oxidizable model compounds. *Journal of Food Engineering* **2008**, *84*, 313-320.

(19) Zhu, J.; Wu, H.; Sun, Q. Preparation of crosslinked active bilayer film based on chitosan and alginate for regulating ascorbate-glutathione cycle of postharvest cherry tomato (*Lycopersicon esculentum*). *International Journal of Biological Macromolecules* **2019**, *130*, 584-594.

(20) Gemili, S.; Yemenicioğlu, A.; Altınkaya, S. A. Development of antioxidant food packaging materials with controlled release properties. *Journal of Food Engineering* **2010**, *96*, 325-332.

(21) Liu, J.; Liu, S.; Chen, Y.; Zhang, L.; Kan, J.; Jin, C. Physical, mechanical and antioxidant properties of chitosan films grafted with different hydroxybenzoic acids. *Food Hydrocolloids* **2017**, *71*, 176-186.

(22) Xie, M.; Hu, B.; Wang, Y.; Zeng, X. Grafting of Gallic Acid onto Chitosan Enhances Antioxidant Activities and Alters Rheological Properties of the Copolymer. *Journal of Agricultural and Food Chemistry* **2014**, *62*, 9128-9136.

(23) Oh, D. X.; Kim, S.; Lee, D.; Hwang, D. S. Tunicate-mimetic nanofibrous hydrogel adhesive with improved wet adhesion. *Acta Biomaterialia* **2015**, *20*, 104-112.

(24) Hu, Q.; Wang, T.; Zhou, M.; Xue, J.; Luo, Y. In Vitro Antioxidant-Activity Evaluation of Gallic-Acid-Grafted Chitosan Conjugate Synthesized by Free-Radical-Induced Grafting Method. *Journal of Agricultural and Food Chemistry* **2016**, *64*, 5893-5900.

(25) Ryu, J. H.; Hong, S.; Lee, H. Bio-inspired adhesive catechol-conjugated chitosan for biomedical applications: A mini review. *Acta Biomaterialia* **2015**, *27*, 101-115.

(26) Ma, S.; Yuan, Q.; Zhang, X.; Yang, S.; Xu, J. Solvent effect on hydrogen-bonded thin film of poly(vinylpyrrolidone) and poly(acrylic acid) prepared by layer-by-layer assembly. *Colloids and Surfaces A: Physicochemical and Engineering Aspects* **2015**, *471*, 11-18.

(27) Lee, B. P.; Messersmith, P. B.; Israelachvili, J. N.; Waite, J. H. Mussel-Inspired Adhesives and Coatings. *Annual Review of Materials Research* **2011**, *41*, 99-132.

(28) Ahn, B. K.; Das, S.; Linstadt, R.; Kaufman, Y.; Martinez-Rodriguez, N. R.; Mirshafian, R.; Kesselman, E.; Talmon, Y.; Lipshutz, B. H.; Israelachvili, J. N.; Waite, J. H. High-performance mussel-inspired adhesives of reduced complexity. *Nature communications* **2015**, *6*, 8663.

(29) Ahn, B. K.; Lee, D. W.; Israelachvili, J. N.; Waite, J. H. Surface-initiated self-healing of polymers in aqueous media. *Nat Mater* **2014**, *13*, 867-872.

(30) Krogsgaard, M.; Behrens, M. A.; Pedersen, J. S.; Birkedal, H. Self-Healing Mussel-Inspired Multi-pH-Responsive Hydrogels. *Biomacromolecules* **2013**, *14*, 297-301.

(31) Olofsson, K.; Malkoch, M.; Hult, A. Facile synthesis of dopa-functional polycarbonates via thiol-ene-coupling chemistry towards self-healing gels. *Journal of Polymer Science Part A: Polymer Chemistry* **2016**, *54*, 2370-2378.

(32) Xia, N. N.; Rong, M. Z.; Zhang, M. Q. Stabilization of catechol-boronic ester bonds for underwater self-healing and recycling of lipophilic bulk polymer in wider pH range. *Journal of Materials Chemistry A* **2016**, *4*, 14122-14131.

- (33) Li, J.; Ejima, H.; Yoshie, N. Seawater-Assisted Self-Healing of Catechol Polymers via Hydrogen Bonding and Coordination Interactions. *ACS Applied Materials & Interfaces* **2016**, *8*, 19047-19053.
- (34) Shin, M.; Lee, H. Gallol-Rich Hyaluronic Acid Hydrogels: Shear-Thinning, Protein Accumulation against Concentration Gradients, and Degradation-Resistant Properties. *Chemistry of Materials* **2017**, *29*, 8211-8220.
- (35) Spizzirri, U. G.; Iemma, F.; Puoci, F.; Cirillo, G.; Curcio, M.; Parisi, O. I.; Picci, N. Synthesis of Antioxidant Polymers by Grafting of Gallic Acid and Catechin on Gelatin. *Biomacromolecules* **2009**, *10*, 1923-1930.
- (36) Hlushko, R.; Hlushko, H.; Sukhishvili, S. A. A family of linear phenolic polymers with controlled hydrophobicity, adsorption and antioxidant properties. *Polymer Chemistry* **2018**, *9*, 506-516.
- (37) Zhan, K.; Ejima, H.; Yoshie, N. Antioxidant and Adsorption Properties of Bioinspired Phenolic Polymers: A Comparative Study of Catechol and Gallol. *ACS Sustainable Chemistry & Engineering* **2016**, *4*, 3857-3863.
- (38) Decher, G.; Hong, J. D.; Schmitt, J. Buildup of ultrathin multilayer films by a self-assembly process: III. Consecutively alternating adsorption of anionic and cationic polyelectrolytes on charged surfaces. *Thin Solid Films* **1992**, *210-211*, 831-835.
- (39) Decher, G. Fuzzy Nanoassemblies: Toward Layered Polymeric Multicomposites. *Science* **1997**, *277*, 1232-1237.
- (40) Stockton, W. B.; Rubner, M. F. Molecular-Level Processing of Conjugated Polymers. 4. Layer-by-Layer Manipulation of Polyaniline via Hydrogen-Bonding Interactions. *Macromolecules* **1997**, *30*, 2717-2725.
- (41) Wang, L.; Wang, Z.; Zhang, X.; Shen, J.; Chi, L.; Fuchs, H. A new approach for the fabrication of an alternating multilayer film of poly(4-vinylpyridine) and poly(acrylic acid) based on hydrogen bonding. *Macromolecular Rapid Communications* **1997**, *18*, 509-514.
- (42) Kozlovskaya, V.; Ok, S.; Sousa, A.; Libera, M.; Sukhishvili, S. A. Hydrogen-Bonded Polymer Capsules Formed by Layer-by-Layer Self-Assembly. *Macromolecules* **2003**, *36*, 8590-8592.
- (43) Fu, Y.; Bai, S.; Cui, S.; Qiu, D.; Wang, Z.; Zhang, X. Hydrogen-Bonding-Directed Layer-by-Layer Multilayer Assembly: Reconfiguration Yielding Microporous Films. *Macromolecules* **2002**, *35*, 9451-9458.
- (44) Sukhishvili, S. A.; Granick, S. Layered, Erasable, Ultrathin Polymer Films. *Journal of the American Chemical Society* **2000**, *122*, 9550-9551.
- (45) Sukhishvili, S. A.; Granick, S. Layered, Erasable Polymer Multilayers Formed by Hydrogen-Bonded Sequential Self-Assembly. *Macromolecules* **2002**, *35*, 301-310.
- (46) Kotov, N. A. Layer-by-layer self-assembly: The contribution of hydrophobic interactions. *Nanostructured Materials* **1999**, *12*, 789-796.
- (47) Shutava, T.; Prouty, M.; Kommireddy, D.; Lvov, Y. pH Responsive Decomposable Layer-by-Layer Nanofilms and Capsules on the Basis of Tannic Acid. *Macromolecules* **2005**, *38*, 2850-2858.
- (48) Selin, V.; Aliakseyeu, A.; Ankner, J. F.; Sukhishvili, S. A. Effect of a Competitive Solvent on Binding Enthalpy and Chain Intermixing in Hydrogen-Bonded Layer-by-Layer Films. *Macromolecules* **2019**, *52*, 4432-4440.

- (49) Selin, V.; Ankner, J. F.; Sukhishvili, S. A. Nonlinear Layer-by-Layer Films: Effects of Chain Diffusivity on Film Structure and Swelling. *Macromolecules* **2017**, *50*, 6192-6201.
- (50) Caruso, F.; Niikura, K.; Furlong, D. N.; Okahata, Y. 2. Assembly of Alternating Polyelectrolyte and Protein Multilayer Films for Immunosensing. *Langmuir* **1997**, *13*, 3427-3433.
- (51) Schoeler, B.; Kumaraswamy, G.; Caruso, F. Investigation of the Influence of Polyelectrolyte Charge Density on the Growth of Multilayer Thin Films Prepared by the Layer-by-Layer Technique. *Macromolecules* **2002**, *35*, 889-897.
- (52) Picart, C.; Mutterer, J.; Richert, L.; Luo, Y.; Prestwich, G. D.; Schaaf, P.; Voegel, J. C.; Lavalle, P. Molecular basis for the explanation of the exponential growth of polyelectrolyte multilayers. *Proc Natl Acad Sci U S A* **2002**, *99*, 12531-12535.
- (53) Liu, G.; Zou, S.; Fu, L.; Zhang, G. Roles of Chain Conformation and Interpenetration in the Growth of a Polyelectrolyte Multilayer. *The Journal of Physical Chemistry B* **2008**, *112*, 4167-4171.
- (54) Xu, L.; Pristinski, D.; Zhuk, A.; Stoddart, C.; Ankner, J. F.; Sukhishvili, S. A. Linear versus Exponential Growth of Weak Polyelectrolyte Multilayers: Correlation with Polyelectrolyte Complexes. *Macromolecules* **2012**, *45*, 3892-3901.
- (55) Wang, X.; Liu, F.; Zheng, X.; Sun, J. Water-Enabled Self-Healing of Polyelectrolyte Multilayer Coatings. *Angewandte Chemie International Edition* **2011**, *50*, 11378-11381.
- (56) Cheng, M.; Shi, F.; Li, J.; Lin, Z.; Jiang, C.; Xiao, M.; Zhang, L.; Yang, W.; Nishi, T. Macroscopic Supramolecular Assembly of Rigid Building Blocks Through a Flexible Spacing Coating. *Advanced Materials* **2014**, *26*, 3009-3013.
- (57) Shahidi, F.; Janitha, P. K.; Wanasundara, P. D. Phenolic antioxidants. *Critical Reviews in Food Science and Nutrition* **1992**, *32*, 67-103.
- (58) Lingua, M. S.; Fabani, M. P.; Wunderlin, D. A.; Baroni, M. V. In vivo antioxidant activity of grape, pomace and wine from three red varieties grown in Argentina: Its relationship to phenolic profile. *Journal of Functional Foods* **2016**, *20*, 332-345.
- (59) Li, Y.; Yao, J.; Han, C.; Yang, J.; Chaudhry, M. T.; Wang, S.; Liu, H.; Yin, Y. Quercetin, Inflammation and Immunity. *Nutrients* **2016**, *8*, 167.
- (60) Moosavi, F.; Hosseini, R.; Saso, L.; Firuzi, O. Modulation of neurotrophic signaling pathways by polyphenols. *Drug Design, Development and Therapy* **2016**, *10*, 23-42.
- (61) Lin, Y.; Shi, R.; Wang, X.; Shen, H.-M. Luteolin, a Flavonoid with Potential for Cancer Prevention and Therapy. *Current cancer drug targets* **2008**, *8*, 634-646.
- (62) Fraga, C. G. Plant phenolics and human health: Biochemistry, nutrition, and pharmacology. *John Wiley & Sons, Inc., Hoboken* **2009**.
- (63) Margraf, T.; Santos, É. N. T.; de Andrade, E. F.; van Ruth, S. M.; Granato, D. Effects of geographical origin, variety and farming system on the chemical markers and in vitro antioxidant capacity of Brazilian purple grape juices. *Food Research International* **2016**, *82*, 145-155.
- (64) Hao, Y.; Sani, L. A.; Ge, T.; Fang, Q. The synergistic inhibition behaviour of tannic acid and iodide ions on mild steel in H₂SO₄ solutions. *Corrosion Science* **2017**, *123*, 158-169.

- (65) Erel-Unal, I.; Sukhishvili, S. A. Hydrogen-Bonded Multilayers of a Neutral Polymer and a Polyphenol. *Macromolecules* **2008**, *41*, 3962-3970.
- (66) Sahiner, N.; Sagbas, S.; Sahiner, M.; Demirci, S. Degradable tannic acid/polyethyleneimine polyplex particles with highly antioxidant and antimicrobial effects. *Polymer Degradation and Stability* **2016**, *133*, 152-161.
- (67) Kozlovskaya, V.; Xue, B.; Lei, W.; Padgett, L. E.; Tse, H. M.; Kharlampieva, E. Diabetes: Hydrogen-Bonded Multilayers of Tannic Acid as Mediators of T-Cell Immunity (Adv. Healthcare Mater. 5/2015). *Advanced Healthcare Materials* **2015**, *4*, 685-685.
- (68) Ejima, H.; Richardson, J. J.; Liang, K.; Best, J. P.; van Koeverden, M. P.; Such, G. K.; Cui, J.; Caruso, F. One-Step Assembly of Coordination Complexes for Versatile Film and Particle Engineering. *Science* **2013**, *341*, 154-157.
- (69) Fan, L.; Ma, Y.; Su, Y.; Zhang, R.; Liu, Y.; Zhang, Q.; Jiang, Z. Green coating by coordination of tannic acid and iron ions for antioxidant nanofiltration membranes. *RSC Advances* **2015**, *5*, 107777-107784.
- (70) Waite, J. H. Mussel Adhesion: Finding the Tricks Worth Mimicking. *The Journal of Adhesion* **2005**, *81*, 297-317.
- (71) Silverman, H. G.; Roberto, F. F. Understanding Marine Mussel Adhesion. *Marine Biotechnology* **2007**, *9*, 661-681.
- (72) Zhao, H.; Waite, J. H. Linking Adhesive and Structural Proteins in the Attachment Plaque of *Mytilus californianus*. *Journal of Biological Chemistry* **2006**, *281*, 26150-26158.
- (73) Yamamoto, H. Synthesis and adhesive studies of marine polypeptides. *Journal of the Chemical Society, Perkin Transactions 1* **1987**, 613-618.
- (74) Yamamoto, H. Adhesive studies of synthetic polypeptides: A model for marine adhesive proteins. *Journal of Adhesion Science and Technology* **1987**, *1*, 177-183.
- (75) Yang, W. J.; Tao, X.; Zhao, T.; Weng, L.; Kang, E.-T.; Wang, L. Antifouling and antibacterial hydrogel coatings with self-healing properties based on a dynamic disulfide exchange reaction. *Polymer Chemistry* **2015**, *6*, 7027-7035.
- (76) Payra, D.; Naito, M.; Fujii, Y.; Yamada, N. L.; Hiromoto, S.; Singh, A. Bioinspired adhesive polymer coatings for efficient and versatile corrosion resistance. *RSC Advances* **2015**, *5*, 15977-15984.
- (77) Matos-Pérez, C. R.; White, J. D.; Wilker, J. J. Polymer Composition and Substrate Influences on the Adhesive Bonding of a Biomimetic, Cross-Linking Polymer. *Journal of the American Chemical Society* **2012**, *134*, 9498-9505.
- (78) Isakova, A.; Topham, P. D.; Sutherland, A. J. Controlled RAFT Polymerization and Zinc Binding Performance of Catechol-Inspired Homopolymers. *Macromolecules* **2014**, *47*, 2561-2568.
- (79) Patil, N.; Falentin-Daudre, C.; Jerome, C.; Detrembleur, C. Mussel-inspired protein-repelling ambivalent block copolymers: controlled synthesis and characterization. *Polymer Chemistry* **2015**, *6*, 2919-2933.
- (80) Leibig, D.; Müller, A. H. E.; Frey, H. Anionic Polymerization of Vinylcatechol Derivatives: Reversal of the Monomer Gradient Directed by the Position of the Catechol Moiety in the Copolymerization with Styrene. *Macromolecules* **2016**, *49*, 4792-4801.
- (81) Jenkins, C. L.; Siebert, H. M.; Wilker, J. J. Integrating Mussel Chemistry into a Bio-Based Polymer to Create Degradable Adhesives. *Macromolecules* **2017**, *50*, 561-568.

- (82) Li, K.; Li, X.-M.; Gloer, J. B.; Wang, B.-G. Isolation, Characterization, and Antioxidant Activity of Bromophenols of the Marine Red Alga *Rhodomela confervoides*. *Journal of Agricultural and Food Chemistry* **2011**, *59*, 9916-9921.
- (83) Javan, A. J.; Javan, M. J.; Tehrani, Z. A. Theoretical Investigation on Antioxidant Activity of Bromophenols from the Marine Red Alga *Rhodomela confervoides*: H-Atom vs Electron Transfer Mechanism. *Journal of Agricultural and Food Chemistry* **2013**, *61*, 1534-1541.
- (84) Patil, N.; Cordella, D.; Aqil, A.; Debuigne, A.; Admassie, S.; Jérôme, C.; Detrembleur, C. Surface- and Redox-Active Multifunctional Polyphenol-Derived Poly(ionic liquid)s: Controlled Synthesis and Characterization. *Macromolecules* **2016**, *49*, 7676-7691.
- (85) Zhan, K.; Kim, C.; Sung, K.; Ejima, H.; Yoshie, N. Tunicate-Inspired Gallol Polymers for Underwater Adhesive: A Comparative Study of Catechol and Gallol. *Biomacromolecules* **2017**, *18*, 2959-2966.
- (86) Keddie, D. J.; Moad, G.; Rizzardo, E.; Thang, S. H. RAFT Agent Design and Synthesis. *Macromolecules* **2012**, *45*, 5321-5342.
- (87) Cauët, S. I.; Wooley, K. L. Kinetic investigation of the RAFT polymerization of p-acetoxystyrene. *Journal of polymer science. Part A, Polymer chemistry* **2010**, *48*, 2517-2524.
- (88) Coates, J.: Interpretation of Infrared Spectra, A Practical Approach. In *Encyclopedia of Analytical Chemistry*; John Wiley & Sons, Ltd, 2006.
- (89) Takahashi, A.; Kawaguchi, M.: The structure of macromolecules adsorbed on interfaces. In *Behavior of Macromolecules*; Springer Berlin Heidelberg: Berlin, Heidelberg, 1982; pp 1-65.
- (90) Dietrich, S. W.; Jorgensen, E. C.; Kollman, P. A.; Rothenberg, S. A theoretical study of intramolecular hydrogen bonding in ortho-substituted phenols and thiophenols. *Journal of the American Chemical Society* **1976**, *98*, 8310-8324.
- (91) Kharlampieva, E.; Sukhishvili, S. A. Ionization and pH Stability of Multilayers Formed by Self-Assembly of Weak Polyelectrolytes. *Langmuir* **2003**, *19*, 1235-1243.
- (92) Pant, A. F.; Sänglerlaub, S.; Müller, K. Gallic Acid as an Oxygen Scavenger in Bio-Based Multilayer Packaging Films. *Materials* **2017**, *10*, 489.
- (93) Selin, V.; Ankner, F. J.; Sukhishvili, A. S. Ionically Paired Layer-by-Layer Hydrogels: Water and Polyelectrolyte Uptake Controlled by Deposition Time. *Gels* **2018**, *4*.
- (94) Kharlampieva, E.; Sukhishvili, S. A. Release of a Dye from Hydrogen-Bonded and Electrostatically Assembled Polymer Films Triggered by Adsorption of a Polyelectrolyte. *Langmuir* **2004**, *20*, 9677-9685.
- (95) Pavlukhina, S.; Zhuk, I.; Mentbayeva, A.; Rautenberg, E.; Chang, W.; Yu, X.; van de Belt-Gritter, B.; Busscher, H. J.; van der Mei, H. C.; Sukhishvili, S. A. Small-molecule-hosting nanocomposite films with multiple bacteria-triggered responses. *Npg Asia Materials* **2014**, *6*, e121.
- (96) Mentbayeva, A.; Ospanova, A.; Tashmuhambetova, Z.; Sokolova, V.; Sukhishvili, S. Polymer–Metal Complexes in Polyelectrolyte Multilayer Films as Catalysts for Oxidation of Toluene. *Langmuir* **2012**, *28*, 11948-11955.
- (97) Kozlovskaya, V.; Shamaev, A.; Sukhishvili, S. A. Tuning swelling pH and permeability of hydrogel multilayer capsules. *Soft Matter* **2008**, *4*, 1499-1507.

- (98) Ninan, N.; Forget, A.; Shastri, V. P.; Voelcker, N. H.; Blencowe, A. Antibacterial and Anti-Inflammatory pH-Responsive Tannic Acid-Carboxylated Agarose Composite Hydrogels for Wound Healing. *ACS Applied Materials & Interfaces* **2016**, *8*, 28511-28521.
- (99) Kozlovskaya, V.; Xue, B.; Lei, W.; Padgett, L. E.; Tse, H. M.; Kharlampieva, E. Hydrogen-Bonded Multilayers of Tannic Acid as Mediators of T Cell Immunity. *Advanced healthcare materials* **2015**, *4*, 686-694.
- (100) Hlushko, H.; Cubides, Y.; Hlushko, R.; Kelly, T. M.; Castaneda, H.; Sukhishvili, S. A. Hydrophobic Antioxidant Polymers for Corrosion Protection of an Aluminum Alloy. *ACS Sustainable Chemistry & Engineering* **2018**, *6*, 14302-14313.
- (101) Rahim, M. A.; Kristufek, S. L.; Pan, S.; Richardson, J. J.; Caruso, F. Phenolic Building Blocks for the Assembly of Functional Materials. *Angewandte Chemie International Edition* **2019**, *58*, 1904-1927.
- (102) Ryu, J. H.; Messersmith, P. B.; Lee, H. Polydopamine Surface Chemistry: A Decade of Discovery. *ACS Applied Materials & Interfaces* **2018**, *10*, 7523-7540.
- (103) Dubas, S. T.; Schlenoff, J. B. Factors controlling the growth of polyelectrolyte multilayers. *Macromolecules* **1999**, *32*, 8153-8160.
- (104) Woollam, J. A.; Johs, B. D.; Herzinger, C. M.; Hilfiker, J. N.; Synowicki, R. A.; Bungay, C. L.: *Overview of variable-angle spectroscopic ellipsometry (VASE): I. Basic theory and typical applications*; SPIE, 1999; Vol. 10294. pp. OP.
- (105) Oliver, W. C.; Pharr, G. M. Measurement of hardness and elastic modulus by instrumented indentation: Advances in understanding and refinements to methodology. *Journal of Materials Research* **2011**, *19*, 3-20.
- (106) Nolte, A. J.; Rubner, M. F.; Cohen, R. E. Determining the Young's Modulus of Polyelectrolyte Multilayer Films via Stress-Induced Mechanical Buckling Instabilities. *Macromolecules* **2005**, *38*, 5367-5370.
- (107) Cai, H.; Liu, X.; Zou, J.; Xiao, J.; Yuan, B.; Li, F.; Cheng, Q. Multi-wavelength spectrophotometric determination of hydrogen peroxide in water with peroxidase-catalyzed oxidation of ABTS. *Chemosphere* **2018**, *193*, 833-839.
- (108) Garza, J. M.; Schaaf, P.; Muller, S.; Ball, V.; Stoltz, J.-F.; Voegel, J.-C.; Lavallo, P. Multicompartment Films Made of Alternate Polyelectrolyte Multilayers of Exponential and Linear Growth. *Langmuir* **2004**, *20*, 7298-7302.
- (109) Bieker, P.; Schönhoff, M. Linear and Exponential Growth Regimes of Multilayers of Weak Polyelectrolytes in Dependence on pH. *Macromolecules* **2010**, *43*, 5052-5059.
- (110) Cohen, Y.; Evan-Salem, T.; Avram, L. Hydrogen-Bonded Hexameric Capsules of Resorcin[4]arene, Pyrogallol[4]arene and Octahydroxypyridine[4]arene are Abundant Structures in Organic Solvents: A View from Diffusion NMR. *Supramol. Chem.* **2008**, *20*, 71-79.
- (111) International Union of, P.; Applied, C.; Commission on Equilibrium, D.; Serjeant, E. P.; Dempsey, B.; International Union of, P.; Applied, C.; Commission on Electrochemical, D.: *Ionisation constants of organic acids in aqueous solution*; Pergamon Press: Oxford; New York, 1979.
- (112) Ricci, A.; Olejar, K. J.; Parpinello, G. P.; Kilmartin, P. A.; Versari, A. Application of Fourier Transform Infrared (FTIR) Spectroscopy in the Characterization of Tannins. *Applied Spectroscopy Reviews* **2015**, *50*, 407-442.

- (113) Mitsuzuka, A.; Fujii, A.; Ebata, T.; Mikami, N. Infrared Spectroscopy of Intramolecular Hydrogen-Bonded OH Stretching Vibrations in Jet-Cooled Methyl Salicylate and Its Clusters. *The Journal of Physical Chemistry A* **1998**, *102*, 9779-9784.
- (114) Dimitrova, Y. Theoretical study of the changes in the vibrational characteristics arising from the hydrogen bonding between Vitamin C (l-ascorbic acid) and H₂O. *Spectrochimica Acta Part A: Molecular and Biomolecular Spectroscopy* **2006**, *63*, 427-437.
- (115) Xu, L.; Selin, V.; Zhuk, A.; Ankner, J. F.; Sukhishvili, S. A. Molecular Weight Dependence of Polymer Chain Mobility within Multilayer Films. *ACS Macro Letters* **2013**, *2*, 865-868.
- (116) Selin, V.; Ankner, J. F.; Sukhishvili, S. A. Diffusional Response of Layer-by-Layer Assembled Polyelectrolyte Chains to Salt Annealing. *Macromolecules* **2015**, *48*, 3983-3990.
- (117) Selin, V.; Ankner, J. F.; Sukhishvili, S. A. Ionically Paired Layer-by-Layer Hydrogels: Water and Polyelectrolyte Uptake Controlled by Deposition Time. *Gels* **2018**, *4*, 7.
- (118) McAloney, R. A.; Dudnik, V.; Goh, M. C. Kinetics of Salt-Induced Annealing of a Polyelectrolyte Multilayer Film Morphology. *Langmuir* **2003**, *19*, 3947-3952.
- (119) Prior, R. L.; Wu, X.; Schaich, K. Standardized Methods for the Determination of Antioxidant Capacity and Phenolics in Foods and Dietary Supplements. *Journal of Agricultural and Food Chemistry* **2005**, *53*, 4290-4302.
- (120) Hotta, H.; Nagano, S.; Ueda, M.; Tsujino, Y.; Koyama, J.; Osakai, T. Higher radical scavenging activities of polyphenolic antioxidants can be ascribed to chemical reactions following their oxidation. *Biochimica et Biophysica Acta (BBA) - General Subjects* **2002**, *1572*, 123-132.
- (121) Koleva, I. I.; Niederländer, H. A. G.; van Beek, T. A. Application of ABTS Radical Cation for Selective On-Line Detection of Radical Scavengers in HPLC Eluates. *Analytical Chemistry* **2001**, *73*, 3373-3381.
- (122) Tian, X.; Schaich, K. M. Effects of Molecular Structure on Kinetics and Dynamics of the Trolox Equivalent Antioxidant Capacity Assay with ABTS+•. *Journal of Agricultural and Food Chemistry* **2013**, *61*, 5511-5519.
- (123) Siquet, C.; Paiva-Martins, F.; Lima, J. L. F. C.; Reis, S.; Borges, F. Antioxidant profile of dihydroxy- and trihydroxyphenolic acids-A structure-activity relationship study. *Free Radical Research* **2006**, *40*, 433-442.
- (124) Lehaf, A. M.; Hariri, H. H.; Schlenoff, J. B. Homogeneity, Modulus, and Viscoelasticity of Polyelectrolyte Multilayers by Nanoindentation: Refining the Buildup Mechanism. *Langmuir* **2012**, *28*, 6348-6355.
- (125) Huang, D.; Ou, B.; Prior, R. L. The Chemistry behind Antioxidant Capacity Assays. *Journal of Agricultural and Food Chemistry* **2005**, *53*, 1841-1856.
- (126) Kandaswami, C.; Vaidyanathan, C. S. Oxidation of catechol in plants. *Biochem J* **1972**, *128*, 30P-31P.
- (127) Huang, Z.; Yu, L.; Dai, Y.; Wang, H. Hydrogen bonding interactions between N,N-dimethylformamide and cysteine: DFT studies of structures, properties, and topologies. *Structural Chemistry* **2011**, *22*, 57-65.
- (128) Zhang, C.; Ren, Z.; Liu, L.; Yin, Z. Modelling hydrogen bonds in NN-dimethylformamide. *Molecular Simulation* **2013**, *39*, 875-881.

- (129) Khutoryanskiy, V.; Staikos, G.: *Hydrogen-Bonded Interpolymer Complexes*; World Scientific Publishing Co. Pte. Ltd., 2009.
- (130) Wang, Y. H.; He, J.; Aktas, S.; Sukhishvili, S. A.; Kalyon, D. M. Rheological behavior and self-healing of hydrogen-bonded complexes of a triblock Pluronic((R)) copolymer with a weak polyacid. *J Rheol* **2017**, *61*, 1103-1119.
- (131) Selin, V.; Aliakseyeu, A.; Ankner, J. F.; Sukhishvili, S. A. Effect of a Competitive Solvent on Binding Enthalpy and Chain Intermixing in Hydrogen-Bonded Layer-by-Layer Films. *Macromolecules* **2019**.
- (132) Jennings, K. R. Spectrometric identification of organic compounds (Fifth Edition) R. M. SILVERSTEIN, G. C. BASSLER AND T. C. MORRILL. Wiley, New York, 1991. No. of pages: 430. ISBN 0471 63404 2. Price: £50.25, \$76.10. *Organic Mass Spectrometry* **1991**, *26*, 813-813.
- (133) Shukla, A.; Almeida, B. Advances in cellular and tissue engineering using layer-by-layer assembly. *WIREs Nanomedicine and Nanobiotechnology* **2014**, *6*, 411-421.
- (134) Gentile, P.; Ferreira, A. M.; Callaghan, J. T.; Miller, C. A.; Atkinson, J.; Freeman, C.; Hatton, P. V. Multilayer Nanoscale Encapsulation of Biofunctional Peptides to Enhance Bone Tissue Regeneration In Vivo. *Advanced Healthcare Materials* **2017**, *6*, 1601182.
- (135) Gentile, P.; Ghione, C.; Ferreira, A. M.; Crawford, A.; Hatton, P. V. Alginate-based hydrogels functionalised at the nanoscale using layer-by-layer assembly for potential cartilage repair. *Biomaterials Science* **2017**, *5*, 1922-1931.
- (136) Pavlukhina, S.; Sukhishvili, S. Polymer assemblies for controlled delivery of bioactive molecules from surfaces. *Advanced Drug Delivery Reviews* **2011**, *63*, 822-836.
- (137) Liu, X.; Han, F.; Zhao, P.; Lin, C.; Wen, X.; Ye, X. Layer-by-layer self-assembled multilayers on PEEK implants improve osseointegration in an osteoporosis rabbit model. *Nanomedicine: Nanotechnology, Biology and Medicine* **2017**, *13*, 1423-1433.
- (138) Liljeström, V.; Ora, A.; Hassinen, J.; Rekola, H. T.; Nonappa; Heilala, M.; Hynninen, V.; Joensuu, J. J.; Ras, R. H. A.; Törmä, P.; Ikkala, O.; Kostianen, M. A. Cooperative colloidal self-assembly of metal-protein superlattice wires. *Nature communications* **2017**, *8*, 671.
- (139) Kharlampieva, E.; Kozlovskaya, V.; Sukhishvili, S. A. Layer-by-Layer Hydrogen-Bonded Polymer Films: From Fundamentals to Applications. *Advanced Materials* **2009**, *21*, 3053-3065.
- (140) Borges, J.; Mano, J. F. Molecular Interactions Driving the Layer-by-Layer Assembly of Multilayers. *Chemical Reviews* **2014**, *114*, 8883-8942.
- (141) Quinn, J. F.; Johnston, A. P. R.; Such, G. K.; Zelikin, A. N.; Caruso, F. Next generation, sequentially assembled ultrathin films: beyond electrostatics. *Chemical Society Reviews* **2007**, *36*, 707-718.
- (142) Quinn, J. F.; Caruso, F. Facile Tailoring of Film Morphology and Release Properties Using Layer-by-Layer Assembly of Thermoresponsive Materials. *Langmuir* **2004**, *20*, 20-22.
- (143) DeLongchamp, D. M.; Hammond, P. T. Highly Ion Conductive Poly(ethylene oxide)-Based Solid Polymer Electrolytes from Hydrogen Bonding Layer-by-Layer Assembly. *Langmuir* **2004**, *20*, 5403-5411.
- (144) Kozlovskaya, V.; Harbaugh, S.; Drachuk, I.; Shchepelina, O.; Kelley-Loughnane, N.; Stone, M.; Tsukruk, V. V. Hydrogen-bonded LbL shells for living cell surface engineering. *Soft Matter* **2011**, *7*, 2364-2372.

- (145) Kozlovskaya, V.; Kharlampieva, E.; Drachuk, I.; Cheng, D.; Tsukruk, V. V. Responsive microcapsule reactors based on hydrogen-bonded tannic acid layer-by-layer assemblies. *Soft Matter* **2010**, *6*, 3596-3608.
- (146) Kozlovskaya, V.; Wang, Y.; Higgins, W.; Chen, J.; Chen, Y.; Kharlampieva, E. pH-triggered shape response of cubical ultrathin hydrogel capsules. *Soft Matter* **2012**, *8*, 9828-9839.
- (147) Liu, F.; Kozlovskaya, V.; Zavgorodnya, O.; Martinez-Lopez, C.; Catledge, S.; Kharlampieva, E. Encapsulation of anticancer drug by hydrogen-bonded multilayers of tannic acid. *Soft Matter* **2014**, *10*, 9237-9247.
- (148) Pham-Hua, D.; Padgett, L. E.; Xue, B.; Anderson, B.; Zeiger, M.; Barra, J. M.; Bethea, M.; Hunter, C. S.; Kozlovskaya, V.; Kharlampieva, E.; Tse, H. M. Islet encapsulation with polyphenol coatings decreases pro-inflammatory chemokine synthesis and T cell trafficking. *Biomaterials* **2017**, *128*, 19-32.
- (149) Decher, G.: Layer-by-Layer Assembly (Putting Molecules to Work). In *Multilayer Thin Films*; pp 1-21.
- (150) Elbert, D. L.; Herbert, C. B.; Hubbell, J. A. Thin Polymer Layers Formed by Polyelectrolyte Multilayer Techniques on Biological Surfaces. *Langmuir* **1999**, *15*, 5355-5362.
- (151) Ruths, J.; Essler, F.; Decher, G.; Riegler, H. Polyelectrolytes I: Polyanion/Polycation Multilayers at the Air/Monolayer/Water Interface as Elements for Quantitative Polymer Adsorption Studies and Preparation of Hetero-superlattices on Solid Surfaces. *Langmuir* **2000**, *16*, 8871-8878.
- (152) Jang, Y.; Seo, J.; Akgun, B.; Satija, S.; Char, K. Molecular Weight Dependence on the Disintegration of Spin-Assisted Weak Polyelectrolyte Multilayer Films. *Macromolecules* **2013**, *46*, 4580-4588.
- (153) Nazaran, P.; Bosio, V.; Jaeger, W.; Anghel, D. F.; v. Klitzing, R. Lateral Mobility of Polyelectrolyte Chains in Multilayers. *The Journal of Physical Chemistry B* **2007**, *111*, 8572-8581.
- (154) Kharlampieva, E.; Ankner, J. F.; Rubinstein, M.; Sukhishvili, S. A. H^+ -Induced Release of Polyanions from Multilayer Films. *Physical Review Letters* **2008**, *100*, 128303.
- (155) Wong, J. E.; Zastrow, H.; Jaeger, W.; von Klitzing, R. Specific Ion versus Electrostatic Effects on the Construction of Polyelectrolyte Multilayers. *Langmuir* **2009**, *25*, 14061-14070.
- (156) Selin, V.; Ankner, J. F.; Sukhishvili, S. A. Ionically Paired Layer-by-Layer Hydrogels: Water and Polyelectrolyte Uptake Controlled by Deposition Time. *Gels* **2018**, *4*.
- (157) Kharlampieva, E.; Sukhishvili, S. A. Hydrogen-Bonded Layer-by-Layer Polymer Films. *Journal of Macromolecular Science, Part C* **2006**, *46*, 377-395.
- (158) Kharlampieva, E.; Kozlovskaya, V.; Ankner, J. F.; Sukhishvili, S. A. Hydrogen-Bonded Polymer Multilayers Probed by Neutron Reflectivity. *Langmuir* **2008**, *24*, 11346-11349.
- (159) Guan, Y.; Zhang, Y. Dynamically bonded layer-by-layer films: Dynamic properties and applications. *Journal of Applied Polymer Science* **2014**, *131*.
- (160) Zhao, Y.-N.; Gu, J.; Jia, S.; Guan, Y.; Zhang, Y. Zero-order release of polyphenolic drugs from dynamic, hydrogen-bonded LBL films. *Soft Matter* **2016**, *12*, 1085-1092.

- (161) Grdadolnik, J.; Merzel, F.; Avbelj, F. Origin of hydrophobicity and enhanced water hydrogen bond strength near purely hydrophobic solutes. *Proceedings of the National Academy of Sciences* **2017**, *114*, 322.
- (162) Zhuk, A.; Selin, V.; Zhuk, I.; Belov, B.; Ankner, J. F.; Sukhishvili, S. A. Chain Conformation and Dynamics in Spin-Assisted Weak Polyelectrolyte Multilayers. *Langmuir* **2015**, *31*, 3889-3896.
- (163) Fortier-McGill, B.; Reven, L. 2H NMR Studies of Polymer Multilayer Capsules, Films, and Complexes. *Macromolecules* **2009**, *42*, 247-254.
- (164) Soltwedel, O.; Ivanova, O.; Nestler, P.; Müller, M.; Köhler, R.; Helm, C. A. Interdiffusion in Polyelectrolyte Multilayers. *Macromolecules* **2010**, *43*, 7288-7293.
- (165) Jomaa, H. W.; Schlenoff, J. B. Salt-Induced Polyelectrolyte Interdiffusion in Multilayered Films: A Neutron Reflectivity Study. *Macromolecules* **2005**, *38*, 8473-8480.
- (166) Xu, L.; Ankner, J. F.; Sukhishvili, S. A. Steric Effects in Ionic Pairing and Polyelectrolyte Interdiffusion within Multilayered Films: A Neutron Reflectometry Study. *Macromolecules* **2011**, *44*, 6518-6524.
- (167) Xu, L.; Kozlovskaya, V.; Kharlampieva, E.; Ankner, J. F.; Sukhishvili, S. A. Anisotropic Diffusion of Polyelectrolyte Chains within Multilayer Films. *ACS Macro Letters* **2012**, *1*, 127-130.
- (168) Dubas, S. T.; Schlenoff, J. B. Swelling and Smoothing of Polyelectrolyte Multilayers by Salt. *Langmuir* **2001**, *17*, 7725-7727.
- (169) Ghostine, R. A.; Jisr, R. M.; Leahaf, A.; Schlenoff, J. B. Roughness and Salt Annealing in a Polyelectrolyte Multilayer. *Langmuir* **2013**, *29*, 11742-11750.
- (170) Fortier-McGill, B.; Toader, V.; Reven, L. Chain Dynamics of Water-Saturated Hydrogen-Bonded Polymer Complexes and Multilayers. *Macromolecules* **2011**, *44*, 2755-2765.
- (171) Hlushko, R.; Ankner, J. F.; Sukhishvili, S. A. Layer-by-Layer Hydrogen-Bonded Antioxidant Films of Linear Synthetic Polyphenols. *Macromolecules* **2020**, *53*, 1033-1042.
- (172) Al-Faleh, R. S.; Zihlif, A. M. A study on optical absorption and constants of doped poly(ethylene oxide). *Physica B: Condensed Matter* **2011**, *406*, 1919-1925.
- (173) South, A. B.; Lyon, L. A. Autonomic Self-Healing of Hydrogel Thin Films. *Angewandte Chemie International Edition* **2010**, *49*, 767-771.
- (174) Kratz, K.; Narasimhan, A.; Tangirala, R.; Moon, S.; Revanur, R.; Kundu, S.; Kim, H. S.; Crosby, A. J.; Russell, T. P.; Emrick, T.; Kolmakov, G.; Balazs, A. C. Probing and repairing damaged surfaces with nanoparticle-containing microcapsules. *Nature Nanotechnology* **2012**, *7*, 87-90.
- (175) Yoon, J. A.; Kamada, J.; Koynov, K.; Mohin, J.; Nicolaÿ, R.; Zhang, Y.; Balazs, A. C.; Kowalewski, T.; Matyjaszewski, K. Self-Healing Polymer Films Based on Thiol-Disulfide Exchange Reactions and Self-Healing Kinetics Measured Using Atomic Force Microscopy. *Macromolecules* **2012**, *45*, 142-149.
- (176) Sui, X.; Shao, C.; Liu, Y. Photoluminescence of polyethylene oxide-ZnO composite electrospun fibers. *Polymer* **2007**, *48*, 1459-1463.
- (177) Tang, S.; Shao, C.; Liu, Y.; Li, S.; Mu, R. Electrospun nanofibers of poly(ethylene oxide)/teraamino-phthalocyanine copper(II) hybrids and its photoluminescence properties. *Journal of Physics and Chemistry of Solids* **2007**, *68*, 2337-2340.
- (178) Chigome, S.; Ajao, J. A.; Fasasi, A. Y.; Torto, N.; Osinkolu, G. A.; Maaza, M. Synthesis and Substrate-Aided Alignment of Porphyrinated Poly(ethylene oxide) (PEO)

Electrospun Nanofibers AU - Abiona, Adurafimihan A. *International Journal of Polymeric Materials and Polymeric Biomaterials* **2010**, 59, 818-827.

APPENDIX A

SUPPORTING INFORMATION FOR THE CHAPTER 2

Table A-1 P2HzHex series and PHex.

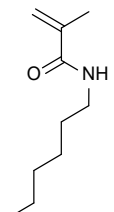
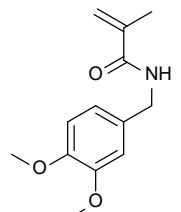
Targeted molar content, %	Polymerization			Deprotection reaction	
	 N-hexyl methacrylamide (1)	 N-(3,4-dimethoxybenzyl) methacrylamide (5)	Yield (%)	Polymer	2M BBr ₃ in CH ₂ Cl ₂
0	1.94 g	-	88	-	-
5	1.84 g	0.135 g	83	0.500 g	0.300 mL
10	1.75 g	0.270 g	83	0.509 g	0.500 mL
15	1.65 g	0.405 g	77	0.520 g	0.700 mL
100	-	2.70 g	73	0.680 g	4.50 mL

Table A-2 PBrHzHex series.

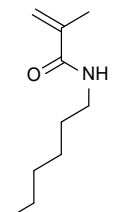
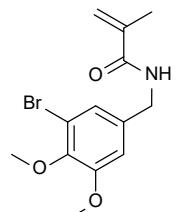
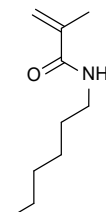
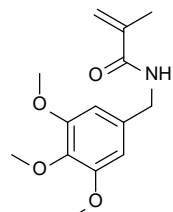
Targeted molar content, %	Polymerization			Deprotection reaction	
	 N-hexyl methacrylamide (1)	 N-(3,4-dimethoxy-5-bromobenzyl) methacrylamide (6)	Yield (%)	Polymer	2M BBr ₃ in CH ₂ Cl ₂
5	1.84 g	0.180 g	75	0.500 g	0.300 mL
10	1.75 g	0.361 g	73	0.532 g	0.500 mL
15	1.65 g	0.541 g	68	0.550 g	0.700 mL
100	-	3.60 g	59	0.910 g	4.50 mL

Table A-3 P3HzHex series.

Targeted molar content, %	Polymerization			Deprotection reaction	
	 N-hexyl methacrylamide (1)	 N-(3,4,5-trimethoxybenzyl) methacrylamide (7)	Yield (%)	Polymer	2M BBr ₃ in CH ₂ Cl ₂
5	1.84 g	0.152 g	81	0.503 g	0.400 mL
10	1.75 g	0.307 g	79	0.517 g	0.700 mL
15	1.65 g	0.457 g	82	0.530 g	1.00 mL
100	-	3.04 g	76	0.770 g	6.50 mL

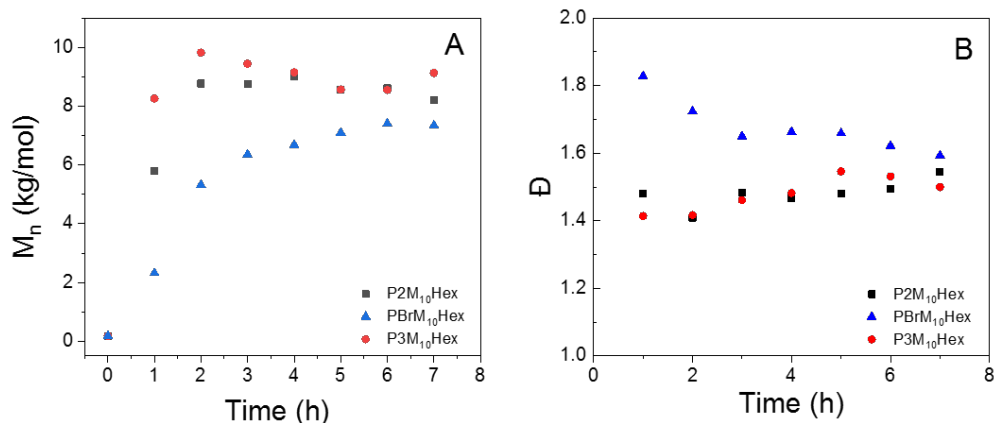


Figure A-1 The number-average molecular weight M_n (A) and molar mass dispersities (B) as a function of polymerization time during synthesis of P2M₁₀Hex, PBrM₁₀Hex, or P3M₁₀Hex at 80°C.

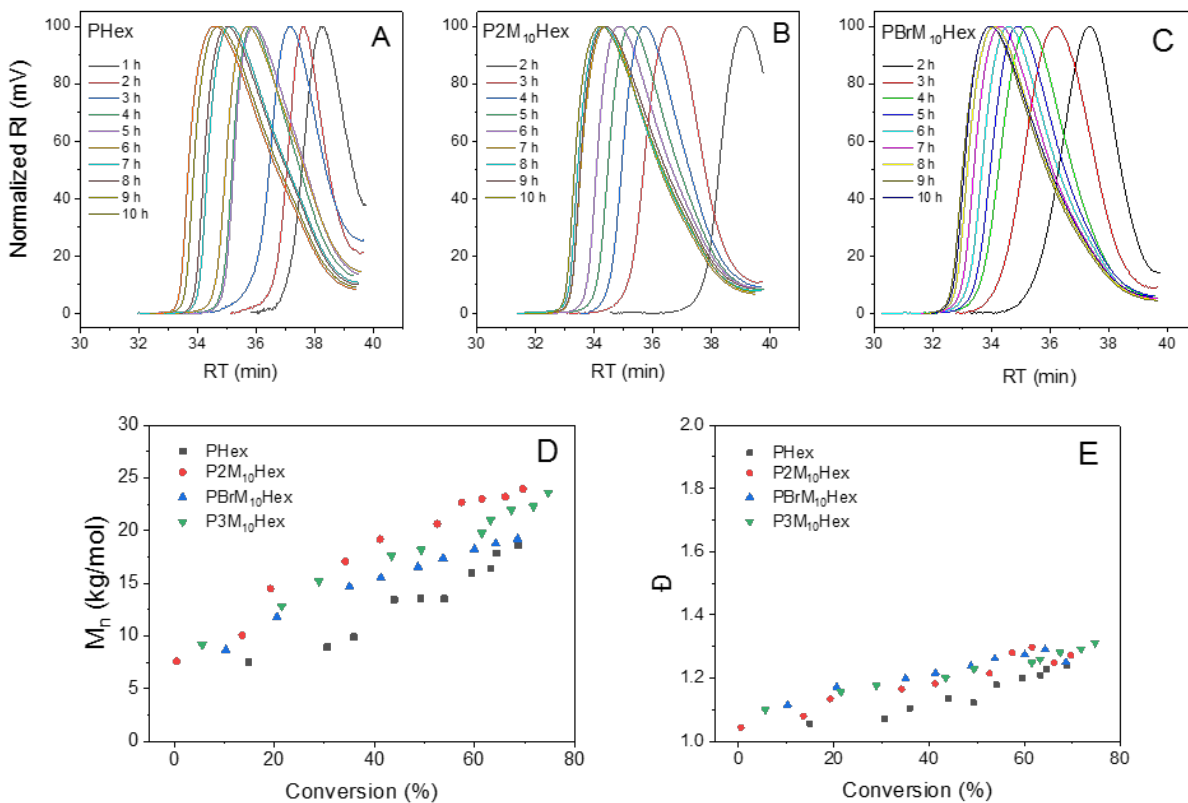


Figure A-2 GPC traces of PHex (A), P2M₁₀Hex (B), PBrM₁₀Hex (C) for different polymerization times, as well as M_n (D) and molar mass dispersities (E) as a function of monomer conversion during polymerization of PHex homopolymer and copolymers containing 10% of phenolic precursor groups at 70°C.

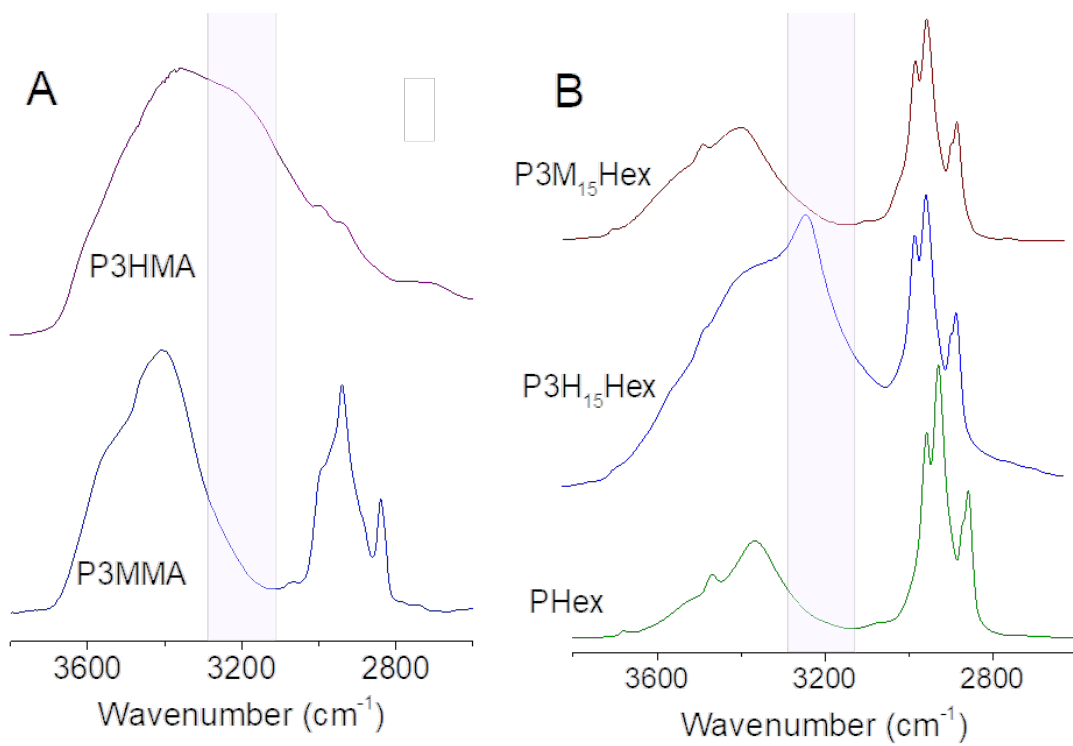


Figure A-3 FTIR spectra of protected and deprotected P3MMA and P3HMA homopolymers (A), P3M₁₅Hex and P3H₁₅Hex copolymers (B, top) and PHex control polymer (B, bottom).

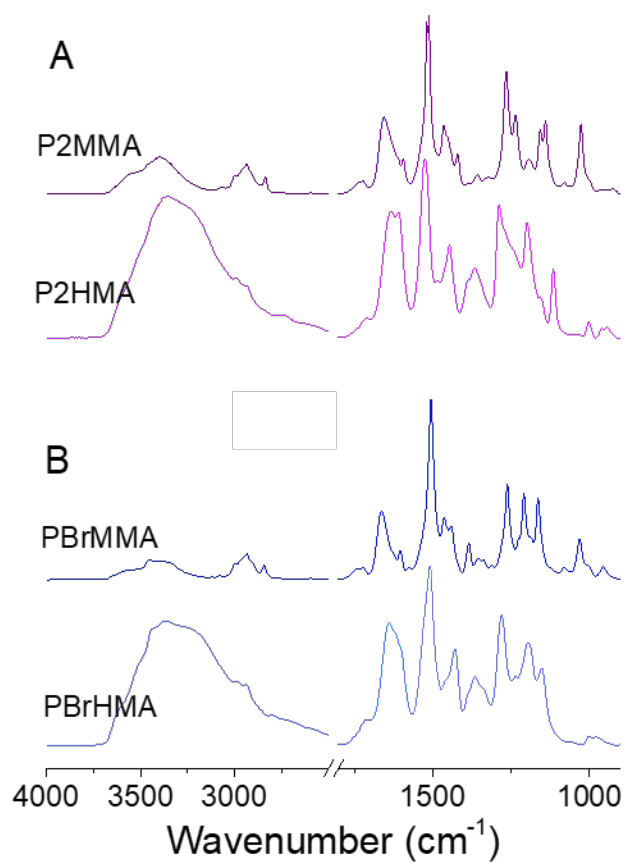


Figure A-4 FTIR spectra of protected and deprotected homopolymers: P2MMA and P2HMA (A), and PBrMMA and PBrHMA (B).

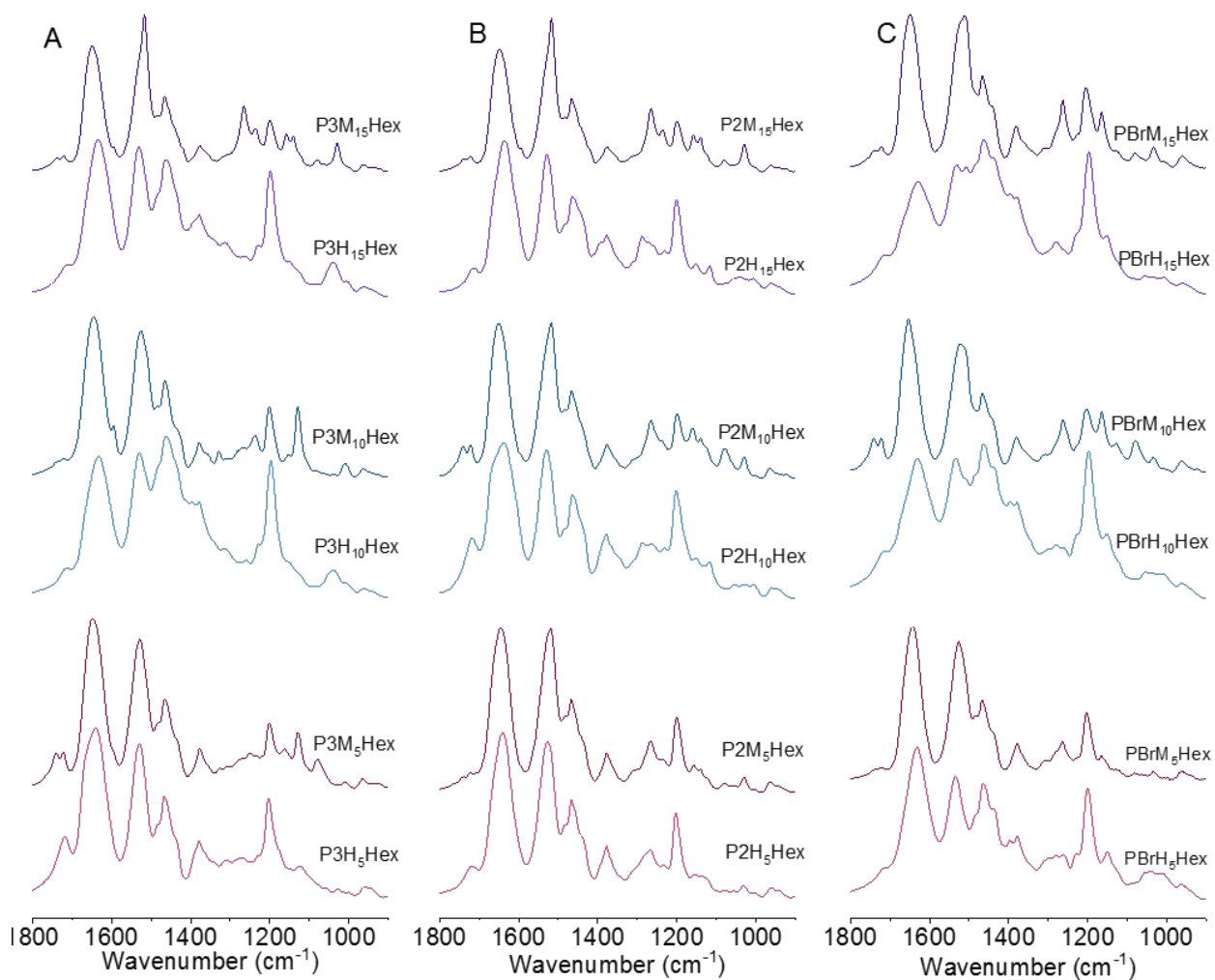


Figure A-5 FTIR spectra of the copolymers of P3MzHex and P3HzHex series (A), P2MzHex and P2HzHex series (B), as well as PBrMzHex and PBrHzHex series (C).

APPENDIX B

SUPPORTING INFORMATION FOR THE CHAPTER 3*

Table B-1 Dry thicknesses measured by ellipsometry during deposition of a (P3HMA/PEO)₂/P3HMA/*d*PEO/P3HMA/PEO/P3HMA/*d*PEO film.

Bilayer Number	Top Layer	Thickness (nm)
0	BPEI	1.0
0.5	P3HMA	3.6
1	PEO	4.3
1.5	P3HMA	10.6
2	<i>d</i> PEO	12.2
2.5	P3HMA	23.8
3	PEO	26.3
3.5	P3HMA	43.4
4	<i>d</i> PEO	48.9

Table B-2 Dry thicknesses measured by ellipsometry during deposition of a (P2HMA/PEO)₂/(P2HMA/*d*PEO)₂/(P2HMA/PEO)₇/(P2HMA/*d*PEO)₂ film.

Bilayer Number	Top Layer	Thickness (nm)
0	BPEI	0.7
0.5	P2HMA	2.0
1	PEO	2.6
1.5	P2HMA	6.1
2	PEO	6.7

*Reprinted with permission from: Hlushko, R.; Ankner, J. A.; Sukhishvili, S. A. Layer-by-Layer Hydrogen-Bonded Antioxidant Films of Linear Synthetic Polyphenol. *Macromolecules* **2020**, Copyright American Chemical Society.

2.5	P2HMA	10.9
3	dPEO	10.8
3.5	P2HMA	12.0
4	dPEO	12.7
4.5	P2HMA	14.6
5	PEO	15.2
5.5	P2HMA	15.4
6	P2HMA + PEO	15.4
7	P2HMA + PEO	23.0
8	P2HMA + PEO	27.8
9	P2HMA + PEO	33.4
10	P2HMA + PEO	39.9
11	P2HMA + PEO	47.4
11.5	P2HMA	54.2
12	dPEO	55.0
12.5	P2HMA	59.4
13	dPEO	60.2

Table B-3 Model parameters for a (P3HMA/PEO)₂/P3HMA/dPEO/P3HMA/PEO/P3HMA/dPEO film. The interfacial widths, σ_{int} , are given as full-width-at-half-maximum (FWHM), which is 2.35 times larger than the more commonly used root-mean-squared (RMS) width.

Layer	Nb (nm ⁻²)	d (nm)	σ_{int} (nm)
P3HMA/dPEO	2.516E-04	8.70	5.14

(P3HMA/PEO)₂/P3HMA/<i>d</i>PEO/			
P3HMA/PEO	2.261E-04	40.07	8.70
BPEI	1.967E-04	1.00	1.00
SiO₂	3.261E-04	1.06	1.00
Si	2.070E-04	—	0.50

Table B-4 Model parameters for a (P2HMA/PEO)₂/(P2HMA/*d*PEO)₂/(P2HMA/PEO)₇/(P2HMA/*d*PEO)₂ film.

Layer	<i>Nb</i> (nm⁻²)	<i>d</i> (nm)	σ_{int} (nm)
(P2HMA/<i>d</i>PEO)₂	2.037E-04	10.87	6.70
(P2HMA/PEO)₇	1.399E-04	35.03	5.70
(P2HMA/<i>d</i>PEO)₂	2.268E-04	3.81	3.81
(P2HMA/PEO)₂	1.314E-04	5.76	3.81
BPEI	8.492E-05	0.50	0.50
SiO₂	3.200E-04	2.00	0.50
Si	2.000E-04	—	0.50

Table B-5 Assignment of FTIR bands of linear polyphenols.

FTIR band assignment	P3HMA	P2HMA
Amide I band	1647 cm ⁻¹	1635 cm ⁻¹
Skeletal vibrations of benzene rings	1609 cm ⁻¹	1605 cm ⁻¹
Amide II	1515 cm ⁻¹	1518 cm ⁻¹
Skeletal vibrations of benzene rings + amide III	1452 cm ⁻¹	1445 cm ⁻¹
Aryl -C-O coupled with skeletal vibrations of benzene rings	1190 cm ⁻¹	1193 cm ⁻¹

-O-H coupled with skeletal vibrations of benzene rings	1030 cm ⁻¹	1112 cm ⁻¹
--	-----------------------	-----------------------

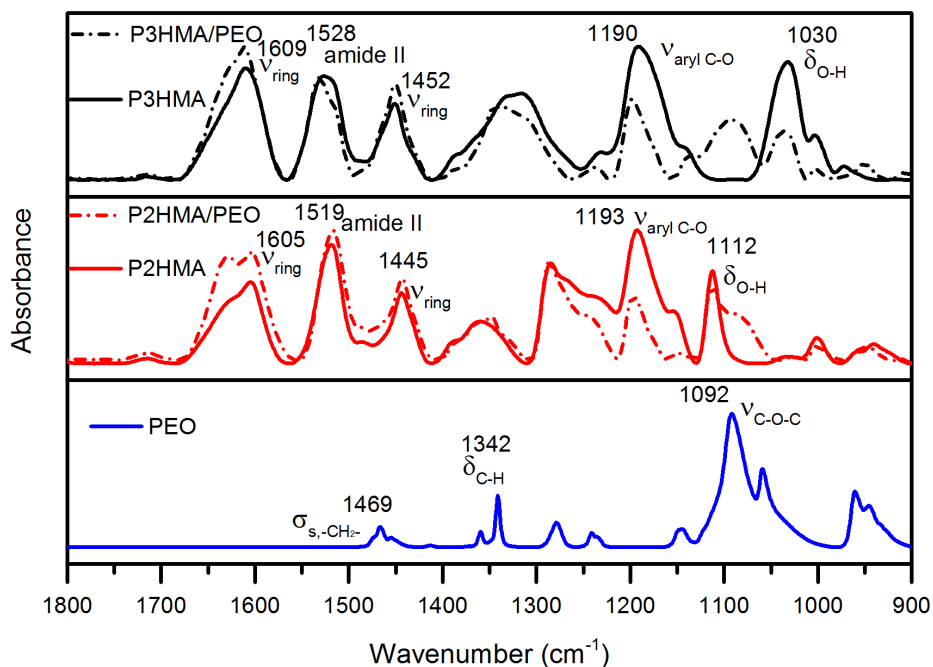


Figure B-1 ATR-FTIR spectra of P3HMA, 6.5-bilayer P3HMA/PEO film, P2HMA, 50.5-bilayer P2HMA/PEO film and PEO.

The spectrum of PEO features -CH- stretching asymmetric vibrations at 2885 cm⁻¹, -CH- stretching symmetric vibrations at 2860 cm⁻¹, -CH₂- scissoring vibrations at 1469 cm⁻¹, -C-H bending vibrations at 1342 cm⁻¹; and C-O-C stretching vibrations at 1092 cm⁻¹.¹⁷⁶⁻¹⁷⁸

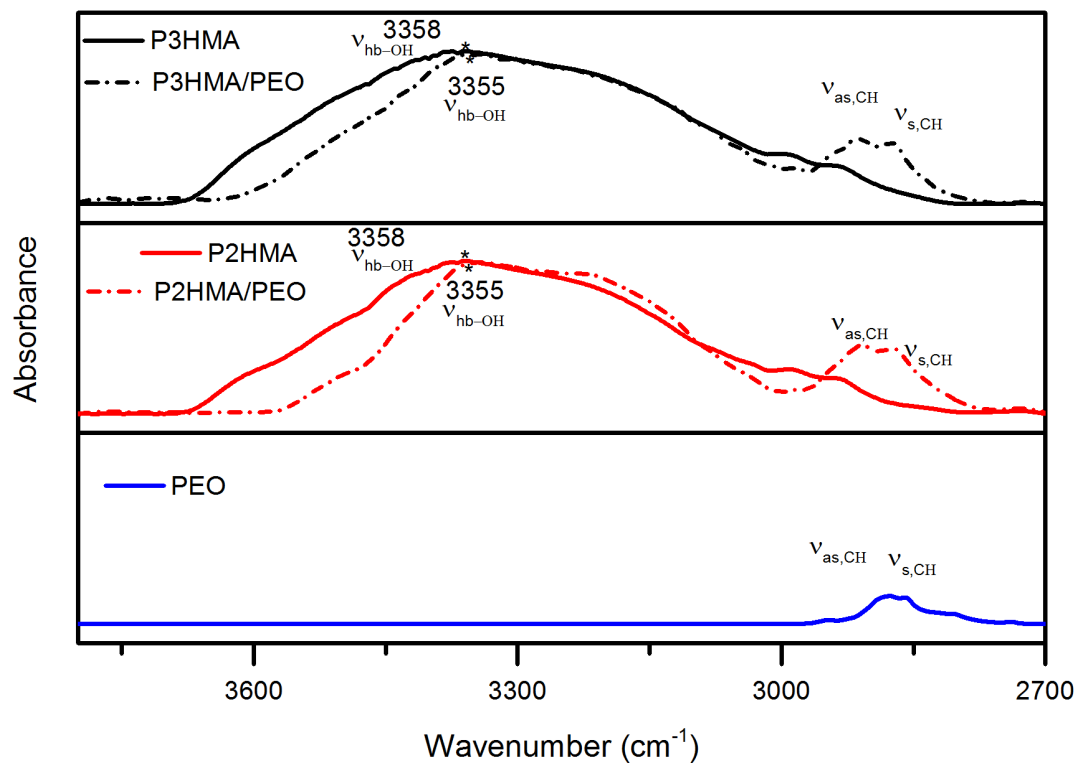


Figure B-2 ATR-FTIR spectra of P3HMA, 6.5-bilayer P3HMA/PEO film, P2HMA and 50.5-bilayer P2HMA/PEO film, and PEO between 3800 and 2700 cm^{-1} .

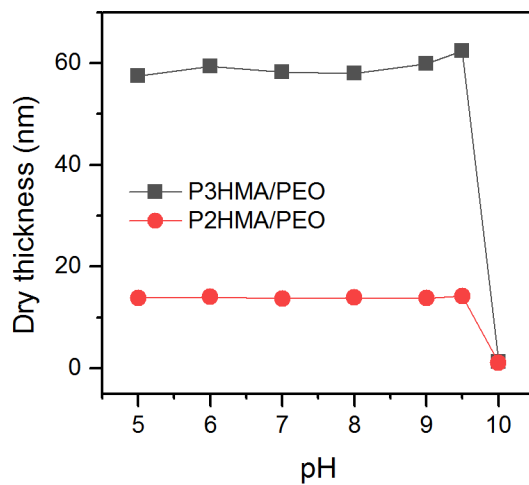


Figure B-3 pH stability of four-bilayer PPh/PEO films assessed as dry film thickness retained after 60 min of sequential exposure to phosphate buffer solutions at increasing pH.

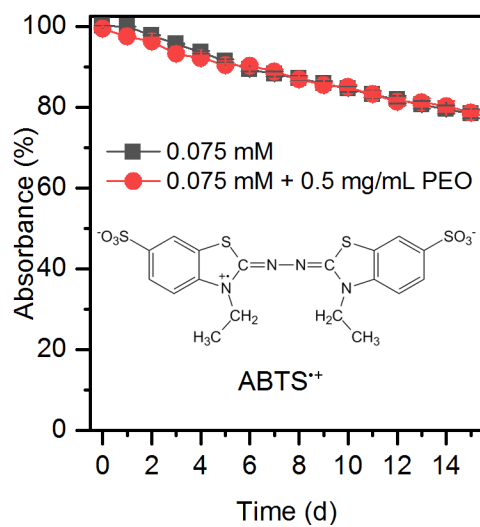


Figure B-4 Self-degradation of ABTS⁺ radical cation solutions with time as the percentage of initial absorbance value at 732 nm for 0.075 mM ABTS⁺ solution (A), and 0.075 mM ABTS⁺ in the presence of 0.5 mg/mL PEO (B).

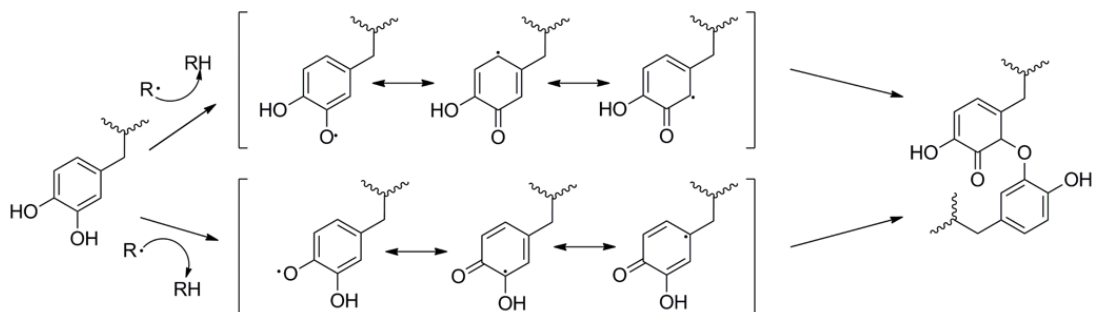


Figure B-5 Proposed resonance structures of semi-quinone radical of P2HMA and a radical coupling crosslinking structure.

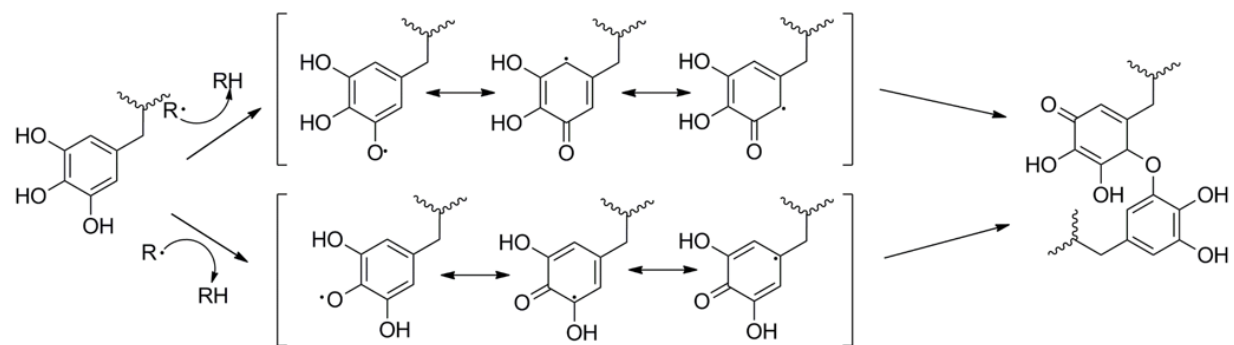


Figure B-6 Proposed resonance structures of semi-quinone radical of P3HMA and a radical coupling crosslinking structure.

APPENDIX C

SUPPORTING INFORMATION FOR THE CHAPTER 4

Synthesis of P2HAA and P3HAA

Synthesis of monomers: Monomers for polymerization of P2HAA and P3HAA were obtained in the following way. First, 5.00 g of 3,4-dimethoxybenzyl amine [0.025 mol] or of 3,4,5-trimethoxybenzyl amine [0.03 mol] used for synthesis of P2HAA and P3HAA, were dissolved in 50 mL of dichloromethane (DCM) in a 100 mL round bottom flask. Then 5.0 ml (6.9 g) of triethylamine (TEA) [0.069 mol] was added to the solution, and flask was placed on the ice bath. After 10 min, solution of 3.5 ml of acryloyl chloride [0.035 mol] in 10.0 mL of DCM was added drop wisely to the mixture at intense stirring. After stirring for 30 min the flask was warmed up to room temperature, and 10 ml of DI water was added. Then the mixture was washed twice with 0.1 M HCl and 1.0 M Na₂CO₃ aqueous solutions, and finally with water. DCM layer was then separated, dried over anhydrous MgSO₄, and consequently passed through a column packed with basic activated alumina and a column packed with acidic activated alumina (Brockmann I). The solvent was removed under vacuum to yield white solid (yield 87.4% and 85.3% for N-(3,4-dimethoxybenzyl) acrylamide) and N-(3,4,5-trimethoxybenzyl) acrylamide, respectively).

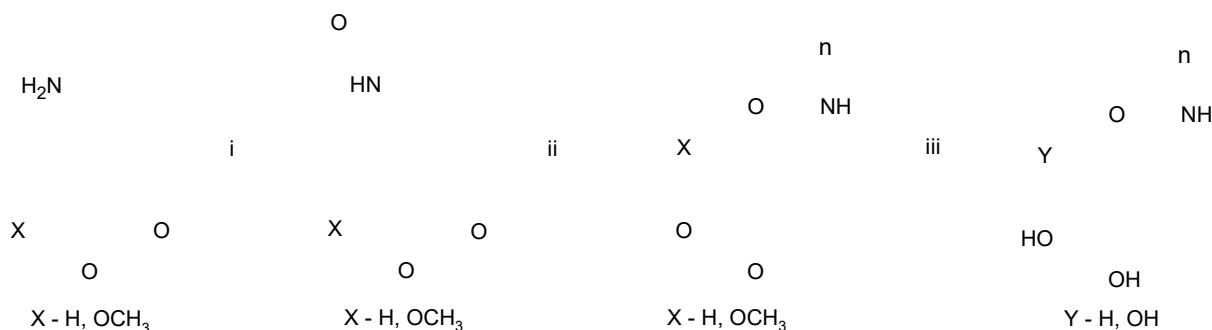


Figure C-1 A stepwise procedure used for P2HAA and P3HAA synthesis. Step i: acryloyl chloride, TEA, CH₂Cl₂, 30 min; step ii: AIBN as initiator, CPDTTC as CTA, dioxane, 70°C, 12-24 h; step iii: 1) BBr₃, CH₂Cl₂, -45°C to RT, 12 h; 2) water, overnight.

Monomer Characterization: Monomer characterization was performed by ¹H-NMR (300 MHz) using DMSO-d₆ as a solvent.

N-(3,4-dimethoxybenzyl) acrylamide: δ 8.2 t(1H, -NH-); 6.5 - 6.6 d (3H, C₆H₃(OCH₃)₂); 5.69 s (1H, CHH=); 5.35 s (1H, CHH=); 4.23 -4.25 d (2H, -CH₂-); 3.71 - 3.73 d (6H, -C₆H₃(OCH₃)₂); 2.49 s (solvent).

N-(3,4,5-trimethoxybenzyl) acrylamide: δ 8.2 t(1H, -NH-); 6.5 - 6.6 d (2H, C₆H₂(OCH₃)₃); 5.69 s (1H, CHH=); 5.35 s (1H, CHH=); 4.23 -4.25 d (2H, -CH₂-); 3.71 - 3.73 d (9H, -C₆H₂(OCH₃)₃); 2.49 s (solvent).

Polymerization: 12.0 mmol of the corresponding monomers (2.65 g of *N*-(3,4-dimethoxybenzyl) acrylamide or 3.01 g of *N*-(3,4,5-trimethoxybenzyl) acrylamide) were placed in a Schlenk tube, sealed, vacuumized, and filled with argon gas. Then 5.00 mL of anhydrous 1,4-dioxane was added and the solution was stirred at room temperature till complete dissolution of the monomers (about 30 min). In a separate flask, 30.0 mg 2,2'-azobis(2-methylpropionitrile) (AIBN) [0.183 mmol] and 365 mg of 2-(dodecylthiocarbonothioylthio)-2-methylpropionic acid (DDMAT) [1.00 mmol] were dissolved in 5.00 mL of anhydrous 1,4-dioxane. A 0.500 mL aliquot of this solution was added to the tube containing monomers. After three vacuum-thaw cycles, the tube was sealed and heated on the oil bath at 70°C for 12 h. The solution was then cooled to the room temperature, and 15.0 mL of DCM were added and stirred till complete dissolution of polymers. Polymer solutions were then slowly added drop-by-drop to 200 mL of n-hexane under vigorous stirring.

Demethylation: About 1.0 g of polymers was dissolved in 30 mL of anhydrous CH₂Cl₂ in a Schlenk flask. After three freeze-thaw cycles, the flasks containing polymer solutions were placed in a chlorobenzene slush (-45°C). Then ~ 1.5-fold excess BBr₃ was added as a 2M solution in CH₂Cl₂ was added dropwisely to the flask at intense steering. The solution was allowed to warm up to room temperature autonomously, and left overnight. A careful addition of 200 mL of degassed DI water resulted in precipitation. The mixture was stirred overnight, the product filtered in an inert atmosphere, and dried under vacuum.

Polymer Characterization: Gel permeation chromatography (GPC) was performed using an Agilent Technologies GPC system equipped with Agilent 1260 infinity multi-suite (refractive index and viscosity) detectors at 30 °C. A Phenogel™ column (Phenomenex) with a particle size of 5 μ m and a pore size of 103 Å was used. Characterization was performed using 1 to 5 mg mL⁻¹ solutions of protected or deprotected polymers in 0.01 M LiBr in DMF, which were eluted at a

rate of 0.10 mL min^{-1} at $30 \text{ }^\circ\text{C}$. Figure C-1 shows GPC traces for P2HAA and P3HAA deprotected polymers.

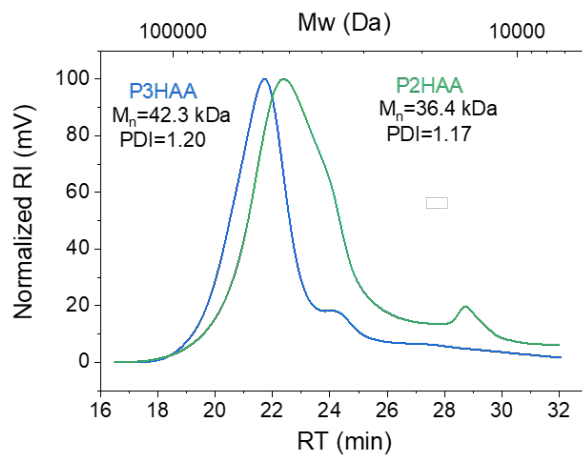


Figure C-2 GPC traces and the determined molecular weights and PDIs of P2HAA and P3HAA polymers.

Model of Neutron Reflectivity Data

General: The neutron specular reflectivity of the Layer-by-Layer-deposited films is modeled as a sequence of l layers, each featuring a scattering-length density Σ_l , thickness d_l , and an interfacial width with the layer above σ_l (fwhm of a Gaussian here). Using the known stoichiometry of the polymers used in the LbL deposition, the neutron scattering-length density can be decomposed into the product of mass density and a stoichiometry-dependent term containing the neutron scattering amplitudes of the constituent nuclei:

Equation C-1

$$\Sigma = \rho S \equiv \rho \frac{N_A \sum_j b_j}{M},$$

where N_A is Avogadro's number, b_j the scattering lengths of the nuclei in the formula unit (e.g. monomer or unit cell), and M the atomic mass of the formula unit. The values of the stoichiometry term S for the polymers involved in this work are given in Table C-1.

Ellipsometry measurements indicated the films varied in thickness by about 3% over the illuminated footprint of the neutron beam. This thickness variation causes a smearing of the total thickness fringes at higher Q values. We have modeled this smearing using a simple approximation to a distribution of film thicknesses wherein half of the film exhibits the nominal thickness d , a quarter is thinner ($d - \delta d$), and a quarter is thicker ($d + \delta d$). Neutron waves reflected from large lateral domains add incoherently, so the reflectivities of these differing thickness domains can simply be averaged,

Equation C-2

$$R_{\text{inc}} = (R_- + 2R_0 + R_+)/4,$$

where R_0 is the specular reflectivity of the film using the nominal thicknesses of the LbL polymer layers and R_+ and R_- are the reflectivities of films in which the thicknesses are increased or decreased by δd , respectively. As mentioned above, the lateral thickness disorder, $\delta d/d = 0.03$.

Protonated as-deposited film:

For each of the samples studied here, an approximately 1000-Å-thick polymer film was deposited LBL via alternating immersion in PEO and polyphenol solutions, as described in the text.

Individual layers intermix extensively with preceding and succeeding layers and so are not resolvable. The PEO/polyphenol multilayer is thus treated as a single composite layer:

Table C-1 Scattering lengths and stoichiometries for the components of the polyphenols and PEO: Compound, Formula Unit, the sum of the scattering lengths $\sum_j b_j$ of the nuclei in the Formula Unit, its molecular mass M , and its stoichiometry S .

Compound	Formula Unit	$\sum_j b_j$ (10^{-5} Å)	M (g mole ⁻¹)	S (10^{-6} Å ⁻² g ⁻¹ cm ³)
PEO (p)	C ₂ H ₄ O	4.13	44.06	0.57
<i>d</i> PEO (d)	C ₂ ² H ₄ O	45.78	48.06	5.73
P2HAA	C ₁₀ H ₁₁ NO ₃	52.08	193.22	1.62
P3HAA	C ₁₀ H ₁₁ NO ₄	57.89	209.22	1.67
P2HMA	C ₁₁ H ₁₃ NO ₃	51.25	207.25	1.49
P3HMA	C ₁₁ H ₁₃ NO ₄	57.05	223.25	1.54

Equation C-3

$$\Sigma^H = \rho [f_{\text{PEO}} S_{\text{PEO}} + (1 - f_{\text{PEO}}) S_{\text{P}n\text{H}p\text{A}}],$$

where f_{PEO} is the volume fraction of PEO, the number of phenol groups n is either 2 or 3, and monomer architecture p is either acrylate (A) or methacrylate (M). The films were modeled using four layers: 1) polyphenol/PEO composite; 2) BPEI seed layer; 3) silicon oxide layer; and 4) Si substrate. The BPEI seed and silicon oxide layers were thin and so did not produce Kiessig fringes within our measured Q range. We therefore modeled BPEI by holding its thickness constant at 10 Å and varying its SLD; the silicon oxide layer thickness was varied while its SLD was held constant at 3.20×10^{-6} Å⁻².

Using these definitions, the four-layer films were fitted using seven adjustable parameters: 1) mass density ρ ; 2) PEO volume fraction f_{PEO} ; 3) LbL film thickness d^{total} ; 4) surface roughness

σ^{surf} ; 5) BPEI SLD Σ^{BPEI} ; 6) silicon oxide layer thickness d^{SiOx} ; and 7) silicon substrate SLD Σ^{Si} . The fit to the substrate SLD is a sanity check of the known value of $2.07 \times 10^{-6} \text{ \AA}^{-2}$. The parameters of the four modeled layers are written in terms of the fitted parameters. The SLDs are $\Sigma_1 = \Sigma^{\text{H}}$ (Eqn. S2), $\Sigma_2 = \Sigma^{\text{BPEI}}$, $\Sigma_3 = 3.2 \times 10^{-6} \text{ \AA}^{-2}$, and $\Sigma_4 = \Sigma^{\text{Si}}$; the thicknesses $d_1 = d^{\text{total}}$, $d_2 = 10 \text{ \AA}$, and $d_3 = d^{\text{SiOx}}$; and $\sigma_1 = \sigma^{\text{surf}}$, $\sigma_2 = 10 \text{ \AA}$, and $\sigma_3 = \sigma_4 = 5 \text{ \AA}$. The fit to the data is insensitive to the interfacial widths of the underlayers, so these were held constant at physically reasonable values. The layer parameters are derived from the fitted parameters as described above and layer parameter uncertainties are propagated from the fitted parameters assuming they are uncorrelated Gaussian random variables.

Films after d PEO exposure

After immersion in d PEO solution, d PEO deposits both in a layer at the film surface and may also diffuse into and replace PEO within the existing film. In both cases, we can track the quantity of added or replaced material using the following expression:

Equation C-0-4

$$\Sigma^x = \rho \left\{ f_{\text{PEO}} \left[f_d^x \frac{M_{d\text{PEO}}}{M_{\text{PEO}}} S_{d\text{PEO}} + (1 - f_d^x) S_{\text{PEO}} \right] + (1 - f_{\text{PEO}}) S_{\text{PnHpA}} \right\},$$

where the superscript x denotes either original (H-stack) H or the added surface layer (D-stack) D and the volume fraction of d PEO within the layer is f_d^x . The subscripts on the polyphenol stoichiometry term are as in Eqn. C-3, values of M and S are found in Table C-1, and ρ and f_{PEO} are the fitted values for the as-deposited film. We impose the equivalence of the molar volume of d PEO and PEO by scaling the mass density by the ratio of their molecular masses.

The films exposed to d PEO were thus modeled using five layers: 1) d PEO-rich PEO/polyphenol composite; 2) d PEO-poor PEO/polyphenol composite; 3) BPEI seed layer; 4) silicon oxide layer; and 5) silicon substrate. The parameters of layers 3-5 were held constant at the values fitted for the as-deposited film. We were thereby able to fit the d PEO immersed sample reflectivities using seven adjustable parameters: 1) volume fraction of d PEO in the top layer (D-stack) f_d^{D} ; 2) volume fraction of d PEO in the underlayer (H-stack) f_d^{H} ; 3) thickness of d PEO-rich top layer d^{D} ; 4) total film thickness d^{total} ; 5) surface roughness σ^{surf} ; 6) interfacial width between D- and H-stacks σ^{HD} ; and 7) silicon substrate SLD Σ^{Si} . The parameters of the five modeled layers

are written in terms of the fitted parameters. The SLDs are $\Sigma_1 = \Sigma^D$ (Eqn. C-4), $\Sigma_2 = \Sigma^H$ (Eqn. C-3), $\Sigma_3 = \Sigma^{\text{BPEI}}$, $\Sigma_4 = 3.2 \times 10^{-6} \text{ \AA}^{-2}$, and $\Sigma_5 = \Sigma^{\text{Si}}$; the thicknesses $d_1 = d^D$, $d_2 = d^{\text{total}} - d^D$, $d_3 = 10 \text{ \AA}$, and $d_4 = d^{\text{SiO}_x}$; and $\sigma_1 = \sigma^{\text{surf}}$, $\sigma_2 = \sigma^{\text{HD}}$, $\sigma_3 = 10 \text{ \AA}$, and $\sigma_4 = \sigma_5 = 5 \text{ \AA}$.

P2HAA/PEO as deposited

Table C-2 Model parameters for the (P2HMA/PEO)₁₅/P2HAA film. The interfacial widths, σ , are given as full-width-at-half-maximum (FWHM), which is 2.35 times larger than the more commonly used root-mean-squared (RMS).

Parameter	Symbol	Value
1	ρ (g cm ⁻³)	1.37 ± 0.06
2	f_{PEO}	0.30 ± 0.05
3	d^{total} (Å)	1064.9 ± 10.5
4	σ^{surf} (Å)	21.8 ± 13.1
5	Σ^{BPEI} (10 ⁻⁶ Å ⁻²)	0.84 ± 0.51
6	d^{SiO_x} (Å)	23.3 ± 3.9
7	Σ^{Si} (10 ⁻⁶ Å ⁻²)	2.07 ± 0.06

P2HAA/PEO exposed to dPEO for 1 minute

Table C-3 Model parameters for the (P2HAA/PEO)₁₅/P2HAA film exposed to 0.2 mg/mL aqueous solution of dPEO for 1 min. The interfacial widths, σ , are given as full-width-at-half-maximum (FWHM), which is 2.35 times larger than the more commonly used root-mean-squared (RMS).

Parameter	Symbol	Value
1	f_d^{D}	0.13 ± 0.05
2	f_d^{H}	0.02 ± 0.03
3	d^{D} (Å)	71.6 ± 34.1
4	d^{total} (Å)	1059.7 ± 10.0
5	σ^{surf} (Å)	14.7 ± 12.7
6	σ^{HD} (Å)	71.6 ± 128.3
7	Σ^{Si} (10 ⁻⁶ Å ⁻²)	2.10 ± 0.07

P2HAA/PEO exposed to dPEO for 2 minutes

Table C-4 Model parameters for the (P2HAA/PEO)₁₅/P2HAA film exposed to 0.2 mg/mL aqueous solution of dPEO for 2 min. The interfacial widths, σ , are given as full-width-at-half-maximum (FWHM), which is 2.35 times larger than the more commonly used root-mean-squared (RMS).

Parameter	Symbol	Value
1	f_d^D	0.15 ± 0.05
2	f_d^H	0.01 ± 0.04
3	d^D (Å)	84.7 ± 37.2
4	d^{total} (Å)	1064.9 ± 10.9
5	σ^{surf} (Å)	15.4 ± 12.1
6	σ^{HD} (Å)	84.7 ± 117.5
7	Σ^{Si} (10^{-6} Å ⁻²)	2.10 ± 0.08

P2HAA/PEO exposed to dPEO for 5 minutes

Table C-5 Model parameters for the (P2HAA/PEO)₁₅/P2HAA film exposed to 0.2 mg/mL aqueous solution of dPEO for 5 min. The interfacial widths, σ , are given as full-width-at-half-maximum (FWHM), which is 2.35 times larger than the more commonly used root-mean-squared (RMS).

Parameter	Symbol	Value
1	f_d^D	0.13 ± 0.05
2	f_d^H	0.02 ± 0.04
3	d^D (Å)	66.5 ± 29.2
4	d^{total} (Å)	1072.6 ± 10.7
5	σ^{surf} (Å)	14.2 ± 12.6
6	σ^{HD} (Å)	66.5 ± 132.5

7	$\Sigma^{\text{Si}} (10^{-6} \text{ \AA}^{-2})$	2.09 ± 0.07
---	---	-----------------

P2HAA/PEO exposed to dPEO for 10 minutes

Table C-6 Model parameters for the (P2HAA/PEO)₁₅/P2HAA film exposed to 0.2 mg/mL aqueous solution of dPEO for 10 min. The interfacial widths, σ , are given as full-width-at-half-maximum (FWHM), which is 2.35 times larger than the more commonly used root-mean-squared (RMS).

Parameter	Symbol	Value
1	f_d^{D}	0.12 ± 0.05
2	f_d^{H}	0.01 ± 0.03
3	$d^{\text{D}} (\text{\AA})$	62.1 ± 30.2
4	$d^{\text{total}} (\text{\AA})$	1075.6 ± 9.8
5	$\sigma^{\text{surf}} (\text{\AA})$	15.0 ± 12.6
6	$\sigma^{\text{HD}} (\text{\AA})$	62.1 ± 127.0
7	$\Sigma^{\text{Si}} (10^{-6} \text{ \AA}^{-2})$	2.07 ± 0.05

P2HMA/PEO as deposited

Table C-7 Model parameters for the (P2HMA/PEO)₂₂/P2HMA film. The interfacial widths, σ , are given as full-width-at-half-maximum (FWHM), which is 2.35 times larger than the more commonly used root-mean-squared (RMS).

Parameter	Symbol	Value
1	$\rho (\text{g cm}^{-3})$	1.36 ± 0.07
2	f_{PEO}	0.34 ± 0.06
3	$d^{\text{total}} (\text{\AA})$	1074.5 ± 8.5
4	$\sigma^{\text{surf}} (\text{\AA})$	43.9 ± 16.9
5	$\Sigma^{\text{BPEI}} (10^{-6} \text{ \AA}^{-2})$	1.72 ± 0.61

6	d^{SiO_x} (Å)	41.3 ± 5.5
7	Σ^{Si} (10^{-6} Å ⁻²)	2.05 ± 0.06

P2HMA/PEO exposed to dPEO for 1 minute

Table C-8 Model parameters for the (P2HMA/PEO)₂₂/P2HMA film exposed to 0.2 mg/mL aqueous solution of dPEO for 1 min. The interfacial widths, σ , are given as full-width-at-half-maximum (FWHM), which is 2.35 times larger than the more commonly used root-mean-squared (RMS).

Parameter	Symbol	Value
1	f_d^{D}	0.12 ± 0.06
2	f_d^{H}	0.00 ± 0.02
3	d^{D} (Å)	84.7 ± 32.6
4	d^{total} (Å)	1082.7 ± 8.0
5	σ^{surf} (Å)	60.9 ± 15.4
6	σ^{HD} (Å)	69.3 ± 123.7
7	Σ^{Si} (10^{-6} Å ⁻²)	2.03 ± 0.07

P2HMA/PEO exposed to dPEO for 2 minutes

Table C-9 Model parameters for the (P2HMA/PEO)₂₂/P2HMA film exposed to 0.2 mg/mL aqueous solution of dPEO for 2 min. The interfacial widths, σ , are given as full-width-at-half-maximum (FWHM), which is 2.35 times larger than the more commonly used root-mean-squared (RMS).

Parameter	Symbol	Value
1	f_d^{D}	0.12 ± 0.05
2	f_d^{H}	0.02 ± 0.02
3	d^{D} (Å)	86.6 ± 33.1
4	d^{total} (Å)	1082.6 ± 8.0

5	σ^{surf} (Å)	55.7 ± 16.7
6	σ^{HD} (Å)	25.4 ± 193.8
7	Σ^{Si} (10^{-6} Å ⁻²)	2.05 ± 0.07

P2HMA/PEO exposed to dPEO for 5 minutes

Table C-10 Model parameters for the (P2HMA/PEO)₂₂/P2HMA film exposed to 0.2 mg/mL aqueous solution of dPEO for 5 min. The interfacial widths, σ , are given as full-width-at-half-maximum (FWHM), which is 2.35 times larger than the more commonly used root-mean-squared (RMS).

Parameter	Symbol	Value
1	f_d^{D}	0.17 ± 0.06
2	f_d^{H}	0.01 ± 0.02
3	d^{D} (Å)	81.2 ± 27.2
4	d^{total} (Å)	1089.4 ± 7.9
5	σ^{surf} (Å)	61.5 ± 13.9
6	σ^{HD} (Å)	79.4 ± 99.5
7	Σ^{Si} (10^{-6} Å ⁻²)	2.04 ± 0.07

P2HMA/PEO exposed to dPEO for 10 minutes

Table C-11 Model parameters for the (P2HMA/PEO)₂₂/P2HMA film exposed to 0.2 mg/mL aqueous solution of dPEO for 10 min. The interfacial widths, σ , are given as full-width-at-half-maximum (FWHM), which is 2.35 times larger than the more commonly used root-mean-squared (RMS).

Parameter	Symbol	Value
1	f_d^{D}	0.18 ± 0.06
2	f_d^{H}	0.00 ± 0.02
3	d^{D} (Å)	78.9 ± 21.5

4	d^{total} (Å)	1093.0 ± 8.5
5	σ^{surf} (Å)	72.9 ± 14.9
6	σ^{HD} (Å)	51.1 ± 95.2
7	Σ^{Si} (10^{-6} Å ⁻²)	2.01 ± 0.07

P3HAA/PEO as deposited

Table C-12 Model parameters for the (P3HAA/PEO)₁₀/P3HAA film. The interfacial widths, σ , are given as full-width-at-half-maximum (FWHM), which is 2.35 times larger than the more commonly used root-mean-squared (RMS).

Parameter	Symbol	Value
1	ρ (g cm ⁻³)	1.27 ± 0.05
2	f_{PEO}	0.27 ± 0.05
3	d^{total} (Å)	1021.4 ± 13.3
4	σ^{surf} (Å)	42.9 ± 7.3
5	Σ^{BPEI} (10^{-6} Å ⁻²)	0.78 ± 0.57
6	d^{SiO_x} (Å)	9.0 ± 4.1
7	Σ^{Si} (10^{-6} Å ⁻²)	2.08 ± 0.05

P3HAA/PEO exposed to dPEO for 1 minute

Table C-13 Model parameters for the (P3HAA/PEO)₁₀/P3HAA film exposed to 0.2 mg/mL aqueous solution of dPEO for 1 min. The interfacial widths, σ , are given as full-width-at-half-maximum (FWHM), which is 2.35 times larger than the more commonly used root-mean-squared (RMS).

Parameter	Symbol	Value
1	f_d^{D}	0.10 ± 0.04
2	f_d^{H}	0.03 ± 0.05

3	d^D (Å)	154.4 ± 112.8
4	d^{total} (Å)	1022.2 ± 17.0
5	σ^{surf} (Å)	26.9 ± 8.5
6	σ^{HD} (Å)	122.8 ± 220.1
7	Σ^{Si} (10^{-6} Å ⁻²)	2.09 ± 0.05

P3HAA/PEO exposed to dPEO for 2 minutes

Table C-14 Model parameters for the (P3HAA/PEO)₁₀/P3HAA film exposed to 0.2 mg/mL aqueous solution of dPEO for 2 min. The interfacial widths, σ , are given as full-width-at-half-maximum (FWHM), which is 2.35 times larger than the more commonly used root-mean-squared (RMS).

Parameter	Symbol	Value
1	f_d^D	0.10 ± 0.04
2	f_d^H	0.04 ± 0.05
3	d^D (Å)	161.3 ± 105.3
4	d^{total} (Å)	1013.3 ± 17.6
5	σ^{surf} (Å)	29.0 ± 8.8
6	σ^{HD} (Å)	102.8 ± 233.6
7	Σ^{Si} (10^{-6} Å ⁻²)	2.09 ± 0.05

P3HAA/PEO exposed to dPEO for 5 minutes

Table C-15 Model parameters for the (P3HAA/PEO)₁₀/P3HAA film exposed to 0.2 mg/mL aqueous solution of dPEO for 5 min. The interfacial widths, σ , are given as full-width-at-half-maximum (FWHM), which is 2.35 times larger than the more commonly used root-mean-squared (RMS).

Parameter	Symbol	Value
1	f_d^D	0.07 ± 0.04

2	f_d^H	0.03 ± 0.05
3	d^D (Å)	213.0 ± 245.1
4	d^{total} (Å)	1028.2 ± 16.7
5	σ^{surf} (Å)	29.5 ± 8.3
6	σ^{HD} (Å)	213.0 ± 326.0
7	Σ^{Si} (10^{-6} \AA^{-2})	2.04 ± 0.04

P3HAA/PEO exposed to dPEO for 10 minutes

Table C-16 Model parameters for the (P3HAA/PEO)₁₀/P3HAA film exposed to 0.2 mg/mL aqueous solution of dPEO for 10 min. The interfacial widths, σ , are given as full-width-at-half-maximum (FWHM), which is 2.35 times larger than the more commonly used root-mean-squared (RMS).

Parameter	Symbol	Value
1	f_d^D	0.08 ± 0.04
2	f_d^H	0.03 ± 0.05
3	d^D (Å)	237.5 ± 657.9
4	d^{total} (Å)	1028.4 ± 17.6
5	σ^{surf} (Å)	30.5 ± 7.9
6	σ^{HD} (Å)	237.5 ± 276.1
7	Σ^{Si} (10^{-6} \AA^{-2})	2.04 ± 0.04

P3HMA/PEO exposed to dPEO for 1 minute

Table C-17 Model parameters for the (P3HMA/PEO)₄/P3HMA film exposed to 0.2 mg/mL aqueous solution of dPEO for 1 min. The interfacial widths, σ , are given as full-width-at-half-maximum (FWHM), which is 2.35 times larger than the more commonly used root-mean-squared (RMS).

Parameter	Symbol	Value
-----------	--------	-------

1	f_d^D	0.34 ± 0.05
2	f_d^H	0.14 ± 0.09
3	d^D (Å)	891.9 ± 232.6
4	d^{total} (Å)	1122.1 ± 14.2
5	σ^{surf} (Å)	11.6 ± 9.4
6	σ^{HD} (Å)	230.2 ± 327.2
7	Σ^{Si} (10^{-6} Å ⁻²)	2.06 ± 0.15

P3HMA/PEO exposed to dPEO for 2 minutes

Table C-18 Model parameters for the (P3HMA/PEO)₄/P3HMA film exposed to 0.2 mg/mL aqueous solution of dPEO for 2 min. The interfacial widths, σ , are given as full-width-at-half-maximum (FWHM), which is 2.35 times larger than the more commonly used root-mean-squared (RMS).

Parameter	Symbol	Value
1	f_d^D	0.31 ± 0.04
2	f_d^H	0.13 ± 0.09
3	d^D (Å)	930.5 ± 110.9
4	d^{total} (Å)	1120.2 ± 14.6
5	σ^{surf} (Å)	6.2 ± 11.7
6	σ^{HD} (Å)	189.7 ± 289.2
7	Σ^{Si} (10^{-6} Å ⁻²)	2.05 ± 0.13

P3HMA/PEO exposed to dPEO for 5 minutes

Table C-19 Model parameters for the (P3HMA/PEO)₄/P3HMA film exposed to 0.2 mg/mL aqueous solution of dPEO for 5 min. The interfacial widths, σ , are given as full-width-at-

half-maximum (FWHM), which is 2.35 times larger than the more commonly used root-mean-squared (RMS).

Parameter	Symbol	Value
1	f_d^D	0.24 ± 0.05
2	f_d^H	0.15 ± 0.07
3	d^D (Å)	920.7 ± 159.1
4	d^{total} (Å)	1133.2 ± 16.2
5	σ^{surf} (Å)	11.8 ± 10.0
6	σ^{HD} (Å)	212.5 ± 491.5
7	Σ^{Si} (10^{-6} Å ⁻²)	2.04 ± 0.08

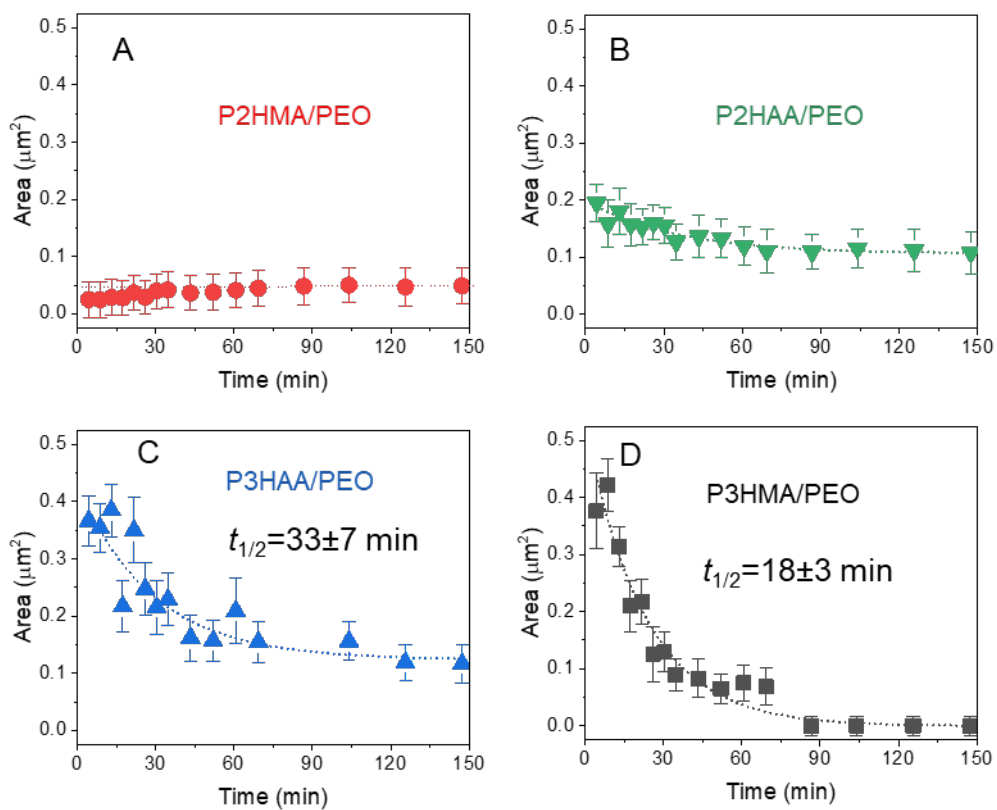


Figure C-2 Time evolution of the lateral dimensions of the indented areas measured at the depth of 25 nm within the films using *in situ* AFM for P2HMA/PEO (A), P2HAA/PEO (B), P3HAA/PEO (C), and P3HMA/PEO (D) films during their continuous immersion in water.

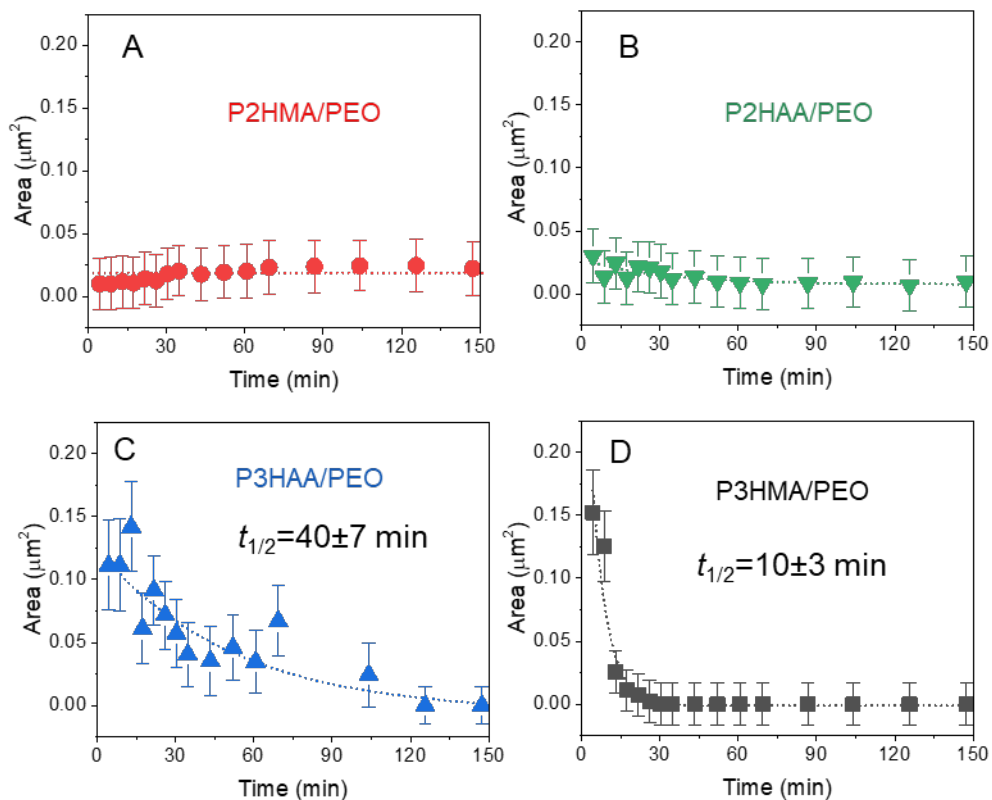


Figure C-3 Time evolution of the lateral dimensions of the indented areas measured at the depth of 60 nm within the films using *in situ* AFM for P2HMA/PEO (A), P2HAA/PEO (B), P3HAA/PEO (C), and P3HMA/PEO (D) films during their continuous immersion in water.